

# **Aerosol Deposition Measurements as a Function of Reynolds Number for Turbulent Flow in a Ninety-Degree Pipe Bend**

by

**Scott R. Wilson, B.Eng Aerospace Engineering**

A Thesis submitted to  
the Faculty of Graduate Studies and Research  
in partial fulfilment of  
the requirements for the degree of  
**Master of Applied Science  
in Mechanical Engineering**

Ottawa-Carleton Institute for  
Mechanical and Aerospace Engineering

Department of Mechanical and Aerospace Engineering  
Carleton University  
Ottawa, Ontario, Canada  
March 5, 2008

Copyright ©  
2008 – Scott R. Wilson



Library and  
Archives Canada

Published Heritage  
Branch

395 Wellington Street  
Ottawa ON K1A 0N4  
Canada

Bibliothèque et  
Archives Canada

Direction du  
Patrimoine de l'édition

395, rue Wellington  
Ottawa ON K1A 0N4  
Canada

*Your file* *Votre référence*  
*ISBN: 978-0-494-40646-5*  
*Our file* *Notre référence*  
*ISBN: 978-0-494-40646-5*

**NOTICE:**

The author has granted a non-exclusive license allowing Library and Archives Canada to reproduce, publish, archive, preserve, conserve, communicate to the public by telecommunication or on the Internet, loan, distribute and sell theses worldwide, for commercial or non-commercial purposes, in microform, paper, electronic and/or any other formats.

The author retains copyright ownership and moral rights in this thesis. Neither the thesis nor substantial extracts from it may be printed or otherwise reproduced without the author's permission.

**AVIS:**

L'auteur a accordé une licence non exclusive permettant à la Bibliothèque et Archives Canada de reproduire, publier, archiver, sauvegarder, conserver, transmettre au public par télécommunication ou par l'Internet, prêter, distribuer et vendre des thèses partout dans le monde, à des fins commerciales ou autres, sur support microforme, papier, électronique et/ou autres formats.

L'auteur conserve la propriété du droit d'auteur et des droits moraux qui protègent cette thèse. Ni la thèse ni des extraits substantiels de celle-ci ne doivent être imprimés ou autrement reproduits sans son autorisation.

---

In compliance with the Canadian Privacy Act some supporting forms may have been removed from this thesis.

Conformément à la loi canadienne sur la protection de la vie privée, quelques formulaires secondaires ont été enlevés de cette thèse.

While these forms may be included in the document page count, their removal does not represent any loss of content from the thesis.

Bien que ces formulaires aient inclus dans la pagination, il n'y aura aucun contenu manquant.

  
**Canada**

## **Abstract**

Motivated by the study of aerosol deposition in a human nasal cavity, a preliminary study was made of deposition in a 90° pipe bend for turbulent flow. Deposition fraction data are presented for different flow Reynolds numbers (10 000, 20 000 and 30 100). The results agree with previous studies, indicating that the effect of the flow Reynolds number on the deposition fraction is not significant; however, a small effect was detected for Stokes number near 0.15. A Reynolds number increase from 10 000 to 20 000 caused a deposition fraction increase of 0.1. Numerical simulations were done, using the Reynolds Averaged Navier-Stokes (RANS) equations with the Shear Stress Transport turbulence model. Modeling with inertial impaction only, the results agree well with the experimental data; however, they fail to detect the small effect seen experimentally. The inclusion of turbulent particle tracking in the RANS simulation via an eddy interaction model did not improve the results. However, based on an analytical analysis of the particle tracking equation and drawing data from the numerical results, it was hypothesised that the Reynolds number effect on deposition at low Stokes numbers is due to turbulent dispersion.

## **Acknowledgements**

Thanks are due to my supervisors, Professors Johnson and Matida, for guiding me through this study and funding me. Also, the support of the other students in our research group was crucial. I also thank my parents for supporting me throughout.

## Table of Contents

Abstract.....	i
Acknowledgements.....	ii
Table of Contents.....	iii
List of Tables.....	v
List of Figures.....	vi
Nomenclature.....	viii
Chapter 1: Introduction.....	1
1.1 Typical Approaches to Studying Aerosol Deposition.....	1
1.2 Experimental Studies of Aerosol Deposition in Laminar Flow.....	4
1.3 Theoretical Studies of Aerosol Deposition in Laminar Flow.....	7
1.4 Experimental Studies for Aerosol Deposition in Turbulent Flow.....	11
1.5 Numerical Studies of Aerosol Deposition in Turbulent Flow.....	14
1.6 Scope of this Study.....	17
Chapter 2: Theory.....	19
2.1 Deposition Modes.....	19
2.2 Dimensional Analysis.....	20
2.3 Molecular Diffusion.....	23
2.4 Motion Due To Inertia.....	25
2.5 Discussion of the Particle Equation.....	27
2.6 Turbulent Dispersion.....	31
2.6.1 Estimating Deposition From Turbulent Dispersion.....	32
2.6.2 The Effect of Turbulent Dispersion on the Inlet Particle Distribution.....	35
2.7 The Fluid Equations.....	35
2.8 Secondary Flow.....	36
2.9 Summary of the Significant Parameters.....	37
Chapter 3: Experimental Apparatus and Methodology.....	38
3.1 The Flow System and Aerosol Generation.....	40
3.1.1 The Aerosol Generator.....	40
3.1.2 The Charge Neutralizer.....	42
3.1.3 The Mixing Chamber.....	42
3.1.4 The Particle Size Distribution Analyzer.....	42
3.1.5 The Test Section.....	45
3.1.6 The Filter.....	45
3.1.7 The Pressure Gauge.....	46
3.1.8 The Mass Flow Meter.....	47
3.1.9 The Vacuum Pump.....	48
3.2 Procedure for Measuring Deposition.....	48
3.2.1 Wash Procedure.....	49
3.2.2 The Spectrophotometer.....	52
Chapter 4: Uncertainty Analysis.....	56
4.1 Bias Error.....	56

4.1.1	Curvature Ratio .....	57
4.1.2	Density Ratio .....	57
4.1.3	Flow Reynolds Number .....	58
4.1.4	Stokes Number .....	59
4.1.5	Deposition Fraction .....	61
4.2	Precision .....	63
4.3	Total Uncertainty .....	63
Chapter 5:	Experimental Results .....	64
Chapter 6:	Simulations .....	68
6.1	Background .....	68
6.2	Fluid Velocity Field Calculation .....	69
6.3	Mesh .....	71
6.4	Particle Trajectory Calculation .....	75
6.5	Results and Discussion .....	80
6.5.1	Flow-field simulation results .....	80
6.5.2	Particle tracking simulation results .....	88
6.5.3	Analytic Modeling of Particle Response to Turbulence .....	94
Chapter 7:	Conclusions .....	100
References	.....	101
Appendix A:	The Fluid Equations .....	104
Appendix B:	Discussion of the Particle Equation .....	110

## List of Tables

Table 1.1 Summary of the Laminar Experimental Studies.....	7
Table 1.2 Summary of the Laminar Theoretical Studies .....	11
Table 1.3 Summary of the Turbulent Experimental Studies.....	14
Table 1.4 Summary of the Turbulent Theoretical Studies.....	17
Table 4.1 Bias Limits.....	62
Table 5.1: Experimental Results (Curvature ratio is $7.4 \pm 0.5$ . Density ratio is $770 \pm 20$ ) .....	64
Table 6.1: Deposition fractions obtained from numerical simulations (Curvature ratio = 7.4. Density ratio = 760) .....	88
Table 6.2 Turbulent Frequency Scales and Corresponding Particle Amplitude Ratios ...	97

## List of Figures

Figure 1.1: Typical Aerosol Deposition Measurement Setup (Pui et al., 1987).....	2
Figure 1.2: Bend Curvature Ratio, $\delta = R / a$ .....	4
Figure 1.3: Laminar Experimental Studies $\left( St = \frac{\rho_p d_p^2 Q}{18\pi\mu a^3} \right)$ .....	6
Figure 1.4: Laminar Theoretical Studies $\left( St = \frac{\rho_p d_p^2 Q}{18\pi\mu a^3} \right)$ .....	10
Figure 1.5: Turbulent Experimental Studies $\left( St = \frac{\rho_p d_p^2 Q}{18\pi\mu a^3} \right)$ .....	13
Figure 1.6: Turbulent Theoretical Studies $\left( St = \frac{\rho_p d_p^2 Q}{18\pi\mu a^3} \right)$ .....	16
Figure 2.1: Flow-Field in a 90° Bend Showing Dean Vortices (Breuer et al., 2006). The legend refers to the relative velocity magnitude. ....	37
Figure 3.1: Schematic of Experimental Apparatus .....	38
Figure 3.2 The 90° Bent Pipe with Downstream Filter .....	39
Figure 3.3: Typical Particle Size Graph, $Re = 20\ 000$ , $St = 0.47$ ( $d_p = 5.41\ \mu m$ ) .....	44
Figure 3.4: Entrance Section Acetone Wash .....	50
Figure 3.5: Exit Section Methanol Wash.....	51
Figure 3.6: Filter Methanol Wash.....	51
Figure 3.7: Soaking of the 90° Test Section as Part of the Methanol Wash Procedure ...	52
Figure 3.8: The Spectrophotometer .....	54
Figure 3.9: Typical Absorbance Plot. The solid line is a group of bend measurements. The broken line is a group of filter measurements.....	55
Figure 5.1: $Re = 10\ 000$ Results Compared with Experimental Results of Pui et al. (1987). $\left( St = \frac{\rho_p d_p^2 Q}{18\pi\mu a^3} \right)$ .....	66

Figure 5.2: Experimental Results $\left( St = \frac{\rho_p d_p^2 Q}{18\pi\mu a^3} \right)$ .....	67
Figure 6.1: Overall Computational Geometry (a) and Representation of the Computational Grid (b) (at the midplane of the geometry and at a cross section at the entrance of the bend).....	72
Figure 6.2 Grid Convergence Study of the Test Section Inlet Pressure (area average)....	73
Figure 6.3 Grid Convergence Study of the Velocity into and out of the Bend.....	74
Figure 6.5 Particle Sensitivity Analysis $\left( St = \frac{\rho_p d_p^2 Q}{18\pi\mu a^3} \right)$ .....	79
Figure 6.6 Velocity Magnitude from RANS Results, Re = 10 000. (The radial axis runs vertically on the page for each of the cross-sectional views) .....	81
Figure 6.7 Velocity Magnitude from RANS Results, Re = 20 000 (The radial axis runs vertically on the page for each of the cross-sectional views). .....	82
Figure 6.9 Velocity in the Plane of the Bend Exit .....	84
Figure 6.10 Turbulent Kinetic Energy from RANS Results, Re = 10 000 (The radial axis runs vertically on the page for each of the cross-sectional views).....	85
Figure 6.11 Turbulent Kinetic Energy from RANS Results, Re = 20 000. (The radial axis runs vertically on the page for each of the cross-sectional views).....	86
Figure 6.12 Velocity Magnitude from RANS Results, Re = 30 000 (The radial axis runs vertically on the page for each of the cross-sectional views) .....	87
Figure 6.13 Numerical Results (mean flow tracking) against Experimental Results $\left( St = \frac{\rho_p d_p^2 Q}{18\pi\mu a^3} \right)$ .....	89
Figure 6.14 Numerical Results (turbulent dispersion tracking) against Experimental Results $\left( St = \frac{\rho_p d_p^2 Q}{18\pi\mu a^3} \right)$ .....	90
Figure 6.15 Turbulence Intensity (I) Half-Way Around the Bend and at the Exit .....	93
Figure 6.16 Particle Amplitude Ratio Response to Velocity Fluctuations at Different Turbulent Frequency Scales.....	98
Figure A1: Toroidal Coordinates for the Bend.....	104

## Nomenclature

$A$	Cross-sectional area
$a$	Pipe radius
$Ab$	Absorption fraction of a sample measured by the spectrophotometer
$c$	Particle number concentration
$C_C$	Cunningham's slip correction factor
$C_D$	Drag coefficient
$C_{D,Stokes}$	Drag coefficient for the Stokes drag law
$C$	Volumetric concentration of vitamin E in the vitamin E solution
CR	Denotes Curvature Ratio ( $\delta$ )
$C_\mu$	A constant in the eddy diffusivity formula
DF	Deposition Fraction
$De$	Dean number
$D$	Diffusion coefficient
$d$	Particle diameter
$d_a$	Aerodynamic diameter
$\frac{D}{dt}$	total time derivative for a fluid particle
$\frac{d}{dt}$	total time derivative for an aerosol particle (or for a fluid particle)
$\vec{F}_{Drag}$	Drag force on aerosol particle due to the air
$\vec{F}_{Saffman}$	Saffman lift force
$f$	Frequency of the aerosol generator (also used as an arbitrary function, or as a pipe friction factor)
$F$	A function in the turbulence model
$g$	Gravitational acceleration constant

$I$	Volumetric concentration of non-volatile impurities. Also used to denote turbulence intensity
$I_n$	Incident light on a sample in the spectrophotometer
$K$	wavenumber
$k$	Boltzmann's constant (or turbulence kinetic energy)
$L$	Pipe length
$m$	Mass
$\dot{m}$	Mass flow rate of air
$N$	Vol times Ab. Also used to denote a random number.
$P$	Air pressure
$Pe$	Peclet number
$P_{gauge}$	Gauge pressure of air
$Q_{Pi}$	Volumetric flow rate of aerosol particles into the bend
$Q_{Po}$	Volumetric flow rate of aerosol particles out of the bend
$Q$	Volume flow rate of air
$Q_S$	Volume flow rate of vitamin E solution
$Q_{SLPM}$	Flow rate of air assuming atmospheric air density
$Re$	Reynolds number based on the pipe diameter and the area-average velocity through the pipe
$Re_p$	Reynolds number of aerosol particle
$Re_{p,\infty}$	Freestream particle Reynolds number
$Re_{v_e}$	Reynolds number based on the eddy viscosity
$Ri$	Richardson number
$r$	Radial coordinate of the pipe cross-section
$R$	Radius of the bend (or gas constant of air)
$S$	Turbulence kinetic energy density function
$SG$	Specific Gravity
$St$	Stokes number
$t$	time
$T$	Temperature
$Tr$	Transmitted light for a sample in the spectrophotometer

$u$	Velocity component in the r-direction, or the x-direction
$U$	Bias error (subscripts denote what is referred to)
$\vec{V}$	Velocity of air
$v$	Velocity component in the $\alpha$ -direction, or the y-direction
$V$	Area average speed of air through the pipe (or sometimes denotes the local speed)
$Vol$	Volume of wash solution
$w$	Velocity component in the $\theta$ -direction, or the z-direction
$x,y,z$	Rectangular coordinates

### Greek

$\delta$	Curvature ratio
$\rho$	Density
$\mu$	Viscosity of air
$\nabla^2$	Laplace operator
$\theta$	Angular coordinate around the pipe bend
$\nabla$	Gradient operator
$\alpha$	Angular coordinate around the pipe cross-section
$\nu$	Kinematic viscosity of air
$\nu_e$	Eddy viscosity, or eddy diffusivity
$\lambda$	Density ratio
$\tau$	time constant
$\rho_{atmosphere}$	Atmospheric air density
$\Omega$	Absolute value of vorticity
$\Phi, \Phi_1, \Phi_2,$ $\beta, \beta', \alpha,$ $\sigma, \sigma'$	Constants in the turbulence model
$\varepsilon$	eddy dissipation
$\omega$	turbulent eddy frequency (also used to denote a circular frequency)
$\Gamma$	velocity gradient

$\eta$  amplitude ratio

### Subscripts

$f$  fluid  
 $p$  particle  
 $rel$  particle relative to the flow-field  
 $e$  eddy  
 $x,y,z$  x,y,z components  
 $bend$  bend  
 $filter$  filter  
 $m$  time mean values  
 $K$  Kolmogorov  
 $L$  Large eddies

### Superscripts

' A prime subscript denotes a turbulent fluctuation  
(n) non-dimensional  
(0) undisturbed flow-field  
(1) perturbation of the flow-field  
(2) perturbed flow-field

## **Chapter 1: Introduction**

This thesis investigates the influence of the flow Reynolds number on the aerosol deposition fraction in a 90° pipe bend, for turbulent flows. Although the longer term goals of this work involve pharmaceutical aerosol deposition investigations in complex geometries (such as nasal cavities and extra-thoracic airways), the relatively simpler geometry facilitates fundamental investigations to better understand the deposition process.

An aerosol is a suspension of particles (either solid or liquid) in a gas. There are many practical examples of aerosols flowing through bends, which create challenging engineering problems. These challenges include: the prevention of icing in curved aircraft intake ducts (which motivated the study of Hacker et al., 1953), the removal of particulates from industrial duct bends (a concern of Peters and Leith, 2004), the sampling of contaminants in gas streams, in which a bend occurs in the sampling line (which motivated the studies of Pui et al., 1987 and McFarland et al., 1997), the erosion of pipe bends due to solid aerosol particles (a concern of Yeung 1979), and the deposition of particles in the respiratory tract (for example the throat model of Zhang et al., 2004).

### **1.1 Typical Approaches to Studying Aerosol Deposition**

Aerosol deposition in bends has been studied experimentally, analytically, and numerically, for both the laminar case and the turbulent case. Figure 1.1 shows a typical experimental setup for aerosol deposition experiments (Pui et al., 1987). Flow is generated by a vacuum pump. The flow rate is measured by the flow meter and varied using the valve. Aerosol is generated and directed to the test section. Part of the aerosol

is deposited in the test section, and part will penetrate the test section to be collected in a filter. After the experiments (typically a half hour), the test section and the filter are washed separately with solvents. A technique is used to measure the volume concentration of the aerosol particle substance in the solvent, such as fluorometry or spectrophotometry. Since the density is known, the deposition fraction (DF) can be calculated by

$$DF = \frac{m_{p,bend}}{m_{p,bend} + m_{p,filter}}, \quad (1)$$

where  $m$  refers to mass, the subscript  $p$  refers to particle (aerosol particle), and the subscripts *bend* and *filter* refer to the bend and filter, respectively.

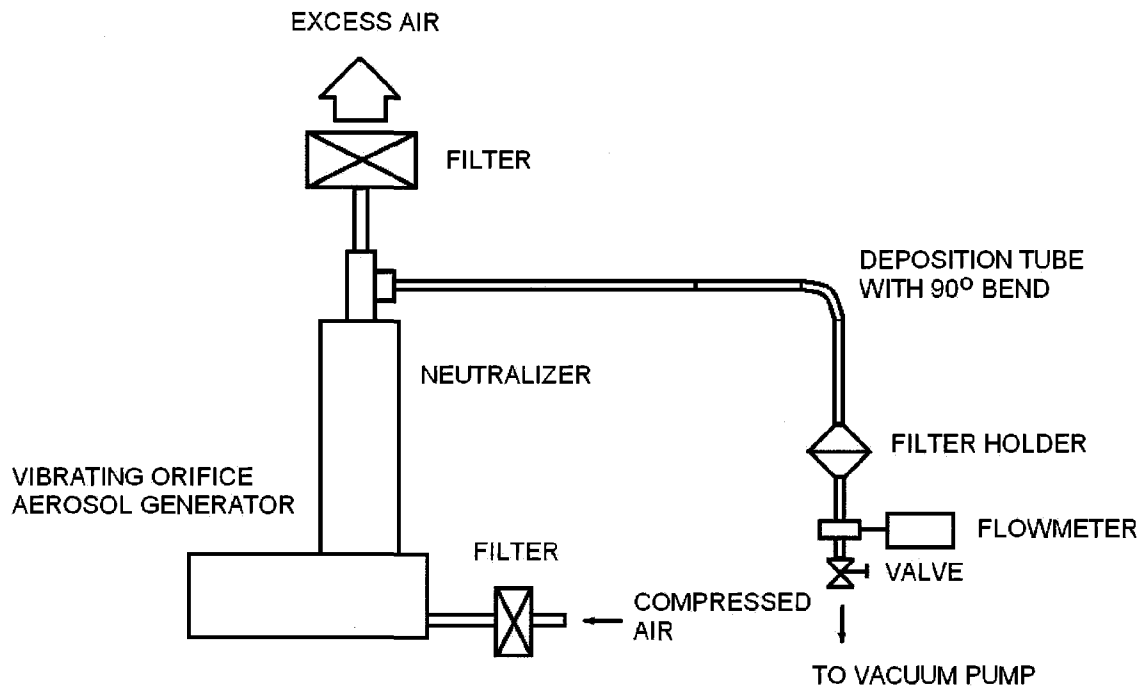


**Figure 1.1: Typical Aerosol Deposition Measurement Setup (Pui et al., 1987)**

Aerosol deposition can be studied numerically by first simulating the single-phase fluid flow and subsequently releasing particles into the flow and tracking their transport using a Lagrangian approach. Direct Numerical Simulation (DNS), Large Eddy Simulation (LES), or RANS (Reynolds Averaged Navier-Stokes) equations are all potential approaches for simulating the fluid flow. In the Lagrangian approach, thousands of particles are released and the particulate phase is solved by the integration of the particle equation of motion. Thousands of particles are released in order to gather deposition statistics. See Elgobashi (1994) for more details of aerosol dispersion and deposition from turbulent flows.

Normally, the aerosol deposition fraction in bends is influenced by the curvature ratio of the bend ( $\delta = R/a$ , see Figure 1.2, where  $R$  is the bend radius and  $a$  is the pipe radius), the flow Reynolds number (which is the inverse of the non-dimensional viscosity) and the Stokes number (which is roughly the non-dimensional particle mass). The Reynolds number is based on the internal diameter of the tube or pipe,  $2a$ , and is defined as follows:

$$\text{Re} = \frac{2aV}{\nu} = \frac{2a \frac{Q}{\pi a^2}}{\nu} = \frac{2Q}{\pi a \nu}, \quad (2)$$

where  $V$  is the average fluid velocity into the bend,  $Q$  is the volumetric flow rate, and  $\nu$  is the kinematic viscosity of the fluid. The Stokes number is given by

$$\text{St} = \frac{V \rho_p d_p^2}{18 \mu a} = \frac{\frac{Q}{\pi a^2} \rho_p d_p^2}{18 \mu a} = \frac{\rho_p d_p^2 Q}{18 \pi \mu a^3}, \quad (3)$$

where the aerosol particle density is  $\rho_p$  and the particle diameter is  $d_p$ .

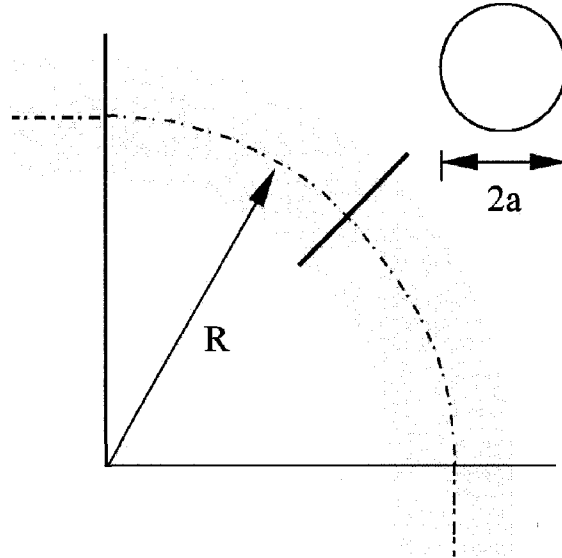


**Figure 1.2: Bend Curvature Ratio,  $\delta = R/a$ .**

A summary of the findings of past studies found in the literature is given in the following sections.

## **1.2 Experimental Studies of Aerosol Deposition in Laminar Flow**

Experimental results for the laminar case have been obtained by Johnston and Muir (1973), Johnston et al. (1977), Pui et al. (1987), and Sato et al. (2003). The experimental results are discussed chronologically in the following paragraphs, and then compiled together in a single graph for comparison (Figure 1.3). Figure 1.3 shows the deposition fraction, DF, as a function of the Stokes number. A zero value for DF means no particle deposition in the bend (or 100% penetration through the bend). A unity value for DF indicates 100% particle deposition on the walls of the bend. It is important to notice that for a constant Reynolds number, the Stokes number will be proportional to the square of a particle size,  $d_p^2$ . The studies are also summarized in Table 1.1. In each of the four cited works, a fluorometric technique was used in which the particles were tagged with a fluorescent substance. When the bend or filter was washed with a solvent, the

fluorescence of the solution could be measured to give the volume concentration of the aerosol particle material.

Johnston and Muir (1973) performed experiments with bends of curvature ratios 5 to 30, with flow Reynolds numbers 100 to 1000. Since the Reynolds number, the curvature ratio, and the Stokes number were all changed among experiments it is difficult to interpret the results; however, a strong, non-linear Stokes number effect on the deposition fraction was indicated.

Johnston et al. (1977) performed experiments at non-constant Reynolds numbers and indicated that the effect of the curvature ratio on the deposition fraction is insignificant. The effect of the flow Reynolds number was not apparent. A plot of their results at varied Reynolds numbers (142-944) with similar curvature ratios, are shown in Figure 1.3.

Pui et al. (1987) performed experiments for flow Reynolds numbers 100 and 1000. For the Reynolds number of 100, the curvature ratio was 7. For the Reynolds number of 1000 the curvature ratio was 5.6 or 5.7. According to their results, the effects of the Reynolds number and/or the curvature ratio are significant. It is not possible to separate the curvature ratio effect from the Reynolds number effect, since both parameters were changed at the same time. A visual examination of the deposition pattern also revealed that the secondary flow (described in section 2.8) strongly influenced the deposition pattern.

Sato et al. (2003) performed experiments at very low Reynolds numbers,  $Re = 3.4$  at a curvature ratio of 3.6, and  $Re = 4.8$  at a curvature ratio of 4.7. The results are similar to those of other studies, and are shown in Figure 1.3.

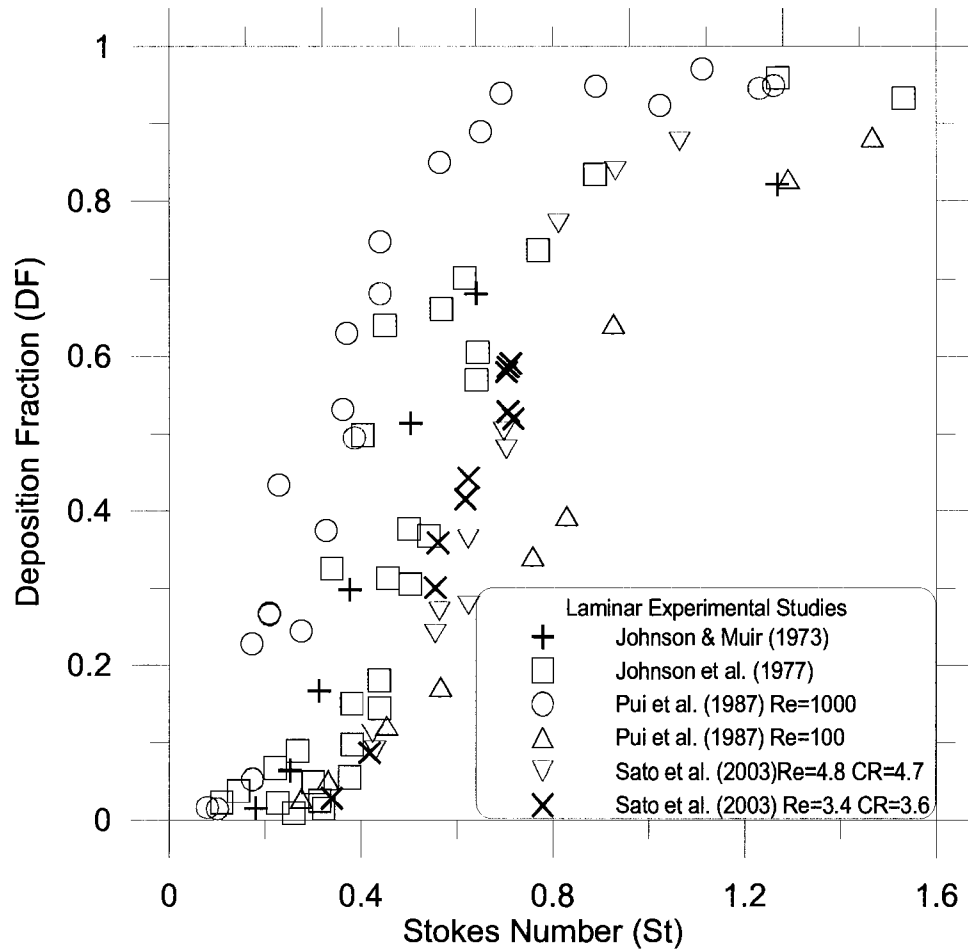


**Figure 1.3: Laminar Experimental Studies**  $\left( St = \frac{\rho_p d_p^2 Q}{18\pi\mu a^3} \right)$

In conclusion, past experimental results for the laminar case indicate a strong non-linear effect on the deposition fraction due to the Stokes number, and a possible significant increase due to an increased flow Reynolds number. The effect due to the curvature ratio is uncertain. The studies are summarized in Table 1.1 below.

**Table 1.1 Summary of the Laminar Experimental Studies**

<b>Study</b>	<b>Measurement Technique</b>	<b>Conclusions</b>
Johnston and Muir (1973) Re = 100 to 1000 CR = 5 to 30 St = 0.1 to 0.7	Fluorometric (particles are tagged with a fluorescent marker)	Non-linear St effect.
Johnston et al. (1977) Re = 100 to 1000 CR = 8 to 25 St = 0.05 to 0.8	Fluorometric. Also used a spinning disc atomizer to generate the aerosols.	Non-linear St effect. No effect due to curvature ratio.
Pui et al. (1987) Re = 100, CR = 7, St = 0.3 to 1.5 Re = 1000, CR = 5.7, St = 0.1 to 1.3	Fluorometric. Used a vibrating orifice aerosol generator.	Non-linear St effect. Possible Re or curvature ratio effect.
Sato et al. (2003) Re = 3.4, CR = 3.6, St = 0.3 to 0.7 Re = 4.8, CR = 4.7, St = 0.4 to 1.1	Fluorometric. Used a collision atomizer for aerosol generation.	Non-linear St effect.

### **1.3 Theoretical Studies of Aerosol Deposition in Laminar Flow**

Theoretical calculations for the laminar case have been made by Landahl and Hermann (1949), Hacker et al. (1953), Yeh (1974), Cheng and Wang (1975), Crane and Evans (1977), Cheng and Wang (1981), and Tsai and Pui (1990). The theoretical results are discussed chronologically and then compiled in Figure 1.4. In general, calculations use either the standard Stokes law of drag, or a modified form of Stokes drag law to more accurately reflect the drag experienced by a particle when the particle Reynolds number is greater than 1 (explained in section 2.5). The particle Reynolds number is the

Reynolds number based on the particle diameter and the slip velocity of the particle relative to the fluid.

Landahl and Hermann (1949) calculated the deposition fraction for a flow in a 90° bend with a parabolic velocity profile, for Reynolds numbers of 3140 and 6250, with the Stokes drag law. The curvature ratio was either 1 or 5. No significant difference between the deposition fractions using these different curvature ratios was detected. Also no differences were reported between the results for the different Reynolds numbers.

Hacker et al. (1953) used a potential flow model. The flow-field used was two-dimensional, with two streamlines representing the inside and outside of the bend. The bend was not quite circular, but had a curvature ratio of about 8. They used a non-Stokes drag law (see section 2.5). Due to this drag law, there was a significant Reynolds number effect. At higher Reynolds numbers, the drag on the particle is greater than that due to Stokes drag, causing the effective inertia of the particle to be reduced, which causes reduced deposition fraction, as is further detailed in section 2.5 (see specifically equations 29 and 30).

Yeh (1974) derived an analytical solution, assuming the Stokes drag law and slug flow. His result for a 90° bend in a circular pipe is:

$$DF = 1 - \frac{2}{\pi} \cos^{-1}\left(\frac{\pi}{2} St\right) + \frac{1}{\pi} \sin\left[2 \cos^{-1}\left(\frac{\pi}{2} St\right)\right] \quad (4)$$

This indicates that the curvature ratio is unimportant, as well as the flow Reynolds number.

Cheng and Wang (1975) also derived an analytical solution. They assumed a forced vortex flow, with the axis of the vortex at the centre of curvature of the bend, and

assumed the Stokes drag law. The Reynolds number effect was found to be zero. The effect of the curvature ratio was found to be insignificant for curvature ratios between 4 and 30. The case for a curvature ratio equal to 5 is plotted in Figure 1.4.

Crane and Evans (1976) provide numerical solutions for curvature ratios of 4 to 20 and Reynolds numbers of 100 000 to 10 000 000. They used a primary potential flow upon which they superimposed a secondary flow, represented as vorticity convected by the primary flow. The particle motion was determined by a drag coefficient based on the particle Reynolds number (non-Stokes drag law. See section 2.5). This resulted in a small Reynolds number effect on the deposition fraction. The higher Reynolds number resulted in a lower deposition fraction. The effect of the curvature ratio was insignificant. Their Stokes law case (particle Reynolds number of zero) with a curvature ratio of 20 is plotted in Figure 1.4.

Cheng and Wang (1981) used a developed laminar flow-field, which includes secondary flow to improve their earlier prediction. The Stokes drag law was used and the curvature ratio was 8. The influence of the Stokes number was consistent with previous predictions and experiments. They found a strong Reynolds number effect where higher Reynolds number resulting in more deposition, contrary to the earlier predictions. Their results for Reynolds numbers of 100 and 1000 are plotted in Figure 1.4.

Tsai and Pui (1990) extended the previous prediction of Cheng and Wang (1981) by numerically modeling a developing flow-field and examining the effects of the curvature ratio and the inlet velocity profile. They used a correction to the Stokes drag law based on the particle Reynolds number. They obtained a significant curvature ratio effect, as well as a significant flow Reynolds number effect. There was notably more

deposition for significantly smaller curvature ratios and for significantly higher Reynolds numbers. Their results for a Reynolds number of 100 with a curvature ratio of 7 and for a Reynolds number of 1000 with curvature ratios of 5.7 and 50 are plotted in Figure 1.4.

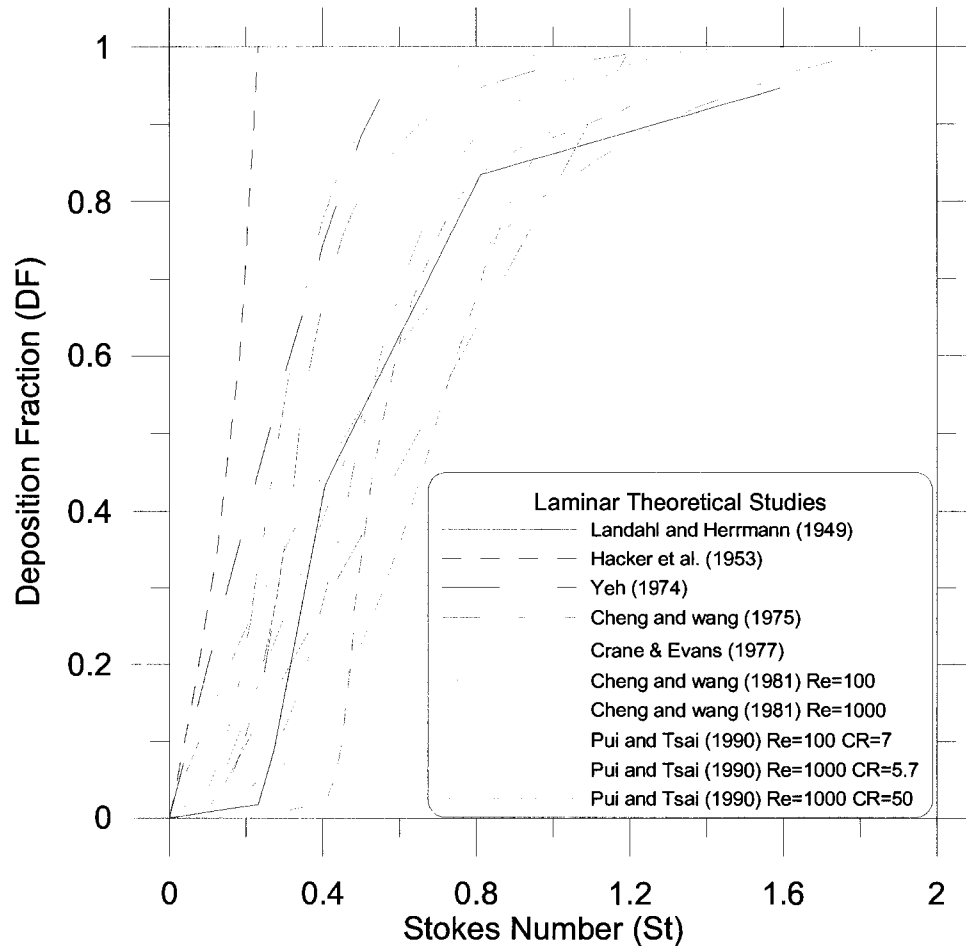


**Figure 1.4: Laminar Theoretical Studies**  $\left( St = \frac{\rho_p d_p^2 Q}{18\pi\mu a^3} \right)$

In conclusion, based on the most rigorous results of Cheng and Wang (1981) and Tsai and Pui (1990), significantly smaller curvature ratios exhibit significantly more deposition, and significantly higher Reynolds numbers exhibit significantly more deposition; however, there is disagreement among some of the cited authors with these conclusions. The studies are summarized in Table 1.2 below.

**Table 1.2 Summary of the Laminar Theoretical Studies**

<b>Study</b>	<b>Calculation Technique</b>	<b>Conclusions</b>
Landahl and Hermann (1949) Re = 3140 to 6250 CR = 1 to 5, St $\approx$ 0.1 to 1.0	Parabolic velocity profile and Stokes drag.	St effect, but no effect due to Re or curvature ratio.
Hacker et al. (1953) Re = 0 to 90 000 000 CR $\approx$ 8, St = 0 to 0.9	Potential flow and non-Stokes drag.	St and Re effect. Higher Reynolds numbers produce smaller deposition fractions.
Yeh (1974) Re arbitrary CR arbitrary, St = 0 to 0.64	Slug flow, and Stokes drag.	St effect, but no effect due to Re or curvature ratio. DF=1 at St=0.64
Cheng and Wang (1975) Re arbitrary CR = 5 to 30, St = 0 to 2.0	Forced vortex flow, with Stokes drag.	St effect, but no effect due to Re or curvature ratio.
Crane and Evans (1977) Re = 100 000 to 10 000 000 CR = 4 and 20, St = 0 to 1.2	Primary potential flow convecting a secondary flow, with non-Stokes drag.	St effect, insignificant curvature ratio effect, and a minor Re effect (smaller deposition with higher Re)
Cheng and Wang (1981) Re = 100 to 4000 CR = 8, St = 0 to 1.2	Fully-developed Laminar flow, with Stokes drag.	St effect, and a strong Re effect (higher Re have more deposition).
Tsai and Pui (1990) Re = 100 to 3000 CR = 5.7 to 50, St = 0 to 1.6	Developing flow-field, with non-Stokes drag.	St effect, and significantly more deposition due to higher Re or smaller curvature ratio.

#### **1.4 Experimental Studies for Aerosol Deposition in Turbulent Flow**

The particle deposition measurement results for turbulent bend flows are discussed chronologically, and then compiled in Figure 1.5. Data have been obtained by Pui et al. (1987) for flow Reynolds numbers of 6000 and 10 000. The points for the two Reynolds

numbers appear to lie on the same curve ( $DF = 1 - 10^{-0.963St}$ ). The curvature ratio was 5.7 and the Stokes number was varied between 0.1 and 1.4.

McFarland et al. (1997) performed experiments to determine the effect of the curvature ratio. They performed the experiments at a non-constant Reynolds number, because their numerical predictions for turbulent flow indicated that the Reynolds number had no significant effect on the deposition fraction. To correct for varying lengths along bends of different curvatures, they added straight sections to the ends of the bends so that the total length of each bend was the same. Their results show a strong, statistically significant, curvature ratio effect with higher the curvature ratios having higher deposition fractions. Additional experiments quantified the effect of pinching of a bend cross-section. Pinching of a tube results from bending a straight tube into a circular arc, and is common in tubes used in practice. The results indicate that there is no significant effect for flattening below 25%.

Peters and Leith (2004) performed experiments at very high Reynolds numbers (203 000 and 368 000), in industrial duct bends. The uncertainty in their data is very high, so no conclusions can be drawn regarding the effects of Reynolds number or curvature ratio. Their results for a horizontally-oriented smooth bend are shown below in Figure 1.5.

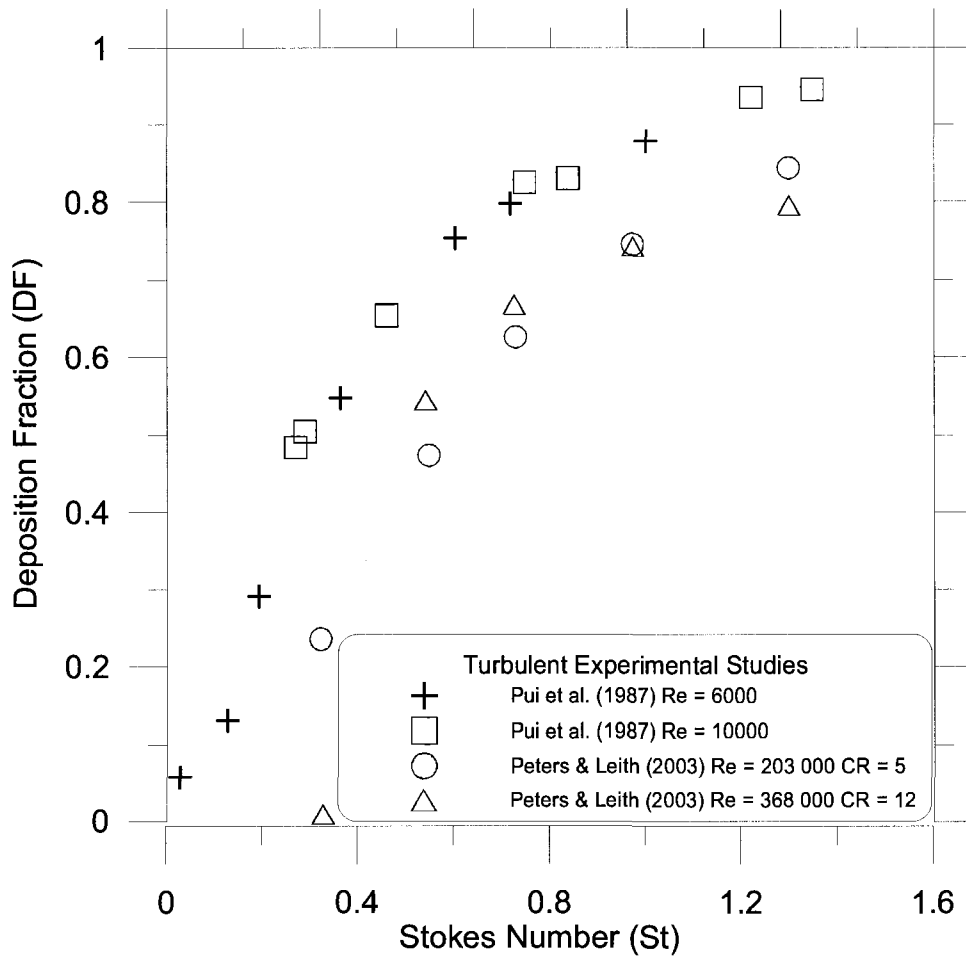


**Figure 1.5: Turbulent Experimental Studies**  $\left( St = \frac{\rho_p d_p^2 Q}{18\pi\mu a^3} \right)$

In conclusion, the experimental results of deposition in the turbulent regime indicate a strong dependence on the Stokes number and a moderate-to-weak dependence on the curvature ratio, with no significant dependence on the flow Reynolds number. The best data for the influence of the Reynolds number appears to be that of Pui et al. (1987). The data of the influence of the curvature ratio is from McFarland et al. (1997), for which the curvature ratio effect becomes significant for curvature ratios below 4 or 5. More deposition occurs at higher curvature ratios, which is opposite what was determined in

the laminar theoretical studies. Data for intermediate to high Re ( $10\,000 < Re < 20\,000$ ) do not yet appear in the literature. The cited studies are summarized in Table 1.3 below.

**Table 1.3 Summary of the Turbulent Experimental Studies**

<b>Study</b>	<b>Measurement Technique</b>	<b>Conclusions</b>
Pui et al. (1987) Re = 6000, 10 000 CR = 5.7 St = 0.1 to 1.4	Fluorometric. Used a vibrating orifice aerosol generator.	St effect but no Re effect
McFarland et al. (1997) Re = 8 300 and 20 000 CR = 1 to 20 St = 0 to 0.7	Fluorometric. Used a vibrating orifice aerosol generator.	St effect. Higher deposition fractions with higher curvature ratios. The Re effect was not systematically examined.
Peters and Leith (2004) Re = 203 000 and 368 000 CR = 1.7 to 12 St = 0.08 to 16	Used industrial ducts bends. Polydisperse glass spheres were accumulated on wire meshes coated with petroleum jelly, both upstream and downstream. They were separated by size using a sedimentation pipette, and weighed.	St effect. Some gravitational settling seen at the higher St

### **1.5 Numerical Studies of Aerosol Deposition in Turbulent Flow**

The numerical deposition results for turbulent bend flows by McFarland et al. (1997) and Breuer et al. (2006) are discussed and then compiled in Figure 1.6. A Lagrangian particle tracking scheme is used to determine the particle trajectories, and the influence of the particles on the flow is considered negligible (called one-way coupling). The flow-field is solved using a turbulence model.

McFarland et al. (1997) used the RANS equations with the Reynolds Stress turbulence model. They used a drag coefficient dependant on the particle Reynolds number. To calculate the instantaneous particle velocity to be used in the particle equation of motion, the turbulent velocity fluctuations had to be modeled. This was done with an eddy interaction model. A study of the effect of the flow Reynolds number indicates it is very insignificant. The Reynolds number based on the pipe diameter was varied from 3 200 to 19 800 at a constant Stokes number, for the Stokes numbers 0.074, 0.30 and 0.67. For a Reynolds number of 8 210, results were calculated for different curvature ratios. Only the curved portion of the bend was included, unlike in their experimental studies. The curvature ratio effect is significant and agrees with their experimental results. Higher curvature ratios result in more deposition.

Breuer et al. (2006) simulated an experimental case of Pui et al. (1987),  $Re=10\,000$ ,  $CR=5.7$ , using a large eddy simulation model. They used the Stokes law of drag, with a correction as a function of particle Reynolds number for higher particle Reynolds numbers. The flow into the bend was fully developed. Their results agree very closely with the experimental data of Pui et al. (1987), and are shown in Figure 1.6.

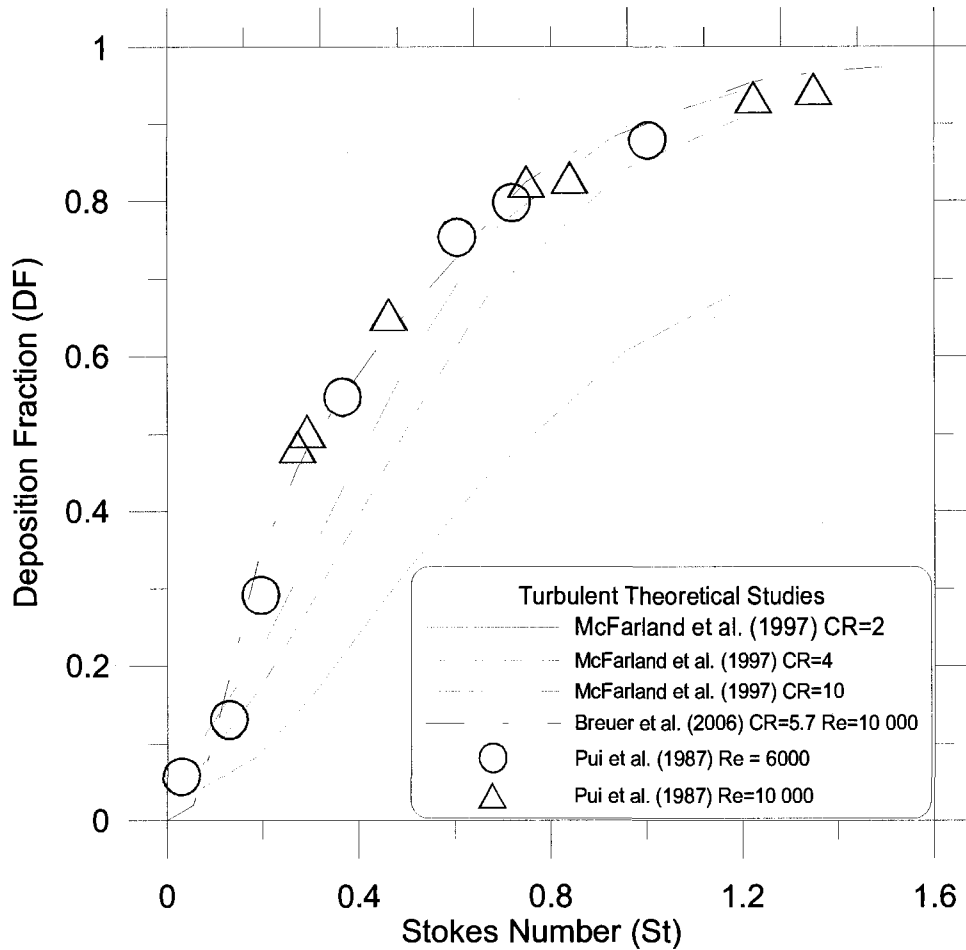


**Figure 1.6: Turbulent Theoretical Studies**  $\left( St = \frac{\rho_p d_p^2 Q}{18\pi\mu a^3} \right)$

In conclusion, theoretical calculations for deposition in the turbulent flow case indicate that the influence of the Reynolds number is insignificant (in the range tested), but that the curvature ratio is significant (for values below 4 or 5), as is the Stokes number. Higher Stokes numbers or curvature ratios (opposite to the laminar flow result) result in higher deposition fractions. The effect of the ratio of the particle density to the fluid density has not been explored, but is assumed small. Since the amount of experimental and theoretical data supporting these conclusions is small, more data could be useful. The cited numerical modeling studies are summarized in Table 1.4 below.

**Table 1.4 Summary of the Turbulent Theoretical Studies**

<b>Study</b>	<b>Calculation Technique</b>	<b>Conclusions</b>
McFarland et al. (1997) Re = 3 200 to 20 000 CR = 1 to 20 St = 0 to 1.2	RANS with Reynolds Stress turbulence model. Lagrangian particle equation with an eddy interaction model, and non-Stokes drag law.	St effect. The influence of Re is insignificant. Higher curvature ratios have higher deposition fractions.
Breuer et al. (2006) Re = 10 000 CR = 5.7 St = 0 to 1.4	LES, and Lagrangian particle tracking with a non-Stokes drag law.	St effect, agreeing closely with experimental results of Pui et al. (1987)

## **1.6 Scope of this Study**

In the present work, experimental data are presented for high flow Reynolds numbers of 10 000, 20 000 and 30 100 and Stokes numbers between 0.1 and 1.0. Previous studies have not experimentally investigated the Reynolds number effect on the deposition fraction for the Reynolds number range of 10 000 to 30 000. The range from 3 200 to 20 000 was studied numerically by McFarland et al. (1997), indicating that the Reynolds number effect on the deposition fraction is negligible. The experiments of Pui et al. (1987) for the Reynolds numbers 6 000 and 10 000 also indicate the effect to be negligible. In the course of this experimental investigation, a small Reynolds number effect for small Stokes numbers was found. Numerical simulations were added to see if they could capture or explain this effect.

A Stokes number range between 0.10 and 1.0 and a Reynolds number range of 10 000 to 30 000 is investigated, since previous studies and practical applications cover this range, or are close to it. For example, the numerical study by Matida et al. (2004) of aerosol deposition in an idealized throat examined flows with  $0.00 < St < 0.53$  and  $2\,700 < Re < 8\,000$  (based on the throat diameter). The numerical study by Ilie et al. (2008) of deposition in the throat with a dry powder Inhaler mouth-piece considered  $St = 0.01$  and  $Re = 9\,000$ .

A brief outline of the theory of aerosol deposition in pipe bends is given in Chapter 2. An explanation of the experiment is given in Chapter 3. A presentation of the uncertainty analysis is given in Chapter 4. The results are given in Chapter 5. The numerical simulations are presented in Chapter 6, and conclusions in Chapter 7.

## **Chapter 2: Theory**

The goal of this chapter is to derive the significant parameters which determine the deposition fraction (DF), and then to convey some understanding of their relative importance. To derive the dimensional parameters, a dimensional analysis is performed (section 2.2). In the following sections these parameters are related to the governing equations. At the end of the chapter (section 2.9), the important parameters are summarized.

### **2.1 Deposition Modes**

There are four mechanisms responsible for the deposition of the particles on the wall of a 90° bend. Gravitational settling (section 2.5) causes particles to deposit as a result of forces due to gravity. Molecular diffusion causes particles to diffuse to the pipe wall (section 2.3). Turbulent dispersion is the dispersion of particles caused by turbulent eddies (section 2.6) and can lead to increased deposition at a wall. The fourth relevant mechanism is inertial impaction (section 2.5), which occurs when particles have too much inertia to follow the flow exactly, causing them to diverge from the general flow direction. For a flow through a bend, these particles deposit due to centrifugal inertia.

If the volume concentration of particles in the flow is very small, the particles do not influence the flow of the air. Their motion is affected by the flow of the air, but the air flow is not affected by their presence (when compared with the overall air flow). This is called one-way coupling. If the presence of the particles affected the flow of the air significantly, it would be called two-way coupling. In this investigation, the volumetric

concentration is about 0.0004% and the mass concentration (or loading) is about 0.3%, which indicates one-way coupling (Elghobashi, 1994).

## 2.2 Dimensional Analysis

It is assumed that the aerosol particle sticks to the pipe wall upon contact. Then the deposition fraction (DF) for a circular 90° bend depends on the geometry and configuration of the test section (pipe internal radius  $a$ , bend radius  $R$ , and gravitational constant  $g$ ), the properties of the flow of air (volumetric flow rate  $Q$ , viscosity  $\mu$ , and density  $\rho$ ), the properties of the aerosol particles (the volumetric flow rate of particles into the bend  $Q_{Pi}$ , the volumetric flow rate of particles out of the bend  $Q_{Po}$ , diameter  $d_p$ , density  $\rho_p$ ), and the diffusion coefficient of the aerosol particles in air  $D$ . The functional dependence can be shown as follows:

$$Q_{Pi} - Q_{Po} = f(Q_{Pi}, Q_{Po}, a, R, Q, \rho, \mu, d, \rho_p, D, g) \quad (5)$$

With these variables, there are three relevant fundamental dimensions: mass, length and time. It is possible according to the Buckingham Pi theorem (see for example Kundhu and Cohen, 2002) to reduce the 11 variables into 8 (11 minus 3) dimensionless variables. Three of the dimensional variables that together contain all 3 dimensions, and which cannot be combined as products to form a non-dimensional variable are chosen ( $Q$ ,  $\rho$ ,  $\mu$ ). These are combined with the remaining 8 variables in turn to obtain 8 non-

dimensional variables  $\left( \frac{Q\rho}{\mu a}, \frac{Q\rho}{\mu R}, \frac{Q\rho}{\mu d_p}, \frac{D\rho}{\mu}, \frac{\rho_p}{\rho}, \frac{Q_{Pi}}{Q}, \frac{Q_{Po}}{Q}, \frac{Q^3 \rho^5 g}{\mu^5} \right)$ . From these,

alternate variables are chosen by multiplying by constants and forming products of powers of these. The following ones are chosen, and in later sections these are shown to have direct relevance to the equations:

$\frac{Q_{pi}}{Q}$ , which is the volume fraction of particles entering the bend.

$\frac{Q_{po}}{Q}$ , which is the volume fraction of particles leaving the bend.

$\delta = \frac{R}{a}$ , which is the curvature ratio.

$Re = \frac{2Q\rho}{\pi a\mu}$ , which is the Reynolds number based on the pipe diameter and average flow velocity ( $\pi a^2 V$ ).

$St = \frac{\rho_p d_p^2 Q}{18\pi\mu a^3}$ , which is the Stokes number.

$\lambda = \frac{\rho_p}{\rho}$ , which is the density ratio.

$Pe = Re \frac{\mu}{D\rho}$ , which is the Peclet number.

$Ri = \frac{\pi^2 g a^5}{Q^2}$ , which is the Richardson number.

Using these dimensionless groupings, the functional dependence is now,

$$\frac{\frac{Q_{pi}}{Q} - \frac{Q_{po}}{Q}}{\frac{Q_{pi}}{Q}} = DF = f\left(\frac{Q_{pi}}{Q}, \frac{Q_{po}}{Q}, \delta, Re, St, \lambda, Pe, Ri\right) \quad (6)$$

Under the assumption of one-way coupling, the volume fraction does not influence the flow. Also, for the same reason, particle interactions can be ignored. Then, the only way for the volume fractions of the particles to influence the deposition fraction is by molecular diffusion. The Peclet number is the inverse of the non-dimensional

diffusion coefficient, and is very large for the flows under consideration ( $Pe > 6.25 \times 10^5$ ), so molecular diffusion can be ignored (see section 2.3). This means that the two volume fractions and the Peclet number can be removed from the right hand side, resulting in:

$$DF = f(\delta, Re, St, \lambda, Ri) \quad (7)$$

The Richardson number represents the magnitude of the influence of gravity on the flow-field and on the particles in the flow-field, and is very small relative to other terms ( $Ri < 2.1 \times 10^{-4}$ ), so gravitational effects will be ignored. This results in:

$$DF = f(\delta, Re, St, \lambda) \quad (8)$$

Cheng and Wang (1981) reported that the deposition fraction depends on  $\delta$ ,  $Re$ ,  $St$ , the freestream particle Reynolds number ( $Re_{p,\infty} = \frac{V\rho d_p}{\mu} = \frac{4Q\rho}{\pi d\mu}$ ), and  $\frac{d_p}{2a}$ . It is easy to reduce the Cheng and Wang conclusion to the one given here. Note that:

$$\frac{d_p}{2a} = \frac{Re_{p,\infty}}{Re} = 3\sqrt{\frac{St}{\lambda Re}} \quad (9)$$

Then, the freestream particle Reynolds number, and the term  $\frac{d_p}{2a}$ , called the interception parameter, can be written as functions of the other parameters, resulting in:

$$DF = f(\delta, Re, St, \lambda) \quad (10)$$

It is important to note that other factors could be relevant that have not been explicitly considered. The roughness of the pipe walls would have some effect. For this study, it is assumed that the walls are smooth. It is also assumed that the pipe cross-section is circular. Finally, the particle material is assumed to be non-volatile (has a low

vapour pressure), such that the evaporation rate is insignificant (which is the case with the Vitamin E aerosol material used in this study).

### 2.3 Molecular Diffusion

Particle diffusion due to random molecular motion can be quantified in unsteady flow by Fick's second law of diffusion (see for example Reist, 1984), which for incompressible flow is:

$$\frac{\partial c}{\partial t} + u \frac{\partial c}{\partial x} + v \frac{\partial c}{\partial y} + w \frac{\partial c}{\partial z} = D \nabla^2 c, \quad (11)$$

where  $c$  is the number concentration of aerosol particles and  $D$  is the binary diffusion coefficient of the aerosol particles in air. The following non-dimensional variables can be introduced where the superscript <sup>(n)</sup> is used to denote non-dimensionality:

$$\begin{aligned} t^{(n)} &= \frac{Vt}{2a} \\ x^{(n)}, y^{(n)}, z^{(n)} &= \frac{x, y, z}{2a} \end{aligned} \quad (12)$$

A non-dimensional version of Equation 11 is then:

$$\frac{\partial c}{\partial t^{(n)}} + u^{(n)} \frac{\partial c}{\partial x^{(n)}} + v^{(n)} \frac{\partial c}{\partial y^{(n)}} + w^{(n)} \frac{\partial c}{\partial z^{(n)}} = \frac{1}{Pe} \nabla^{2(n)} c \quad (13)$$

The Peclet number is the inverse of the non-dimensional molecular diffusion coefficient, and is defined as:

$$Pe = \frac{2aV}{D} = Re \frac{\nu}{D} \quad (14)$$

A formulation for  $D$  for particles in air is due to Einstein's theory of Brownian motion (see for example Reist, 1984). The basic derivation is roughly as follows. Suppose there is a particle concentration gradient in a certain direction. A plane

perpendicular to this direction will experience a force on it due to the air pressure. The air pressure is due to molecular collisions on the plane. The presence of the particles reduces the number of molecular collisions onto the plane, since the particles displace the air molecules. The result is that the plane will feel a reduced pressure (called the osmotic pressure) proportional to the particle concentration. The osmotic pressure gradient causes the air to move relative to the particles from areas of low particle concentration to areas of high particle concentration, creating a slip velocity between the air and the particles. This slip velocity causes a drag force on the particles, which is approximately given by Stokes law of drag. The force due to the osmotic pressure gradient, per particle, is equated to the Stokes drag force on the particle. The result is an equation for the particle current as a linear function of the particle concentration gradient, the constant of proportionality being the diffusion coefficient,

$$D = \frac{kTC_c}{3\pi\mu d_p} \approx \frac{kT}{3\pi\mu d_p} = \frac{(1.38 \times 10^{-23} \text{ J/K})296\text{K}}{3\pi(1.80 \times 10^{-5} \text{ Nsm}^{-2})d_p} < \quad (15)$$

$$\frac{(1.38 \times 10^{-23} \text{ J/K})296\text{K}}{3\pi(1.80 \times 10^{-5} \text{ Nsm}^{-2})10^{-6} \text{ m}} = 2.4 \times 10^{-11} \text{ m}^2 / \text{s}$$

where  $k$  is the Boltzmann constant,  $T$  is the temperature, and  $C_c$  is Cunningham's slip correction factor. Using this value of the diffusion coefficient, the Peclet number is then very large.

$$Pe > Re \frac{1.5 \times 10^{-5} \text{ m}^2 \text{ s}^{-1}}{2.4 \times 10^{-11} \text{ m}^2 \text{ s}^{-1}} = 6.25 \times 10^5 Re \quad (16)$$

Thus, the non-dimensional diffusion coefficient ( $1/Pe$ ) is very small and molecular diffusion is assumed to be insignificant (and generally should be insignificant for turbulent flows due to a high Reynolds number).

## 2.4 Motion Due To Inertia

The particle motion can be described by Lagrangian coordinates or Eulerian coordinates. The Eulerian description treats the particles as a second fluid phase, giving a two-fluid model of aerosol flow (example Elghobashi, 1994 or Kaimal & Devanathan, 1980). The Lagrangian equation of motion for a particle in a fluid was solved by Maxey and Riley (1983). See Appendix B for a discussion of this derivation. The result (assuming that the particle Reynolds number is negligible and that the particle is small relative to spatial gradients) is:

$$\begin{aligned}
 \underbrace{m_p \frac{d\vec{V}_p}{dt}}_{\text{I particle inertia}} = & \underbrace{m_f \frac{D\vec{V}}{dt}}_{\text{II force exerted on an equivalent fluid particle due to the unperturbed flow}} - \underbrace{\frac{1}{2} m_f \frac{d}{dt} \left( \vec{V}_p - \vec{V} - \frac{1}{40} d_p^2 \nabla^2 \vec{V} \right)}_{\text{III added mass term with Faxen correction}} - \underbrace{3\pi d_p \mu \left( \vec{V}_p - \vec{V} - \frac{1}{24} d_p^2 \nabla^2 \vec{V} \right)}_{\text{IV Stokes drag term with Faxen correction}} \\
 & - \underbrace{1.5 \sqrt{\pi \mu \rho} d_p^2 \int_0^t \frac{d\xi}{\sqrt{t-\xi}} \left( \vec{V}_p - \vec{V} - \frac{1}{24} d_p^2 \nabla^2 \vec{V} \right)}_{\text{V the Basset term with Faxen correction}} d\xi + \underbrace{\bar{g} (m_p - m_f)}_{\text{VI gravitational term (with buoyancy)}} + \underbrace{\bar{F}_{\text{Saffman}}}_{\text{VII Saffman Lift Force}}
 \end{aligned} \tag{17}$$

where  $m_p, \frac{d}{dt}, \vec{V}_p, m_f, \frac{D}{dt}, \vec{V}$  are in turn, the mass of the particle, the total time derivative of the particle, the velocity of the particle, the mass of an equivalent volume of fluid, the total time derivative of the fluid, and the velocity of the fluid. This formula is not an exact solution of the Navier-Stokes equations because it assumes that the particle Reynolds number is negligible and that the particle is small relative to spatial gradients in the flow (Maxey & Riley, 1983). The Saffman force (Saffman, 1965) is perpendicular to the stream-wise direction and is given by:

$$F_{\text{Saffman}} = -81.2\pi^2 \sqrt{\mu\rho} (V_p - V) d_p^2 |\Gamma|^{1/2} \text{sgn}\{\Gamma\}, \tag{18}$$

where  $\Gamma$  is the velocity gradient perpendicular to the stream-wise direction. It represents a lift force resulting from velocity shear, perpendicular to the stream-wise direction. A discussion of the derivation can be seen in Stone (2000). The equation is non-dimensionalized by substituting the following non-dimensional variables:

$$\begin{aligned}
\bar{V}^{(n)} &= \frac{\bar{V}}{V} \\
\bar{V}_p^{(n)} &= \frac{\bar{V}_p}{V} \\
\frac{d}{dt^{(n)}} &= \frac{a}{V} \frac{d}{dt} \quad , \\
\frac{D}{Dt^{(n)}} &= \frac{a}{V} \frac{D}{Dt} \\
\nabla^{2(n)} &= a^2 \nabla^2
\end{aligned} \tag{19}$$

resulting in:

$$\begin{aligned}
\underbrace{St \frac{d\bar{V}_p^{(n)}}{dt^{(n)}}}_{\text{I}} &= \underbrace{\frac{St}{\lambda} \frac{D\bar{V}^{(n)}}{dt^{(n)}}}_{\text{II}} - \underbrace{\frac{St}{2\lambda} \frac{d}{dt^{(n)}} \left( \bar{V}_p^{(n)} - \bar{V}^{(n)} - \frac{1}{10} \left( \frac{d_p}{2a} \right)^2 \nabla^{2(n)} \bar{V}^{(n)} \right)}_{\text{III}} \\
&\quad - \underbrace{\left( \bar{V}_p^{(n)} - \bar{V}^{(n)} - \frac{1}{6} \left( \frac{d_p}{2a} \right)^2 \nabla^{2(n)} \bar{V}^{(n)} \right)}_{\text{IV}} \\
&\quad - \underbrace{\sqrt{\frac{\text{Re}}{8\pi}} \frac{d_p}{2a} \int_0^{t^{(n)}} \frac{d\xi}{\sqrt{t^{(n)} - \xi}} \left( \bar{V}_p^{(n)} - \bar{V}^{(n)} - \frac{1}{6} \left( \frac{d_p}{2a} \right)^2 \nabla^{2(n)} \bar{V}^{(n)} \right)}_{\text{V}} d\xi \\
&\quad + \underbrace{St \text{Ri} \left( 1 - \frac{1}{\lambda} \right) \hat{g}}_{\text{VI}} + \underbrace{\frac{12\sqrt{2}St}{\lambda \sqrt{\text{Re}}} \frac{d_p}{2a} \bar{F}^{(n)}}_{\text{VII}} \quad \text{Saffman}
\end{aligned} \tag{20}$$

The Saffman force was non-dimensionalized analogously to the other terms. Now (see

section 2.2) a substitution is made for the interception parameter  $\left(\frac{d_p}{2a} = 3\sqrt{\frac{St}{\lambda Re}}\right)$ ,

resulting in

$$\begin{aligned}
\underbrace{St \frac{d\bar{V}_p^{(n)}}{dt^{(n)}}}_{\text{I}} &= \underbrace{\frac{St}{\lambda} \frac{D\bar{V}^{(n)}}{dt^{(n)}}}_{\text{II}} - \underbrace{\frac{St}{2\lambda} \frac{d}{dt^{(n)}} \left( \bar{V}_p^{(n)} - \bar{V}^{(n)} - \frac{9St}{10\lambda Re} \nabla^{2(n)} \bar{V}^{(n)} \right)}_{\text{III}} \\
&\quad - \underbrace{\left( \bar{V}_p^{(n)} - \bar{V}^{(n)} - \frac{3St}{2\lambda Re} \nabla^{2(n)} \bar{V}^{(n)} \right)}_{\text{IV}} \\
&\quad - \underbrace{3 \sqrt{\frac{St}{8\pi\lambda}} \int_0^{t^{(n)}} \frac{d\xi}{\sqrt{t^{(n)} - \xi}} \left( \bar{V}_p^{(n)} - \bar{V}^{(n)} - \frac{3St}{2\lambda Re} \nabla^{2(n)} \bar{V}^{(n)} \right) d\xi}_{\text{V}} \\
&\quad + \underbrace{St Ri \left( 1 - \frac{1}{\lambda} \right) \hat{g}}_{\text{VI}} + \underbrace{4 \sqrt{\frac{2St}{\lambda}} \bar{F}^{(n)}_{\text{Saffman}}}_{\text{VII}}
\end{aligned} \tag{21}$$

## 2.5 Discussion of the Particle Equation

The Richardson number (see for example Kundhu & Cohen 2002) is defined as:

$$Ri = \frac{ag}{V^2} = \frac{\pi^2 a^5 g}{Q^2} \tag{22}$$

For the  $Re = 10\,000$  (the smallest  $Re$  used in the experiments presented in this thesis)  $Q =$

75.5 L/min, and since  $a = 5.1$  mm,

$$Ri < \frac{\pi^2 (5.1 \times 10^{-3})^5 9.81}{\left(\frac{75.5}{60000}\right)^2} = 2.1 \times 10^{-4} \tag{23}$$

Similarly, for  $Re = 30\,000$  (the largest  $Re$  used in the current data),  $Ri \ll 1$ . Since the Richardson number is so small in all cases here, it is assumed that the gravitational term can be dropped, which makes gravitational settling an unimportant deposition mechanism (term VI in Equation 21).

All terms with the density ratio and  $Re$  together in the denominator will be small ( $\frac{St}{\lambda Re} < 1.3 \times 10^{-7}$ ) and can be dropped. Also, all terms with  $St$  divided by the density

ratio are assumed small enough to drop (terms II and III;  $\frac{St}{\lambda} < 1.3 \times 10^{-3}$ ). The result is:

$$\underbrace{St \frac{d\vec{V}_p^{(n)}}{dt^{(n)}}}_I = -\underbrace{(\vec{V}_p^{(n)} - \vec{V}^{(n)})}_{IV} - 3 \underbrace{\sqrt{\frac{St}{8\pi\lambda}} \int_0^{t^{(n)}} \frac{d\xi (\vec{V}_p^{(n)} - \vec{V}^{(n)})}{\sqrt{t^{(n)} - \xi}} d\xi}_V + 4 \underbrace{\sqrt{\frac{2St}{\lambda}} \vec{F}^{(n)}_{Saffman}}_{VII} \quad (24)$$

A less certain simplification is to neglect terms V and VII under the assumption that  $St$  is less than 1 and the density ratio,  $\lambda$ , is 770 making the term  $\sqrt{\frac{St}{\lambda}}$  small. In this case, term

IV can be argued to dominate so that:

$$St \frac{d\vec{V}_p^{(n)}}{dt^{(n)}} = -(\vec{V}_p^{(n)} - \vec{V}^{(n)}) \quad (25)$$

The inherent simplicity of Equation 25 is also an important justification for neglecting terms V and VII of Equation 24. Equation 25 is the Stokes solution for uniform, steady flow (the unperturbed velocity field has a uniform velocity) and is called Stokes law of drag.

The assumption of a small particle Reynolds number, introduced with Equation 17, is potentially limiting. In the present experiments, for a density ratio of 770, a Stokes

number between 0.1 and 1.0, and a Reynolds number between 10 000 and 30 000 the following bounds on the particle Reynolds number can be made:

$$\begin{aligned} \text{Re}_p < \text{Re}_{p,\infty} &= 3\sqrt{\frac{St \text{Re}}{\lambda}} \\ 3\sqrt{\frac{0.1 \times 10000}{770}} &= 3 < \text{Re}_{p,\infty} < 3\sqrt{\frac{1.0 \times 30000}{770}} = 19 \end{aligned} \quad (26)$$

The particle Reynolds number uses the slip velocity between the particle and the fluid, whereas the freestream particle Reynolds number ( $\text{Re}_{p,\infty}$ ) uses the average fluid velocity. Since the particle Reynolds number could be relevant, the validity of the particle equation (21) is reduced. Therefore, a more reasonable approach is to replace the Stokes drag assumption for the particle drag ( $C_{D,Stokes} = 24/\text{Re}_p$ ) with a drag calculation assuming uniform, steady flow with arbitrary particle Reynolds number. For steady, uniform flow, the particle drag coefficient is

$$C_D = \frac{F_{Drag}}{\frac{1}{2} \rho A_p |V_p - V|^2}, \quad (27)$$

where  $A_p$  is the cross-sectional area of the particle, and  $F_{Drag}$  is the drag force.  $C_D$  is a function of the particle Reynolds number and the Richardson number (see for example Kundhu and Cohen, 2002). Since the Richardson number is small, it can be neglected. Thus, multiplying Equation 25 by  $C_D/C_{D,Stokes}$ , the equation of motion of a spherical particle for steady, uniform flow is then (Brun et al. 1953):

$$St \frac{d\vec{V}_p^{(n)}}{dt^{(n)}} = -\frac{C_D \text{Re}_p}{24} (\vec{V}_p^{(n)} - \vec{V}^{(n)}) \quad (28)$$

This is the common form of the particle equation of motion used for numerical calculations. An empirical relation for the drag coefficient as a function of the particle

Reynolds number is substituted for the drag coefficient. It is used as an approximation to the non-steady case. Since the drag relations that are used give a larger drag force than the Stokes drag force when the particle Reynolds number is larger than 1 (i.e.,  $\frac{C_D \text{Re}_p}{24} > 1$ ), the effect of using a non-Stokes drag law in this equation is to effectively

reduce the Stokes number. The following relations hold (see Equation 9):

$$\text{Re}_p = \frac{|\vec{V}_{rel}|}{V} \text{Re}_{p,\infty} = 3 |\vec{V}_p^{(n)} - \vec{V}^{(n)}| \sqrt{\frac{\text{Re} St}{\lambda}}, \quad (29)$$

where  $\vec{V}_{rel} = \vec{V}_p - \vec{V}$ . Then, the simplified equation of motion can be written as:

$$St \frac{d\vec{V}_p^{(n)}}{dt^{(n)}} = - \frac{|\vec{V}_{rel}^{(n)}| \vec{V}_{rel}^{(n)}}{8} \sqrt{\frac{\text{Re} St}{\lambda}} C_D \left( V_{rel}^{(n)}, \sqrt{\frac{\text{Re} St}{\lambda}} \right) \quad (30)$$

The non-dimensional inertia of the particle for an arbitrary particle Reynolds number is a function of the Stokes number and  $\frac{d_p}{2a} (= 3 \sqrt{\frac{St}{\lambda \text{Re}}})$ . For the Stokes flow case ( $\text{Re}_p < 1$ ),

$C_D = \frac{24}{\text{Re}_p}$ , so the non-dimensional inertia equals the Stokes number, and the 2<sup>nd</sup>

parameter is unimportant (which would make the density ratio insignificant). As the

particle Reynolds number increases, generally  $\frac{C_D \text{Re}_p}{24}$  becomes larger (Kundhu and

Cohen, 2002). Due to Equation 29, an increase in the flow Reynolds number tends to

increase the particle Reynolds number. This results in the effective non-dimensional

inertia of the particle to be decreased, so that it behaves as if it had a smaller Stokes

number. The end result is that there is a Reynolds number effect on the inertial impaction

mechanism, causing a decrease of the deposition fraction as the Reynolds number

increases (which was seen in some of the laminar theoretical studies in Chapter 1). The

relative importance of this effect indicates the relative importance of the density ratio in this study, since the effect comes from the parameter  $\frac{d_p}{2a} (= 3\sqrt{\frac{St}{\lambda Re}})$ . This means a Re change will have the same effect as a density ratio change, assuming the effect is not due to a change in the flow-field. It will be assumed that this effect is minor, so that

$$DF \approx f(\delta, Re, St) \quad (31)$$

## 2.6 Turbulent Dispersion

Turbulence causes the instantaneous velocity of the flow-field to deviate from the time mean velocity. Typically, the instantaneous flow is broken into components ( $\vec{V} = \vec{V}_m + \vec{V}'$ ), where the superscript ' denotes a velocity fluctuation, and the subscript  $m$  denotes the time mean. When the kinetic energy of the flow-field is averaged, the result is  $\frac{1}{2}V^2 = \frac{1}{2}u_e^2 + \frac{1}{2}v_e^2 + \frac{1}{2}w_e^2 + \frac{1}{2}V_m^2$ . The velocity components are  $(u, v, w)$ . The rms value of the turbulent fluctuations is denoted by the subscript  $e$  (for eddy). This shows that the kinetic energy of the flow exists as two forms: that due to the mean flow, and that due to the turbulence,  $k = \frac{1}{2}(u_e^2 + v_e^2 + w_e^2)$ . The fluctuating velocities due to turbulence cause particles to disperse more throughout the flow. This is referred to as turbulent dispersion. This extra dispersion tends to increase the deposition of the particles on the pipe walls. A brief discussion on how turbulent dispersion can be estimated is provided in the following section.

### 2.6.1 Estimating Deposition From Turbulent Dispersion

Both the velocity magnitude and fluctuation frequencies of turbulence influence the particle motion. Particles of higher inertia will develop a phase lag relative to a turbulent fluctuation, which will cause the magnitude of their response to decrease (Rouhiainen & Stachiewicz, 1970). Consequently, they will track the fluctuations less well. An estimate of the impact of turbulent fluctuations can be made by examining the case for very small Stokes numbers in which flow fluctuations are perfectly tracked. A major assumption that is made in the following analysis is that the turbulent fluctuations are isotropic. This assumption cannot be made close to walls, since a turbulent fluctuation cannot move through a wall and must therefore be smaller in directions normal to walls.

Assuming the turbulent fluctuations to be isotropic, and the Stokes number to be negligible, a particle will undergo a random walk relative to the mean flow streamlines. This means that the direction of each step is random. When there are lots of particles undergoing a random walk, with small distances travelled at each step, the result is a diffusion of the concentration of particles. For molecular diffusion, the diffusion coefficient (based on the molecular theory of gases) is proportional to the rms speed of the molecules and the average distance travelled between collisions (mean free path) (see for example Kundhu and Cohen, 2002). An analogous turbulent diffusion coefficient can also be estimated. The result for small Stokes numbers is that the turbulent diffusion coefficient is equal to the eddy kinematic viscosity used in eddy viscosity turbulence models. The justification for this line of reasoning is given in the following paragraphs.

It is assumed that the properties of isotropic turbulence are determined completely by the turbulent kinetic energy ( $k$ ) and the eddy dissipation rate ( $\varepsilon$ ). To derive a formula

for the eddy diffusion coefficient (or for transport of momentum, the eddy kinematic viscosity), it is required to find an eddy rms speed and an equivalent eddy mean free path (eddy length scale). The rms speed is derived from

$$k = \frac{1}{2}(u_e^2 + v_e^2 + w_e^2) = \frac{3}{2}u_e^2 \quad (32)$$

$$u_e = \sqrt{\frac{2k}{3}}$$

The eddy length scale is given by

$$L_e = f(k, \varepsilon), \quad (33)$$

where  $f$  is an unknown function. By the Buckingham Pi Theorem:

$$L_e \propto \frac{k^{\frac{3}{2}}}{\varepsilon} \quad (34)$$

The result is then that the eddy diffusivity is

$$v_e \propto \frac{k^{\frac{3}{2}}}{\varepsilon} \sqrt{\frac{2}{3}k} \propto \frac{k^2}{\varepsilon}. \quad (35)$$

Equation 35 defines an eddy diffusion coefficient that can be used to estimate the effect of turbulent dispersion on particles with small Stokes numbers. The same argument works whether considering concentrations of particles or concentrations of momentum; therefore it is equivalent to the eddy viscosity used in eddy-viscosity turbulence models.

To adapt this for larger Stokes numbers, the eddy diffusion coefficient must be multiplied by an amplitude ratio. Particles with higher Stokes numbers will have a reduced amplitude of fluctuation. This amplitude ratio can be estimated for any given frequency by studying the response of the Stokes law case of the particle equation (25) for a sinusoidal input of the given frequency (Tavoularis, 2005).

Turbulent diffusion must be compared relative to convection, as seen in the molecular diffusion equation (11). The faster a quantity of the aerosol convects through the bend, the less time it has to deposit due to turbulent diffusion. The result is that (analogous to the Peclet number for molecular diffusion), an important parameter for turbulent dispersion is the Reynolds number based on the eddy viscosity:

$$\text{Re}_{\nu_e} = \frac{V}{\nu_e} \text{Re} \quad (36)$$

For higher Stokes numbers, due to the reduced response of particles to turbulence, the eddy diffusivity must be multiplied by an amplitude ratio, so the diffusive effect diminishes. Also, non-isotropic properties of turbulence were neglected in the derivation, so the use of this close to walls is suspect.

Since the eddy viscosity,  $\nu_e$ , increases as the Reynolds number increases, it is not obvious how an increase in the Reynolds number affects the deposition fraction due to turbulent dispersion. Since the length scales between eddy interactions are not microscopic, the effect of turbulent dispersion is not entirely diffusive. Theoretical and numerical studies on the effect of turbulent dispersion on the deposition rate in pipe flows have shown that particles are able to penetrate right through the near-wall region of low eddy viscosity by free flight (for example, McCoy & Hanratty (1977), and Ganic & Mastanaiah (1981)). The result is that generally particles with higher Stokes numbers deposit at a higher rate in straight pipe flow, even though they respond less to the diffusive effect of turbulence. The smaller particles are not able to as easily penetrate the layer of low turbulence in the boundary-layer sublayer.

### 2.6.2 The Effect of Turbulent Dispersion on the Inlet Particle Distribution

Due to the diffusive effect of turbulence, particles tend to move from high turbulence regions to low turbulence regions (Reeks, 1983). For example, for a fully-developed particle concentration profile in a straight pipe, using the eddy viscosity approximation for turbulent dispersion, the turbulent diffusion equation in the radial direction ( $r$ ) is:

$$\frac{\partial c}{\partial t} = 0 = \frac{\partial(v_e \frac{\partial c}{\partial r})}{\partial r}, \quad (37)$$

so,

$$v_e \frac{\partial c}{\partial r} = \text{constant}. \quad (38)$$

The result would be that the particle concentration would be high where the eddy diffusivity is low, which would be in the boundary-layer sublayer. This does not actually happen though, for the following reason: due to the condition of continuity, this would require the fluid to move in the opposite direction, but the fluid is also driven in the same direction for the same reason.

## 2.7 The Fluid Equations

It is generally believed that the incompressible continuity equation and the Navier-Stokes equation accurately determine the fluid velocity field. These, in turn, are:

$$\nabla \cdot \vec{V} = 0 \quad (39)$$

$$\frac{\partial \vec{V}}{\partial t} + (\vec{V} \cdot \nabla) \vec{V} = -\frac{1}{\rho} \nabla P + \frac{1}{\rho} \vec{g} + \frac{\mu}{\rho} \nabla^2 \vec{V} \quad (40)$$

The pressure is denoted by  $P$ . In Appendix A, these are written for toroidal coordinates and non-dimensional variables are introduced. The Reynolds number, curvature ratio and

Richardson number are the resulting non-dimensional parameters. Since the Richardson number was already shown to be small, the gravitational force can be neglected as assumed in section 2.2.

## **2.8 Secondary Flow**

Due to the centrifugal inertia of the primary flow, a secondary flow is superimposed on the primary flow. The flow is centrifugally driven outwards, but due to the requirement of mass conservation, it must flow back inwards. The fluid near the centre of the tube has more centrifugal inertia than the fluid close to the walls, so it flows outwards. A pressure gradient causes the flow close to the walls to move inwards. This results in a symmetric pair of counter-rotating vortices. Some investigators have discovered that sometimes (for higher Dean numbers,  $De = \frac{Re}{\sqrt{\delta}}$ ) there are 2 pairs of vortices (4 vortices) instead of 1 (for example the numerical calculation of Dennis & Ng (1982) for fully-developed laminar flow).

The following figure shows the flow-field for the Reynolds 10 000 case from the LES simulation of Breuer et al. (2006). A significant secondary flow pattern, consisting of vortices is seen in the cross-sections.

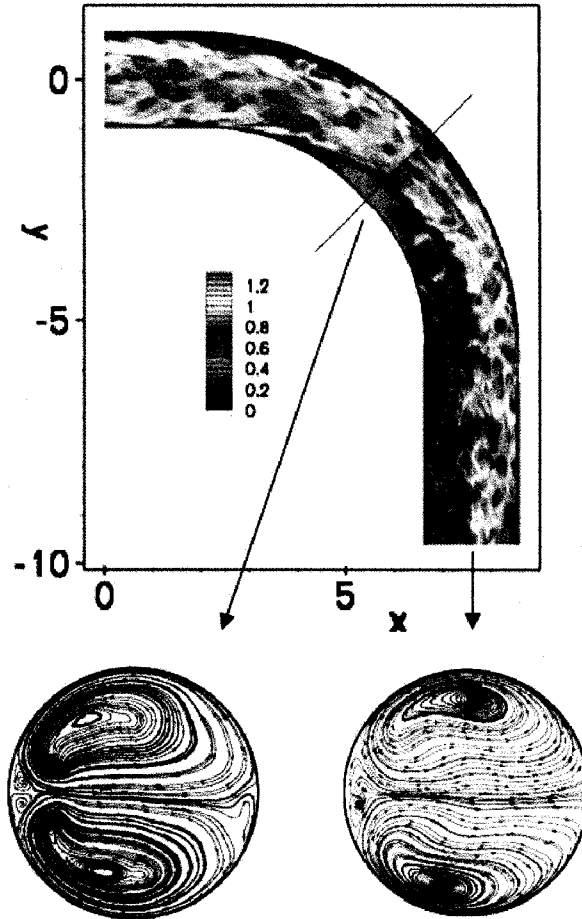


**Figure 2.1: Flow-Field in a 90° Bend Showing Dean Vortices (Breuer et al., 2006).  
The legend refers to the relative velocity magnitude.**

## **2.9 Summary of the Significant Parameters**

The significant parameters derived in this chapter are:

- The density ratio  $\lambda = \frac{\rho_p}{\rho} = 770$
- The curvature ratio  $\delta = \frac{R}{a} = 7.4$
- The flow Reynolds number  $Re = \frac{V2a}{\nu} = \frac{\frac{Q}{\pi a^2} 2a}{\nu} = \frac{2Q}{\pi a \nu}$
- The Stokes number  $St = \frac{V \rho_p d_p^2}{18 \mu a} = \frac{\frac{Q}{\pi a^2} \rho_p d_p^2}{18 \mu a} = \frac{\rho_p d_p^2 Q}{18 \pi \mu a^3}$

## Chapter 3: Experimental Apparatus and Methodology

Experiments were performed to measure total deposition of aerosol particles flowing through a 90° bend for flow Reynolds numbers of 10 000, 20 000, and 30 100 and Stokes numbers based on the particle diameter ranging from 0.1 to 1.0. Figure 3.1 shows a schematic of the apparatus used. A photograph of the test section is shown in Figure 3.2.

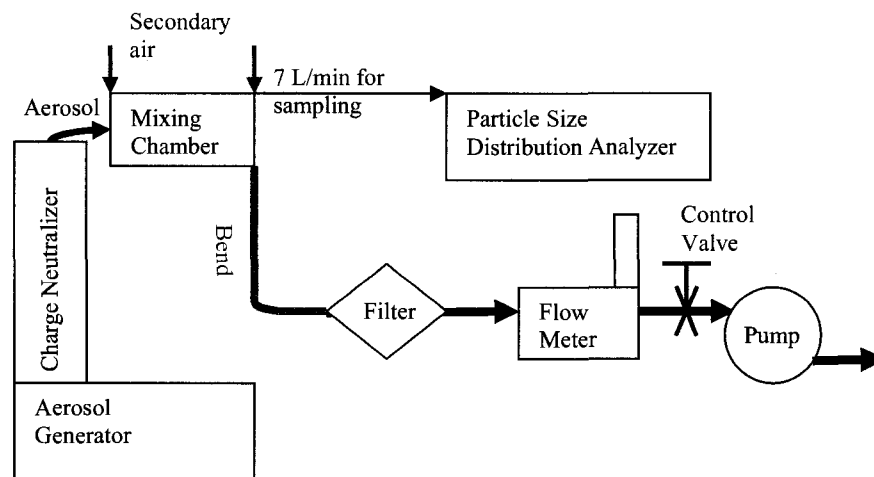
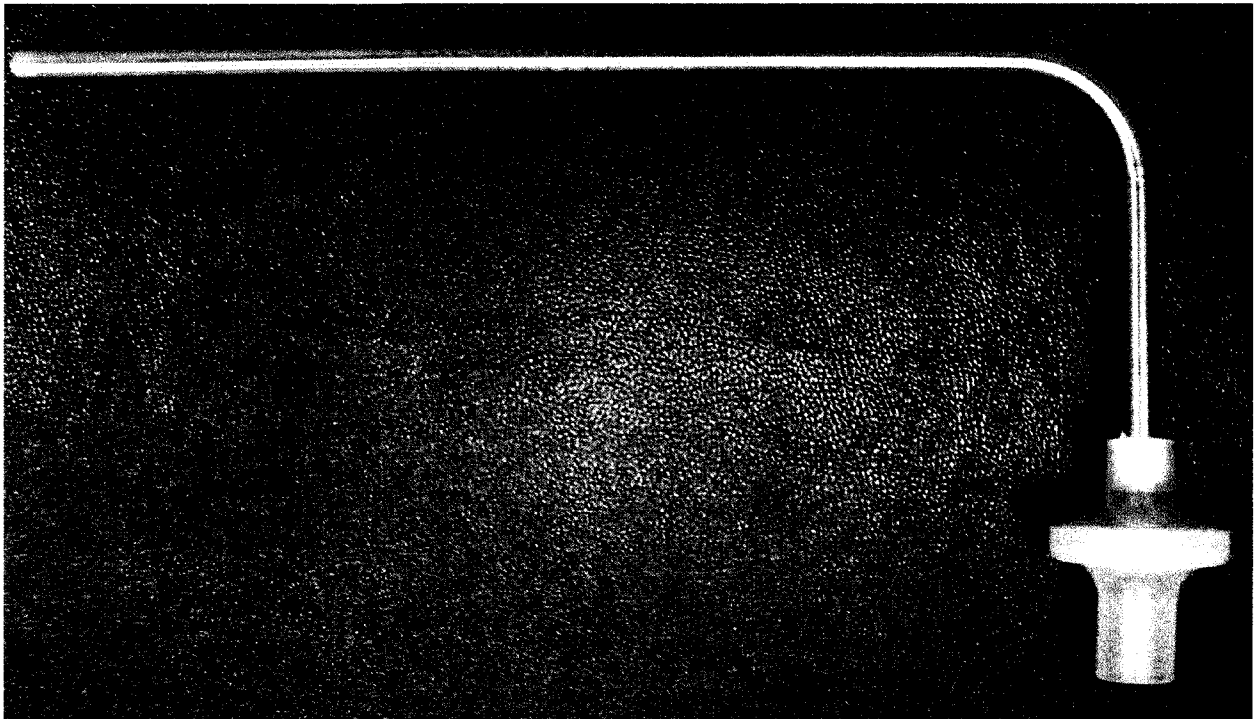


Figure 3.1: Schematic of Experimental Apparatus

The bend was positioned so that the aerosol flowed vertically downwards into the bend. An entrance length of 27 diameters ensured that the turbulent flow entering the test section was fully developed. The entrance length of pipe required for fully developed turbulent flow is  $4.4 Re^{1/6}$  (White, 1998), which equals 24.5 diameters for  $Re = 30\ 000$ , and 10 inches (25.4 cm) for the pipe diameter of 0.405 inches (10.3 cm). The bend geometry is described by the curvature ratio ( $R/a = 7.4$ ). The flow Reynolds number is referenced to the inner diameter of the pipe. Aerosol particles consisting of liquid of

vitamin E were generated as described below and entrained into the air flow before passing through the test section. Vitamin E has been successfully used for similar experiments in the past (for example DeHaan & Finlay, 2001). The ratio of the aerosol particle density to the air density was 770.

A portion of the vitamin E droplets deposit on the bend wall as the aerosol laden flow passes through the bend. Since the vitamin E droplets are liquid and non-volatile, they stick to the wall and do not re-enter the flow. The vitamin E that was deposited is washed from the bend and from the filter, and measured as described in section 3.2 below. The deposition fraction is the ratio of particles deposited on the bend wall to the total number which flowed into the bend.



**Figure 3.2 The 90° Bent Pipe with Downstream Filter**

### **3.1 The Flow System and Aerosol Generation**

A short description of each piece of equipment follows, starting with the aerosol generator and working downstream with the flow. Each piece of equipment can be identified in Figure 3.1.

#### **3.1.1 The Aerosol Generator**

A TSI Model 3450 Vibrating Orifice Aerosol Generator was used to produce mono-disperse aerosol particles (i.e., particles with a very narrow size distribution). The operation principle is described here from the equipment manual (TSI, 2002). The aerosol generator has three main components:

- A jet of solution containing vitamin E dissolved in isopropyl alcohol,
- A small orifice that vibrates, and
- A flow of air that mixes with the aerosol particles.

The jet of liquid was created by pumping the vitamin E (brand Equate<sup>®</sup>) solution out of a syringe with a stepper motor, into tubing that directs the solution to the orifice. The jet operates at a constant volumetric flow rate and as it passes through the small orifice it breaks into uniform size droplets due to the vibration of the orifice. The orifice is mechanically in contact with a piezo-electric ceramic, which is electrically connected to a frequency generator, so that the orifice vibrates at the same frequency as the frequency generator. The orifice can be controlled by varying the frequency of vibration.

The particles which flow from the orifice are dispersed in air (called the dispersion air) and are mixed in a chamber above the orifice. This prevents significant coagulation of the particles. The aerosol flows out of this chamber and is further diluted with a second stream of air. The resulting aerosol consists of a stream of air flowing at

about 70 L/min suspending particles of vitamin E dissolved in isopropyl alcohol. Here or further downstream, the alcohol is fully evaporated, leaving behind spherical droplets of vitamin E.

For a particular setting of the instrument (combination of liquid feed rate and orifice vibration frequency), the final particle size is changed by changing the concentration of vitamin E in the isopropyl solution. The difficult part in operating the aerosol generator is finding settings that produce mono-disperse particles. For a particular setting (combination of liquid feed rate and orifice vibration frequency) the particle size can be calculated. The equation is (TSI, 2002):

$$\frac{\pi}{6} d_p^3 = \frac{Q_s}{f} (C + I)$$

$$d_p = \left( \frac{6}{\pi} \right)^{1/3} Q_s^{1/3} f^{-1/3} (C + I)^{1/3}$$
(41)

where:  $d_p$  is the particle diameter

$Q_s$  is the volume flow rate of the jet {=  $5.44 \times 10^{-9} \text{ m}^3 / \text{s}$  for the syringe pump setting of  $9.9 \times 10^{-4} \text{ cm/s}$ ; 1% bias limit}

$f$  is the vibration frequency of the frequency generator (1% bias limit)

$C$  is the volumetric concentration of the vitamin E (brand Equate<sup>®</sup>) in alcohol { $C = 0.000196 \times \text{Absorbance at } 285\text{nm}$ ; 2% bias limit}, and

$I$  is the residue after evaporation volumetric concentration of the alcohol (40 ppm).

The particle size was measured using the Particle Size Distribution (PSD) analyzer (section 3.1.4). The calculated particle size was used to validate the measured particle size and was not used in the calculations.

### **3.1.2 The Charge Neutralizer**

After leaving the aerosol generator, particles have some electric charge. This is undesirable, because this could affect the deposition fraction results. The TSI Model 3054 Aerosol Neutralizer is used to neutralize this charge. The operation principle is described here as inferred from the equipment manual (TSI, 2003).

A radioactive source (10 millicurie of Krypton-85 gas) is contained in a sealed holder inside a stainless steel tube. The radioactivity (beta decay) releases beta particles (electrons) and gamma particles (photons). These ionize some of the air in the tube into both positive and negative ions. The aerosol flows through the tube, and these ions combine with and neutralize the excess charge on the aerosol particles.

### **3.1.3 The Mixing Chamber**

After passing through the neutralizer, the aerosol enters a mixing chamber where it is mixed with filtered secondary air from the room. This chamber helps to ensure complete mixing of the aerosol particles in the air and allows the flow rate to be controlled by the introduction of secondary air.

### **3.1.4 The Particle Size Distribution Analyzer**

From the mixing chamber, some of the aerosol is fed into the TSI PSD 3603 Particle Size Distribution Analyzer (PSD). Although the final particle size can be calculated using the equation shown above in section 3.1.1, direct measurements using the PSD were deemed to be more accurate and were used in the reporting of all results. To verify that the results were consistent between these two options, the data was also plotted using the calculated particle size. The same conclusions were seen as with the measured particle

size data. As well, the PSD was used to ensure that the aerosol droplets were monodisperse. The description of this device is based on the equipment manual (TSI, 2004).

Air is bled from the mixing chamber at 7 L/min into the device. Most of the air (6 L/min) is diverted and filtered, and then re-directed through a nozzle. Inside this nozzle is a smaller inner nozzle, through which the rest of the aerosol passes (1 L/min). The aerosol exits this inner nozzle into the sampling area. Sheath air from the outer nozzle (6 L/min) surrounds the aerosol, causing the flow from the inner nozzle to form a central region of more uniform flow. This makes the drag force on the particles simpler to calculate (see section 2.5 for reference). The aerosol is accelerated to a high velocity in a narrow stream. Due to the inertia of the aerosol particles, they lag behind. During this acceleration, the particles pass individually through a pair of overlapping laser beams. Light is scattered off the particle from each beam, and passes through a lens to an avalanche photo-detector. This produces a distinct double-crested electrical pulse. The time between the crests is determined by the drag force on the particle (section 2.5). The flow conditions are constant, and the instrument is calibrated to the Stokes number (and is insensitive to the density ratio), or equivalently, the aerodynamic diameter (particle diameter multiplied by the square root of the specific gravity) (see Chen et al., 1985). The bias limit of the measurement is 2%. The air continues into a diffuser and the particles are trapped downstream.

The software graphs the particle size versus the relative volume of particles. By monitoring this graph, a judgement is made whether the aerosol is monodisperse or not. A sample size distribution plot is shown in Figure 3.3 below.

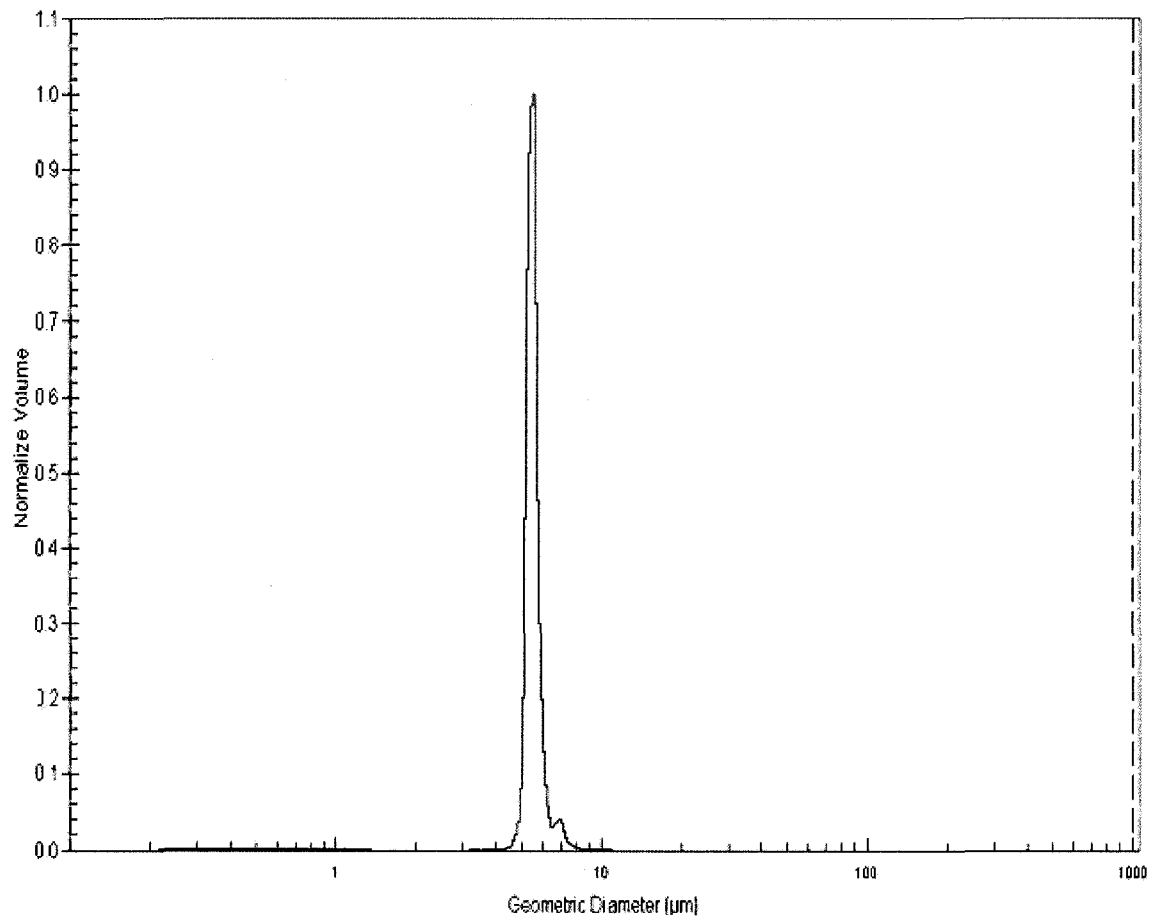


**Figure 3.3: Typical Particle Size Graph,  $Re = 20\ 000$ ,  $St = 0.47$  ( $d_p = 5.41\ \mu m$ )**

The size used is the mass median diameter, for which half of the mass of the aerosol has a smaller diameter, and half of the mass has a larger diameter.

### **3.1.5 The Test Section**

A 90° bend of stainless steel tubing was used for all experiments (see Figure 3.2). The inside diameter of the tubing was  $1.03\pm 0.01$  cm ( $0.405\pm 0.005$  inches). The straight section before the bend was 27.9 cm long (11 inches or 27 diameters) to produce fully-developed flow. The straight section after the bend was 8.9 cm long (3.5 inches). The radius of the bend was  $3.81\pm 0.25$  cm ( $1.5\pm 0.1$  inches).

The curvature ratio (bend radius divided by inside radius of the tube) was 7.4. A tube bender was used to make the bend. The brand name of the bender is Ridgid. It is a hand-held bender for an outside pipe diameter of  $\frac{1}{2}$  inches and a bend radius of 1.5 inches. The tube was bent slightly more than 90 degrees, because some small amount of bending occurred just before and just after the bend. This ensured a 90 degree bend in the bend portion. The tube was filled with sand during bending to reduce flattening of the cross-section. The degree of flattening due to bending is approximately 5% of the diameter, so no influence of this effect on the deposition fraction results is expected (McFarland et al., 1997). This was determined by measuring the outside pipe diameter after bending. The diameter was reduced by about 5% due to pinching.

### **3.1.6 The Filter**

Marquest Respigard-II 303 Bacterial filters manufactured by Vital Signs Inc. were used as the filter downstream of the bend (see Figure 3.2). A new filter was used for each experiment. The filter material was spun bound polypropylene. The particles are trapped by impaction. To verify that the filter was trapping practically all particles, some experiments were performed with 2 filters connected in series, and each filter washed

(see section 3.2.1 below) and analyzed separately. The concentration of vitamin E in the 2<sup>nd</sup> filter was below detectable limits.

### 3.1.7 The Pressure Gauge

A dial vacuum gauge was used upstream of the mass flow-meter (ANSI standard Grade A). This allowed a calculation of the air density at this point, through the ideal gas law (assuming a constant temperature). From the density and the mass flow rate, the volumetric flow rate was calculated. The bias error is 2% full scale in the range of interest, which equals 2 kPa (0.6 inHg.) The resolution is 1.7 kPa (0.5 inHg).

The density ratio depends on the actual air density in the test section. The Stokes number depends on the actual volumetric flow rate in the test section, so it also depends on the actual density in the test section, since the mass flow is measured by the mass flow meter. The gauge pressure measured at the gauge location was small enough for the Re 10 000 and Re 20 000 cases to be used for the gauge pressure in the bend without loss of accuracy. For the high Re case, the flow was split just downstream of the filter so that some could go through each of the 2 flow meters used for this case. This resulted in extra losses in a bend, fittings, and extra piping, so instead, a different estimating procedure was used for the Re 30 100 case.

For the Re 30 100 case, the pressure entering the entrance pipe is assumed to be atmospheric (since it comes directly from the mixing chamber, which has secondary air ports connecting it to the atmosphere). Then, the pressure entering the bend would be atmospheric, minus the pressure loss in the entrance pipe. The pressure loss in the pipe is

$$\text{(White, 1998)} f \frac{L}{2a} \frac{V^2}{2} = 0.024(27) \frac{(42 \text{ m/s})^2}{2} = 0.7 \text{ kPa} , \text{ where } f \text{ represents the friction}$$

factor and  $L$  represents the length of the inlet pipe. As well, the pressure drop calculated in the simulation (Chapter 6) in total through the entrance pipe, bend, and exit pipe, was 1.3 kPa, so a reasonable bias limit to use for the pressure in the test section is 1.5 kPa (see chapter 4). The pressure used for this case is then  $(101.3 - 0.7) \pm 1.5$  kPa.

### **3.1.8 The Mass Flow Meter**

The Brooks Instrument Model 5863S thermal mass flow meter was used to measure the flow rate. The principle of operation given here is based on the equipment manual (Brooks Instrument, 2000).

Air is diverted through a bypass channel, where it flows past a heating element. The power supplied to the heating element is known or constant. Two sensing elements, one upstream and one downstream from the heating element, measure the temperature difference between upstream and downstream. This temperature difference is proportional to the mass flow rate.

The two sensing elements are connected in a bridge circuit. The resistance in each element depends on its temperature. Using the bridge circuit, the difference in resistance between upstream and downstream can be determined, which gives the temperature difference. The meter gives a voltage output signal proportional to the mass flow rate. This output signal is fed into a National Instruments data acquisition card. This card is read using the LabView software.

The meter has a maximum flow rate of 150 SLPM (where SLPM is the standard litres per minute of air at a pressure of 101.325 kPa and a temperature of 0°C), which corresponds to a Reynolds number of 20 000 for the current test section. The bias error is

0.2% of the full scale (0.3 SLPM) and 0.7% of the operating range. There is a set-point bias error, due to the drift and oscillation in the flow-rate reading during the experiment, apparently equal to 0.2%. For the Reynolds number case of 30 000, the flow meter was connected in parallel with a second thermal mass flow meter. The second flow meter is an Aalborg mass flow controller with a maximum flow rate of 150 SLPM, and bias of 2% full scale (3 SLPM).

### **3.1.9 The Vacuum Pump**

A Welch dry vacuum pump Model 2585B was used to drive the flow. The pump was placed downstream of the mass flow meter and manual control valve, and was capable of pulling about 200 L/min through the system. For the Reynolds 30 100 case, two identical pumps were connected in parallel, one downstream of each mass flow meter.

## **3.2 Procedure for Measuring Deposition**

In a typical experiment the aerosol flow was passed through the test section at steady state for 0.5 hours to ensure sufficient deposition for accurate measurement. As well, each experiment was repeated at least 3 times to minimize the precision uncertainty as explained further in Chapter 4. The length of the experiment was varied (in an uncontrolled way) for each data point, and between data points. It is expected that this variation is reflected in the precision uncertainty of the final data (see section 4.2). After the flow part of the experiment was finished, the vitamin E was washed from the bend and from the filter (including the straight section of pipe immediately downstream of the

bend). Then the amount of vitamin E was measured with the spectrophotometer. This enabled the deposition fraction to be calculated

### **3.2.1 Wash Procedure**

First the entrance section was cleaned by soaking it in acetone to remove and dispose of any vitamin E deposited upstream of the test section as shown in Figure 3.4. The exit section was then soaked in a fixed amount methanol to remove the vitamin E as shown in Figure 3.5. This methanol/vitamin E solution from the exit section wash was then poured back and forth through the filter (Figure 3.6). Because the filter pad absorbed a significant portion of the total methanol used, to obtain sufficient mixed solution for sampling in the spectrophotometer, a portion of the methanol solution that was absorbed into the filter pad was removed by pipetting it with a disposable Pasteur pipette. This solution was identified as the filter solution. To create the bend solution, a fixed quantity of methanol (same as used for the filter) was poured into the bend, and the bend was left to soak for at least 5 minutes as shown in Figure 3.7. The spectral absorbance of each solution was then measured in the spectrophotometer to determine the concentration of vitamin E in solution. Since the amount of methanol used in the wash procedure was precisely measured, the mass of vitamin E can be determined and hence the deposition fraction in the bend can be calculated. A detailed uncertainty analysis of this procedure is presented in the following chapter.

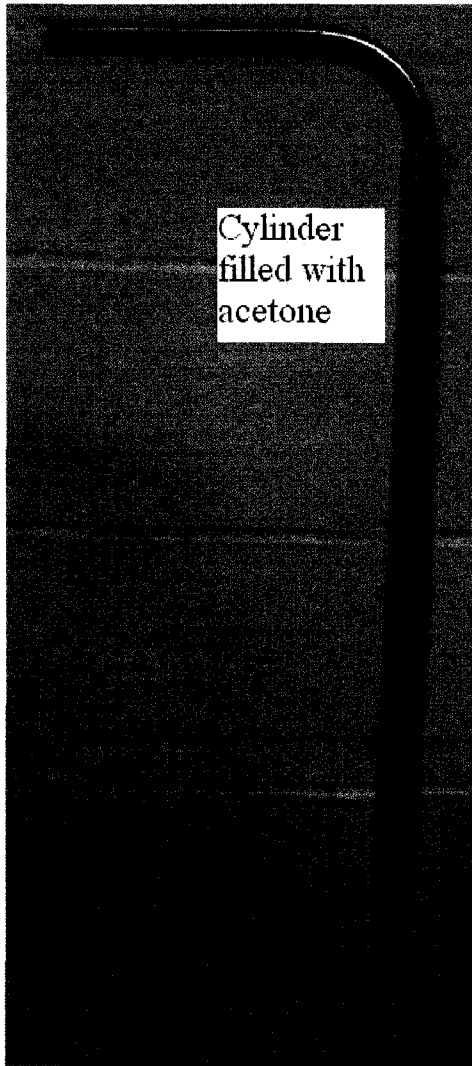


**Figure 3.4: Entrance Section Acetone Wash**

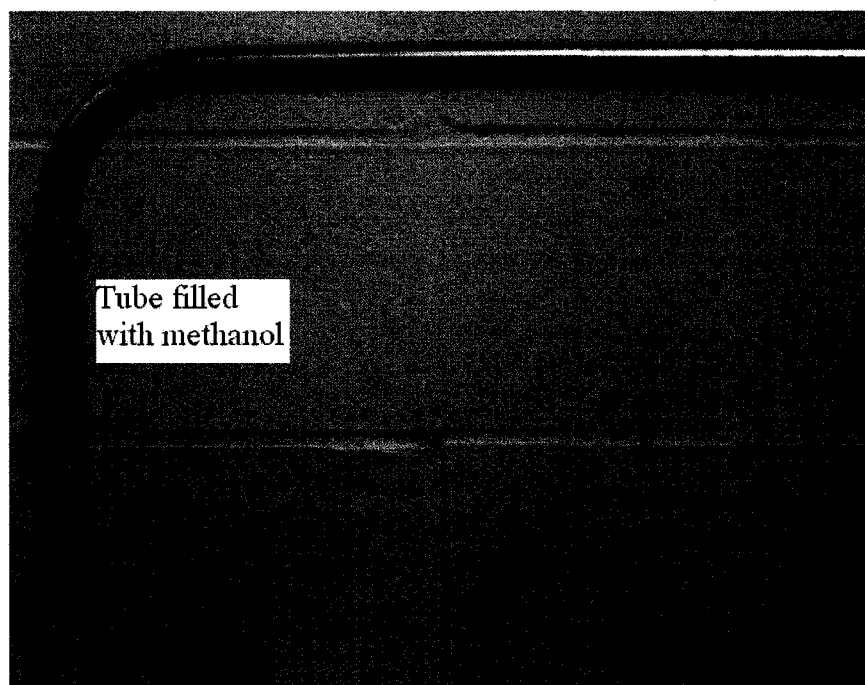


**Figure 3.5: Exit Section Methanol Wash**

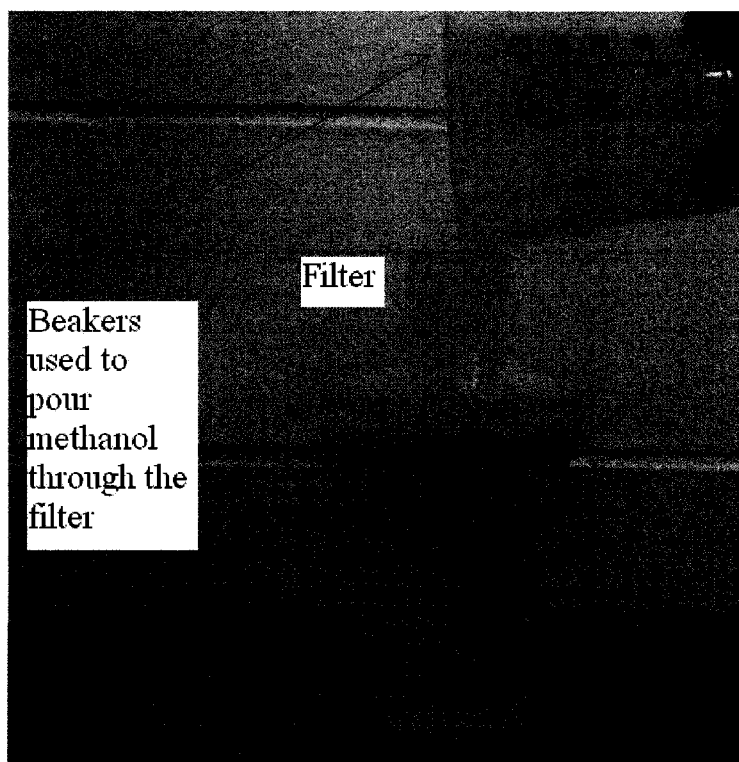


**Figure 3.6: Filter Methanol Wash**

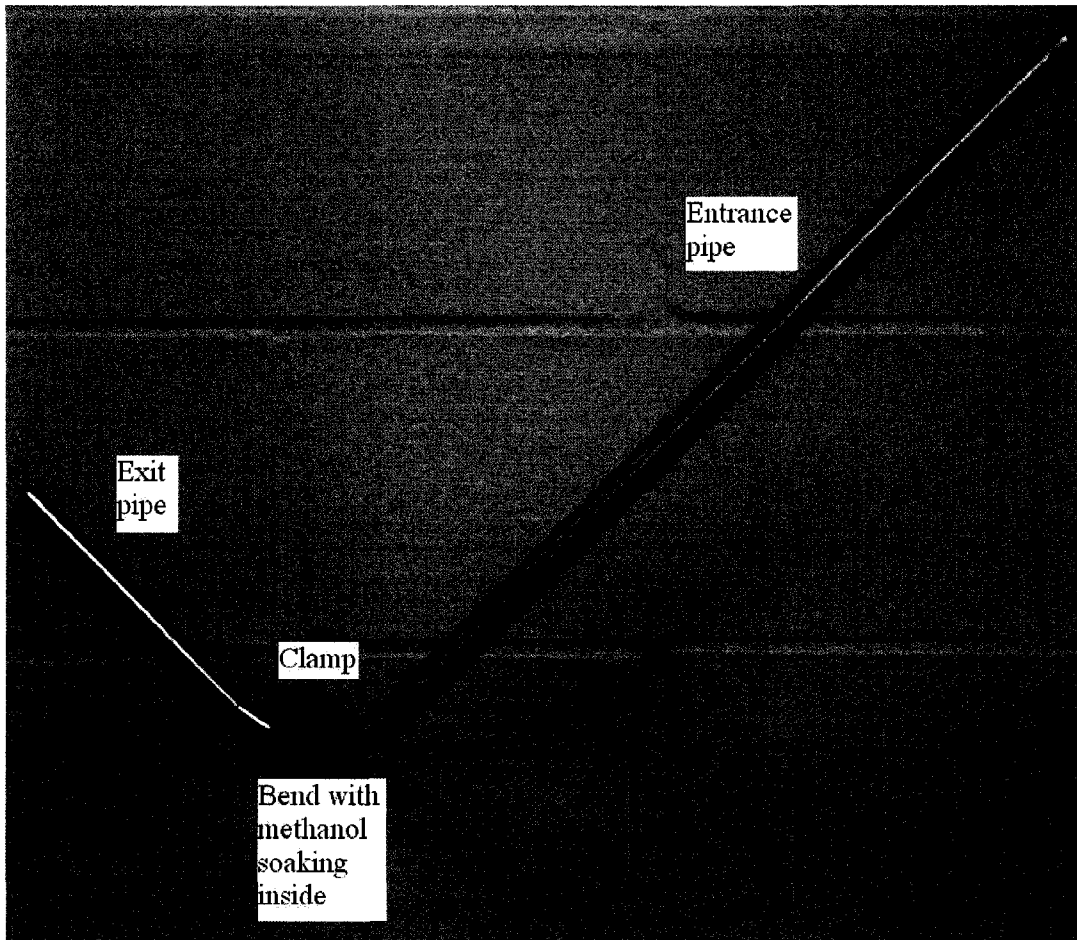


**Figure 3.7: Soaking of the 90° Test Section as Part of the Methanol Wash Procedure**

### **3.2.2 The Spectrophotometer**

An Agilent 8453 UV-visible Spectroscopy System, shown in Figure 3.8, was used to measure the concentrations of vitamin E in the methanol wash solution. The description of this instrument is based on the manual (Agilent Technologies, 2003). The absorbance of a sample is measured for different wavelengths in 1nm increments from 190 nm to 1100 nm. The absorbance ( $A_b$ ) is defined as:

$$A_b = \log_{10}(\text{Incident Light Intensity}/\text{Transmitted Light Intensity}) \quad (42)$$

If the absorbance is 1, 10% of the light photons pass through the sample. For vitamin E, the absorbance peak occurs at 285 nm and spans a wavelength range of 252-300 nm. The measured absorbance at 320 nm is subtracted from each absorbance to correct for impurities in the solution, since this wavelength should have zero absorbance due to vitamin E. If an impurity (such as acetone from the washing of the entrance section of the pipe) has an absorbance peak which overlaps the vitamin E peak, the absorbance peak will have a skewed shape. The measurement was discarded if this was the case. The absorbance value used is the wavelength-weighted average over 252-300 nm.

An absorbance much greater than 1 is inaccurate as explained via the following equations where  $Tr$  is the transmitted light intensity, and  $In$  is the incident light intensity (see chapter 4 for the uncertainty calculation procedure.):

$$\begin{aligned}
 Ab &= \log \left( e^{\ln \left( \frac{In}{Tr} \right)} \right) \\
 Ab &= \ln \left( \frac{In}{Tr} \right) \log e \\
 \frac{d(Ab)}{d(Tr)} &= \frac{\log e}{In/Tr} (-InTr^{-2}) = -\frac{\log e}{In} 10^{-Ab}
 \end{aligned}
 \tag{43}$$

Any uncertainty in the intensity of the transmitted light causes an uncertainty in the absorbance proportional to  $10^{Ab}$ , which grows very quickly when  $Ab$  is greater than 1. Therefore, if the measured absorbance at 285 nm was greater than 1.5, the measurement was not used. For a low absorbance, the precision error of the absorbance becomes a significant fraction of the absorbance, making the precision error in the deposition fraction large. Therefore, in general, the absorbance of the sample at 285 nm was at least 0.05. The absorption is directly proportional to concentration according to Beer's Law

(see for example Bauman & Poe 1962) and the software for the instrumentation was used to calculate mass of vitamin E in solution.

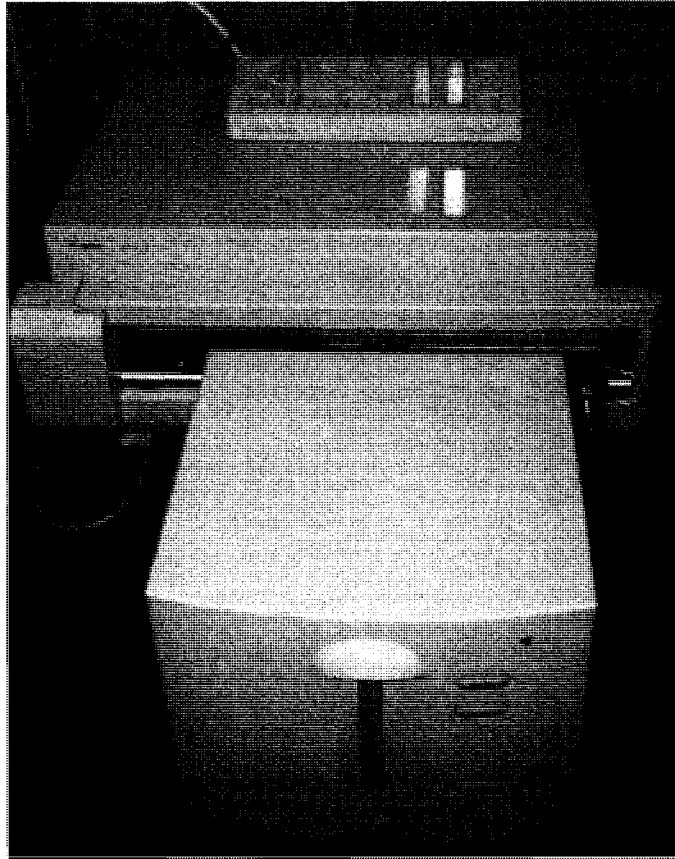


**Figure 3.8: The Spectrophotometer**

Overlaid Sample Spectra

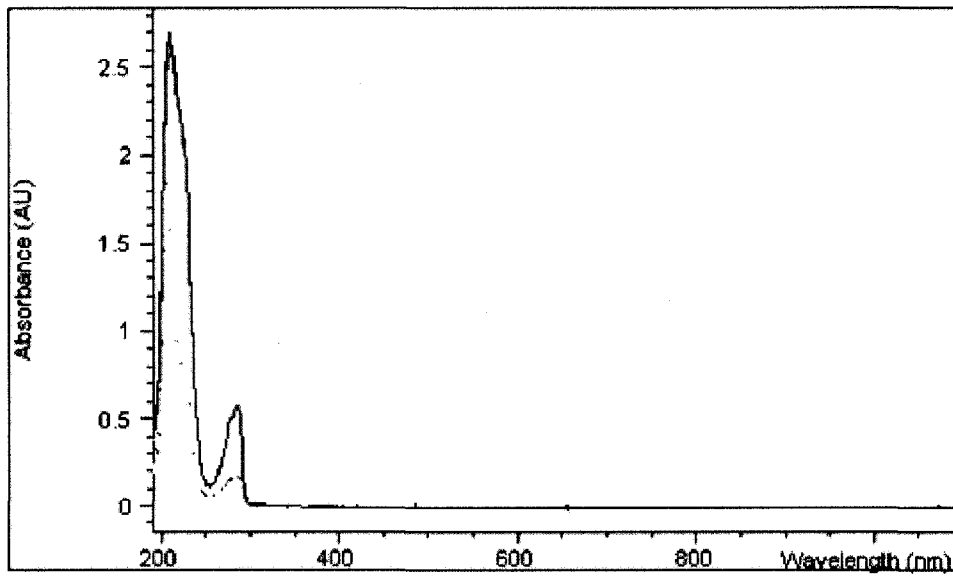


**Figure 3.9: Typical Absorbance Plot. The solid line is a group of bend measurements. The broken line is a group of filter measurements.**

## Chapter 4:      **Uncertainty Analysis**

It is necessary to know the uncertainty of the deposition fraction as well as of other important parameters which include the curvature ratio, the density ratio, the flow Reynolds number and the Stokes number. The method of uncertainty analysis used is based on the ANSI/ASME Measurement Uncertainty Standard (1985). The uncertainty of the data consists of two parts: the precision, and the propagated bias error. Bias error is the inability of the equipment to measure correct values. The propagated bias error is the estimate of the influence of all the different sources of bias error on the final measurement. The precision error is the scatter in the measurements caused by random error. Both kinds of error are estimated separately and then combined.

### **4.1 Bias Error**

Since the actual bias error for any particular instrument is unknown, it is estimated. This estimate is called the bias limit, and it represents the likely range in either the positive or negative direction that contains the true bias. When there are several different bias limits to be combined, it is assumed that there are as many negative bias errors as positive errors, so that they can be roughly combined in quadrature by the root sum of squares formula (Equation 44). When there are only a few bias limits to be combined, the same equation is used, but it is a less certain estimate, since they might actually combine additively. The calculation of bias propagation for a function  $f(x_1, x_2, \dots, x_N)$  is according to this formula:

$$U = \sqrt{U_1^2 + U_2^2 + \dots + U_N^2} \quad (44)$$

In turn,  $U, U_1, U_2, \dots, U_N$  are the propagated bias error, bias limit 1, bias limit 2, ..., bias limit N. To compute the bias limits, the following formula is used (The bias limit of one of the variables ( $x_1$ ) is  $U_{x1}$ ):

$$U_1 = \frac{\partial f(x_1, x_2, \dots, x_N)}{\partial x_1} U_{x1} \quad (45)$$

#### 4.1.1 Curvature Ratio

The bias limit of the curvature ratio is due to the bias limit in both the pipe radius ( $a$ ) and the bend radius ( $R$ ), which is:

$$\frac{U_\delta}{\delta} = \sqrt{\left(\frac{U_a}{a}\right)^2 + \left(\frac{U_R}{R}\right)^2} = \sqrt{\left(\frac{0.005}{0.405}\right)^2 + \left(\frac{0.1}{1.5}\right)^2} = 7\% \quad (46)$$

#### 4.1.2 Density Ratio

The bias limit of the density ratio is due to the bias limit in both the air density ( $\rho$ ) and the particle density ( $\rho_p$ ). The vitamin E used (Equate<sup>®</sup>) has a specific gravity of  $0.92 \pm 0.01$ . The air density is related to the pressure through the ideal gas law. Refer to section 3.1.7 for estimates of the air pressure in the test section. For the Re 10 000 case the gauge pressure is 0.0 kPa. For the Re 20 000 case the gauge pressure is -0.5 kPa, so the bias limit (including the 2 kPa bias limit of the gauge) of air density is

$$\frac{U_\rho}{\rho} \approx \frac{U_P}{P} = \sqrt{\left(\frac{2 - 0.5}{101.325 - 0.5}\right)^2} = 2.5\%$$

For the Re = 30 100 case, the bias limit is

$$\frac{U_{\rho}}{\rho} \approx \frac{U_P}{P} = \sqrt{\left(\frac{1.5}{101.325 - 0.7}\right)^2} = 2\% \quad (47)$$

For simplicity, a bias limit for the air density of 2.5% was used for all cases.

$$\frac{U_{\lambda}}{\lambda} = \sqrt{\left(\frac{U_{\rho}}{\rho}\right)^2 + \left(\frac{U_{\rho_p}}{\rho_p}\right)^2} = \sqrt{(2.5\%)^2 + \left(\frac{1\%}{0.92}\right)^2} = 2.5\% \quad (48)$$

A variation of the air temperature could also cause a variation of the air density. Since the variation in laboratory air temperature was small among all the experiments ( $24^{\circ}\text{C} \pm 3^{\circ}\text{C}$ ), it is assumed that any variation in density due to temperature changes are absorbed in the precision uncertainty. Since air humidity was not monitored, any variations were also assumed to be reflected in the precision uncertainty.

### 4.1.3 Flow Reynolds Number

The flow Reynolds number is:

$$\text{Re} = \frac{2Q}{\pi a v} = \frac{2\dot{m}}{\pi a \mu} \quad (49)$$

The mass flow rate can be written in terms of the Standard Litres Per Minute (SLPM) flow rate  $Q_{SLPM}$ , which is the equivalent mass flow rate for air at atmospheric density.

$$Q_{SLPM} \rho_{atmosphere} = Q\rho = \dot{m} \quad (50)$$

$$\text{Re} = \frac{2Q_{SLPM} \rho_{atmosphere}}{\pi a \mu} \quad (51)$$

$$\frac{U_{\text{Re}}}{\text{Re}} = \sqrt{\left(\frac{U_{Q_{SLPM}}}{Q_{SLPM}}\right)^2 + \left(\frac{U_a}{a}\right)^2} \quad (52)$$

From the mass flow rate specifications (section 3.9):

$$\begin{aligned}
\frac{U_{Q_{SLPM}}}{Q_{SLPM}} &= \sqrt{\left(\frac{0.3SLPM}{Q_{SLPM}}\right)^2 + 0.007^2 + 0.002^2} \\
Q_{SLPM} &= \frac{Re \pi a v}{2} \\
\frac{U_{Q_{SLPM}}}{Q_{SLPM}} &= \sqrt{\left(\frac{0.3SLPM}{\frac{Re \pi a v}{2}}\right)^2 + 0.007^2 + 0.002^2} \\
&= \sqrt{\left(\frac{40}{Re}\right)^2 + 0.007^2 + 0.002^2} \leq \sqrt{\left(\frac{40}{10000}\right)^2 + 0.007^2 + 0.002^2} = 0.8\%
\end{aligned} \tag{53}$$

For the  $Re = 30\ 100$  case, the error for the two flow meters was combined by the root sum of squares method (giving 2.2%). The bias for the Reynolds number (for  $Re = 10\ 000$  and  $Re = 20\ 000$ ) is:

$$\frac{U_{Re}}{Re} = \sqrt{(0.8\%) + \left(\frac{0.5\%}{0.405}\right)^2} < 2\% \tag{54}$$

and for  $Re=30\ 100$  it is 2.5%.

#### 4.1.4 Stokes Number

The Stokes number is:

$$\begin{aligned}
St &= \frac{\rho_p d_p^2 Q}{18\pi\mu a^3} \\
Q &= \frac{Q_{SLPM} \rho_{atmosphere}}{\rho} \\
d_a &= \sqrt{SG} d_p \\
St &= \frac{d_a^2 Q_{SLPM} \rho_{atmosphere}}{18\mu a^3 \rho}
\end{aligned} \tag{55}$$

The aerodynamic diameter is  $d_a$ , and the specific gravity is  $SG$ . The bias limit in the Stokes number is then:

$$\frac{U_{St}}{St} = \sqrt{\left(\frac{2U_{d_a}}{d_a}\right)^2 + \left(\frac{U_{Q_{SLPM}}}{Q_{SLPM}}\right)^2 + \left(\frac{3U_a}{a}\right)^2 + \left(\frac{U_\rho}{\rho}\right)^2} \tag{56}$$

The bias in the Stokes number becomes (including the bias limit of the Particle Size Distribution Analyzer, section 3.5):

$$\frac{U_{St}}{St} = \sqrt{(2 \times 2\%)^2 + (2\%)^2 + \left(\frac{3 \times 0.5\%}{0.405}\right)^2 + (2.5\%)^2} = 6\% \quad (57)$$

Since the particle size was also calculated based on the operation of the aerosol generator (section 3.2) there is another way to calculate the Stokes number bias limit, using the calculated particle size and the bias in the calculated particle size:

$$\frac{u_d}{d} = \frac{1}{3} \sqrt{\left(\frac{u_{Q_s}}{Q_s}\right)^2 + \left(\frac{u_f}{f}\right)^2 + \left(\frac{u_{C+I}}{C+I}\right)^2} \quad (58)$$

For the aerodynamic diameter, the bias limit of the density of the vitamin E must be included:

$$\begin{aligned} \frac{u_{d_a}}{d_a} &= \sqrt{\left(\frac{1}{3} \frac{u_{Q_s}}{Q_s}\right)^2 + \left(\frac{1}{3} \frac{u_f}{f}\right)^2 + \left(\frac{1}{3} \frac{u_{C+I}}{C+I}\right)^2 + \left(\frac{0.01}{0.92}\right)^2} \\ &\approx \sqrt{\left(\frac{1}{3} \frac{u_{Q_s}}{Q_s}\right)^2 + \left(\frac{1}{3} \frac{u_f}{f}\right)^2 + \left(\frac{1}{3} \frac{u_C}{C}\right)^2 + \left(\frac{0.01}{0.92}\right)^2} \end{aligned} \quad (59)$$

The vitamin E solution was diluted for measuring the concentration in the spectrophotometer (about a 2% bias limit in the concentration) and then the known concentration was diluted for putting in the syringe which attached to the generator (about a 2% bias limit in the concentration). This gives a total bias limit for the calculated aerodynamic diameter of (using the bias values from section 3.2):

$$\begin{aligned} \frac{u_{d_a}}{d_a} &\approx \sqrt{\left(\frac{1}{3} \frac{u_{Q_s}}{Q_s}\right)^2 + \left(\frac{1}{3} \frac{u_f}{f}\right)^2 + \left(\frac{1}{3} \frac{u_C}{C}\right)^2 + \left(\frac{0.01}{0.92}\right)^2 + \left(\frac{1}{3} \frac{2}{100}\right)^2 + \left(\frac{1}{3} \frac{2}{100}\right)^2} \\ &= \sqrt{\left(\frac{1}{3} 1\%\right)^2 + \left(\frac{1}{3} 1\%\right)^2 + \left(\frac{1}{3} 2\%\right)^2 + \left(\frac{1\%}{0.92}\right)^2 + \left(\frac{1}{3} 2\%\right)^2 + \left(\frac{1}{3} 2\%\right)^2} = 2\% \end{aligned} \quad (60)$$

This is the same bias limit as for the measured size, so the bias in the Stokes number is the same; however, a comparison of the calculated and measured diameters indicated that either one had more bias than anticipated, since they are usually different by more than 4%. The interpretation is that there was a lot of variability in the dilution process, and possibly a higher uncertainty in the calibration constant of concentration versus absorbance than estimated. Another possibility is that the Particle Size Distribution analyzer became out of calibration. Because of this, the data was examined twice, once for each particle size estimate. The results for each size estimate show the same trends, so only the measured sizes are used for the presentation of the final data, but it should be assumed that there is some uncertainty in the Stokes number not captured by this uncertainty analysis.

#### 4.1.5 Deposition Fraction

The deposition fraction, DF, is given by:

$$DF = \frac{Vol_{bend} Ab_{bend}}{Vol_{bend} Ab_{bend} + Vol_{filter} Ab_{filter}} = \frac{N_{bend}}{N_{bend} + N_{filter}} \quad (61)$$

The  $Ab$ 's are absorbance fractions, and the  $Vol$ 's are the volumes of the solvent used to wash out the vitamin E from the filter or the bend. The bias limit is:

$$U_{DF} = \sqrt{\left(U_{N_{bend}} \frac{\partial DF}{\partial N_{bend}}\right)^2 + \left(U_{N_{filter}} \frac{\partial DF}{\partial N_{filter}}\right)^2} \quad (62)$$

$$\frac{\partial DF}{\partial N_{bend}} = \frac{N_{filter}}{(N_{bend} + N_{filter})^2} = \frac{\frac{N_{filter}}{N_{bend}} N_{bend}}{(N_{bend} + N_{filter})^2} = DF(1 - DF) \frac{1}{N_{bend}} \quad (63)$$

$$\frac{\partial DF}{\partial N_{filter}} = \frac{-N_{bend}}{(N_{bend} + N_{filter})^2} = DF \frac{-\frac{N_{filter}}{N_{bend} + N_{filter}}}{N_{bend} + N_{filter}} = DF(1 - DF) \frac{-1}{N_{filter}} \quad (64)$$

$$\frac{U_{DF}}{DF} = (1 - DF) \sqrt{\left(\frac{U_{Nb}}{Nb}\right)^2 + \left(\frac{U_{Nf}}{Nf}\right)^2} \quad (65)$$

$$\frac{U_{DF}}{DF} = (1 - DF) \sqrt{\left(\frac{U_{Vol_{bend}}}{Vol_{bend}}\right)^2 + \left(\frac{U_{Ab_{bend}}}{Ab_{bend}}\right)^2 + \left(\frac{U_{Vol_{filter}}}{Vol_{filter}}\right)^2 + \left(\frac{U_{Ab_{filter}}}{Ab_{filter}}\right)^2} \quad (66)$$

The following estimates have been made:

$$\frac{U_{Vol_{bend}}}{Vol_{bend}} = 1.4\% \quad (67)$$

$$\frac{U_{Vol_{filter}}}{Vol_{filter}} = 4.3\% \quad (68)$$

$$\frac{U_{Ab_{bend}}}{Ab_{bend}} = \frac{U_{Ab_{filter}}}{Ab_{filter}} = 2\% \quad (69)$$

The bias limit of the deposition fraction is given by:

$$\frac{U_{DF}}{DF} = (1 - DF) \sqrt{(1.4\%)^2 + (2\%)^2 + (4.3\%)^2 + (2\%)^2} = 5.3\%(1 - DF) \quad (70)$$

The bias limits for the key parameters in the experiment are summarized in Table 4.1 below.

**Table 4.1 Bias Limits**

Parameter	Bias limit
$\delta$	7%
$\lambda$	2.5%
Re	2% or 2.5% (Re = 30 100)
St	6%
DF	5.3%(1 - DF)

## 4.2 Precision

The precision error causes scatter in the deposition fraction results of different experiments for the same data point. This is quantified by using the Student t-test with a 95% confidence interval for the sample mean. When different experiments at the same data point have different Reynolds numbers or Stokes numbers, the average Reynolds number and average Stokes number are used. The error caused by this is accounted for in the precision error. The precision error is calculated by multiplying the standard deviation of the sample average deposition fraction for the data point by the appropriate t-value (from Student's t-distribution tables). For example, using the point  $Re = 10\ 000$ ,  $St = 0.44$ , there were 4 experiments, with an average  $DF$  of 0.67 with a standard deviation of 0.0024. This gives a standard deviation of the mean of  $0.0024/\sqrt{4} = 0.0012$ . The t-value for 3 degrees of freedom and a 95% confidence interval is 3.182. The uncertainty is then  $3.182 \times 0.0012 = 0.004$ . This can be seen in Table 5.1.

## 4.3 Total Uncertainty

The total uncertainty for the density ratio, the curvature ratio, the Reynolds number and the Stokes number is just the bias error. The total uncertainty of the deposition fraction is the root sum of squares of the precision error and the bias error. Total uncertainty values are given along with experimental data in the following chapter. Referring to the point  $Re = 10\ 000$ ,  $St = 0.44$  (Table 5.1), the bias is 0.012 and the precision is 0.004. This gives an uncertainty of  $\sqrt{0.004^2 + 0.012^2} = 0.013$ .

## Chapter 5: Experimental Results

Deposition measurements of spherical aerosols in the 90° bend were made for flow Reynolds numbers of 10 000, 20 000 and 30 100. The Stokes number based on the particle diameter was varied between 0.1 and 1.0. The experimental results are summarized in Table 5.1. The total uncertainties were estimated according to the procedure outlined in Chapter 4 and were 1 to 20% of the measured deposition fraction (an average of 7%).

**Table 5.1: Experimental Results (Curvature ratio is  $7.4 \pm 0.5$ . Density ratio is  $770 \pm 20$ )**

Re	St $\pm 6\%$	Deposition Fraction (DF)	Bias Limit	Precision	Uncertainty
10 000 $\pm 200$	0.11	0.05	0.003	0.011	0.011
	0.17	0.19	0.008	0.034	0.035
	0.26	0.44	0.013	0.049	0.051
	0.44	0.67	0.012	0.004	0.013
	0.53	0.74	0.010	0.007	0.013
	0.89	0.90	0.005	0.015	0.015
20 000 $\pm 400$	0.97	0.92	0.004	0.012	0.012
	0.13	0.28	0.011	0.026	0.028
	0.21	0.45	0.013	0.011	0.017
	0.47	0.69	0.011	0.023	0.025
	0.60	0.77	0.009	0.012	0.015
	0.78	0.85	0.007	0.007	0.010
30100 $\pm 800$	1.06	0.91	0.004	0.022	0.023
	0.13	0.32	0.012	0.049	0.050
	0.21	0.42	0.013	0.029	0.032
	0.48	0.68	0.012	0.051	0.053

As a validation of our results, the Reynolds 10 000 case is plotted against the experimental results of Pui et al. (1987) in Figure 5.1. The trends of the two sets of data are very similar. For an increase of Stokes number there is an increase of deposition fraction. At a Stokes number of 0.8 the deposition fraction is about 80%, and as the Stokes number is increased further, the rate of increase of the deposition fraction flattens out. Even though the curvature ratios are different by 30% (7.4 in the present study versus 5.7 for Pui et al.), the results are almost identical. The experimental and numerical results of McFarland et al. (1997) show that the deposition fraction is expected to change by less than + 0.05 going from a curvature ratio of 4 to 10, so this similarity of our results with those of Pui et al. is expected.

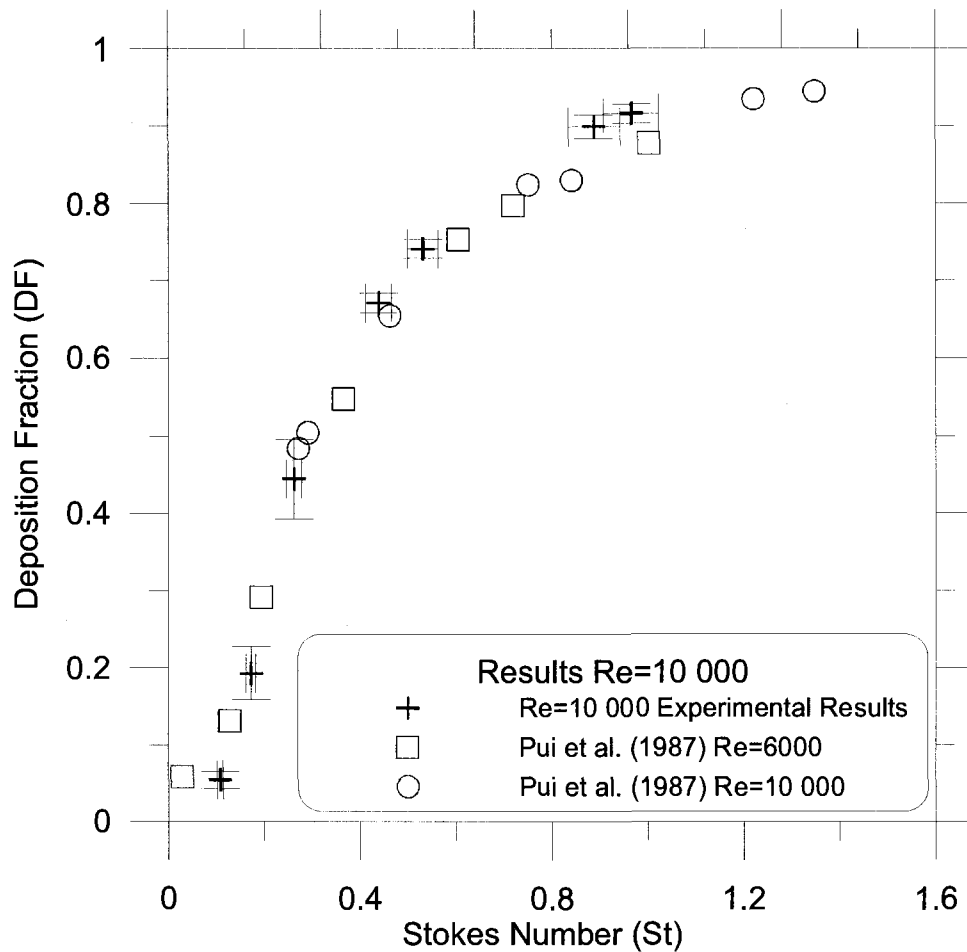


**Figure 5.1: Re = 10 000 Results Compared with Experimental Results of Pui et al.**

(1987).  $\left( St = \frac{\rho_p d_p^2 Q}{18\pi\mu a^3} \right)$

All three Reynolds number cases are plotted together in Figure 5.2. Where the error bars for the same data point do not overlap between the different Reynolds number cases, significant differences are said to be detected. This occurs at a Stokes number of 0.15. The Reynolds number cases 20 000 and 30 100 exhibit significantly more deposition than the 10 000 case at this Stokes number.

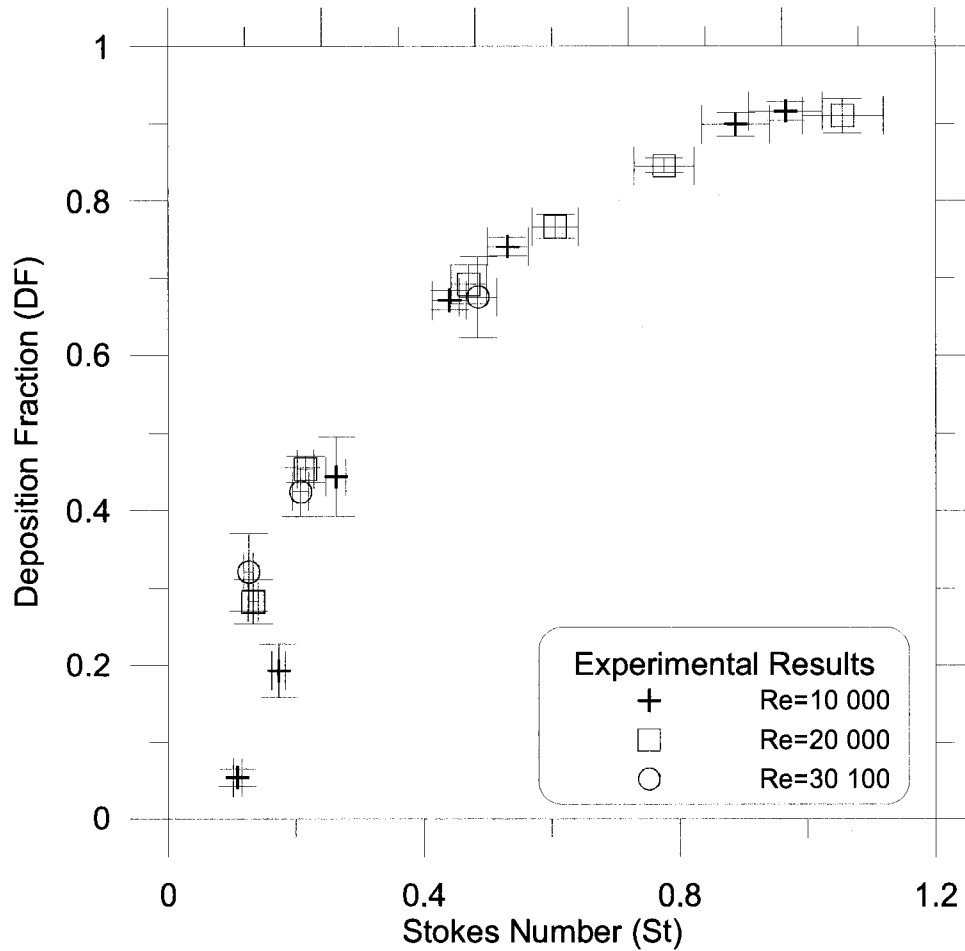


**Figure 5.2: Experimental Results**  $\left( St = \frac{\rho_p d_p^2 Q}{18\pi\mu a^3} \right)$

Since the Reynolds number effect is seen in the lower Stokes number range, it is possible that it is due to turbulent dispersion. As discussed in section 2.6, the smaller Stokes number particles tend to be more responsive to the diffusive effect of turbulence; however, due to the complex effect of turbulence on particle trajectories (discussed in section 2.6) this needs to be examined more closely. For this reason, numerical simulations were added, which are discussed in the next chapter.

## **Chapter 6: Simulations**

A numerical study was undertaken to investigate if the Reynolds number effect on the deposition fraction (different Reynolds numbers giving different deposition fractions at the same Stokes number) seen in the experimental data could be detected numerically, and if so, if it could be explained. In the experimental data, for Stokes numbers near 0.15, there is an increase in the deposition fraction (DF) of about 0.1 when the Reynolds number is increased from 10 000 to 20 000. Particle deposition in the bend for a Stokes number ranging from 0.1 to 0.9 was studied numerically for the three different Reynolds numbers ( $Re = 10\,000$ ,  $20\,000$ , and  $30\,000$ ) using RANS (Reynolds Averaged Navier-Stokes) equations and RANS/EIMs (RANS/Eddy Interaction Models).

### **6.1 Background**

The volume fraction of particles in the air for the experiment is approximately 0.0004%, which is small enough to indicate that the influence of the particles on the flow is negligible (Elghobashi, 1994) so that the “one-way coupling” approach can be used. In other words, particles do not affect the single-phase fluid motion. For all of the numerical simulations, the volumetric concentration was kept smaller than 0.0004%. This allowed the flow-field to be solved in the absence of the particles. The particles were then introduced and tracked using the Lagrangian equation of motion.

## 6.2 Fluid Velocity Field Calculation

The Reynolds Averaged Navier-Stokes equations (RANS) were solved with the CFX-11.0 software (ANSYS Inc.). To solve for the turbulent stresses in the RANS equations, the Shear Stress Transport (SST) turbulence model, which was developed by Menter (1994), was used. The SST model combines the existing k- $\epsilon$  and k- $\omega$  models (see for example Hoffmann and Chiang, 2000). It has been found that the k- $\omega$  model is too sensitive to the specification of inlet boundary conditions for  $\omega$  (the turbulent eddy frequency), and the k- $\epsilon$  model does not have this problem (Menter, 1994). Thus the k- $\epsilon$  is generally preferable, but the k- $\omega$  is better in the sublayer of the boundary-layer (Menter, 1994). Menter writes the k- $\epsilon$  equations in terms of  $\omega$ . The result is (Hoffmann and Chiang, 2000):

$$\begin{aligned} \frac{\partial k}{\partial t} + U_i \frac{\partial k}{\partial x_i} &= \tau_{ij} \frac{\partial u_i}{\partial x_j} - \beta k \omega + \frac{\partial}{\partial x_i} \left[ (v + \sigma v_e) \frac{\partial k}{\partial x_i} \right] \\ \frac{\partial \omega}{\partial t} + U_i \frac{\partial \omega}{\partial x_i} &= \alpha \frac{\omega}{k} \tau_{ij} \frac{\partial u_i}{\partial x_j} - \beta' \omega^2 + \frac{\partial}{\partial x_i} \left[ (v + \sigma' v_e) \frac{\partial \omega}{\partial x_i} \right] + 2(1-F) \frac{\sigma'}{\omega} \frac{\partial k}{\partial x_i} \frac{\partial \omega}{\partial x_i} \end{aligned}$$

$$F = \tanh(\arg^2)$$

$$\arg = \max \left[ 2 \frac{\sqrt{k}}{0.09 \omega y}, \frac{500\nu}{\omega y^2} \right] \quad (71)$$

The distance to the closest wall is  $y$ . The constants for the k- $\omega$  model are:

$$\beta = 0.09, \alpha = 5/9, \beta' = 3/40, \sigma = 0.5, \sigma' = 0.5 \quad (72)$$

Constants for the k- $\epsilon$  model are:

$$\beta = 0.09, \alpha = 0.44, \beta' = 0.0828, \sigma = 1, \sigma' = 0.856 \quad (73)$$

These models are now combined by blending them. Let  $\Phi$  represent one of the above constants, and a subscript of 1 refer to the k- $\omega$  model and 2 refer to the k- $\epsilon$  model. The actual constant is determined by (Hoffmann and Chiang, 2000):

$$\Phi = F\Phi_1 + (1 - F)\Phi_2 \quad (74)$$

Menter makes a further change by limiting the eddy viscosity by a new formula for the eddy viscosity (Hoffmann and Chiang, 2000):

$$\nu_e = \frac{0.31k}{\max(0.31\omega, \Omega F)} \quad (75)$$

The term  $\Omega$  is the absolute value of vorticity. The constants in the SST model were fine-tuned by comparing the model predictions with experimental results of test flows, including: free shear flows, an adverse pressure gradient flow along the axis of a cylinder, a backward facing step flow, a NACA 4412 airfoil flow, and a transonic bump flow (Menter, 1994). The software uses a blend of formulae close to a wall. The log law of the wall formula to relate the stresses (turbulent and non-turbulent stresses) to the velocity is blended with the SST calculation. As the grid is refined, the SST calculation portion of the blend becomes more dominant. This is called the automatic wall treatment option. The option used for the discretization of the convection term is high resolution, which is a blend of upwind differencing and central differencing. The upwind differencing more appropriately models convection, but the blending of central differencing increases stability. The convergence criterion was either 1000 iterations or normalized rms residuals less than  $10^{-10}$ . For all simulations the rms residuals were lower than  $10^{-5}$ . The residual is the difference between the left hand side and the right hand side of the equation being solved.

The entrance length of pipe required for fully developed turbulent flow is  $4.4\text{Re}^{1/6}$  (White, 1998), which equals 24.5 diameters for  $\text{Re}=30\,000$ , and 10 inches (25.4 cm) for the

pipe diameter of 0.405 inches (10.3 cm). For the simulations, an entrance length of 10 inches (25.4 cm) and an exit length of 4 inches (11.6 cm) were used. The boundary conditions were: an area-average zero gauge pressure at the pipe outlet, a given flow rate of 25°C dry air, and a uniform velocity profile at the inlet, with an entrance turbulence intensity of 5%. The particles were introduced uniformly across the inlet to the entrance pipe before the bend, and were allowed to deposit in the entrance pipe before the bend. The number of particles deposited in the entrance pipe was subtracted from the number entering the inlet, so that the number entering the bend was known.

### **6.3 Mesh**

A multi-block structured grid with 15 blocks was used, which had biased accumulation of nodes towards the wall. Figure 6.1 shows the bend geometry (identical to the geometry used in the experiments shown in Chapter 3) and the computational grid (at the mid plane and at the entrance of the bend). The grid was generated using the ICEM-CFD software (ANSYS Inc.). A grid convergence study was performed for the flow-field for the  $Re = 30\,000$  case and results were evaluated using both the pressure drop through the test section, including the entrance pipe and exit pipe (Figure 6.2), and the velocity profile at both the start and the end of the bend (Figure 6.3). It was determined that changes in the computed flow-field were insignificant when the number of grid nodes was increased from 600 000 to 1 800 000. The medium sized grid was considered to be adequate and the particle tracking simulations were performed with 1 100 000 nodes.

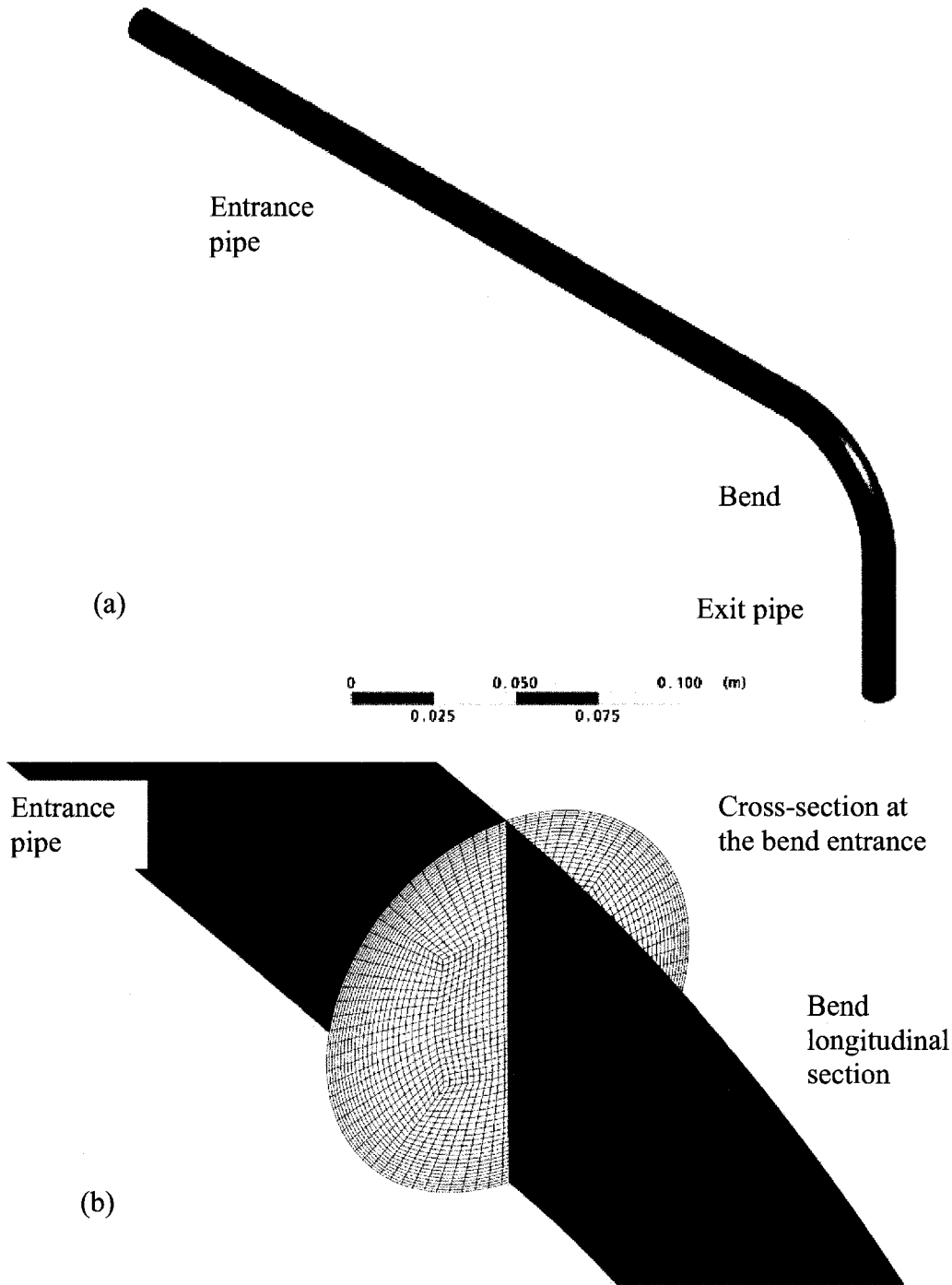


**Figure 6.1: Overall Computational Geometry (a) and Representation of the Computational Grid (b) (at the midplane of the geometry and at a cross section at the entrance of the bend).**

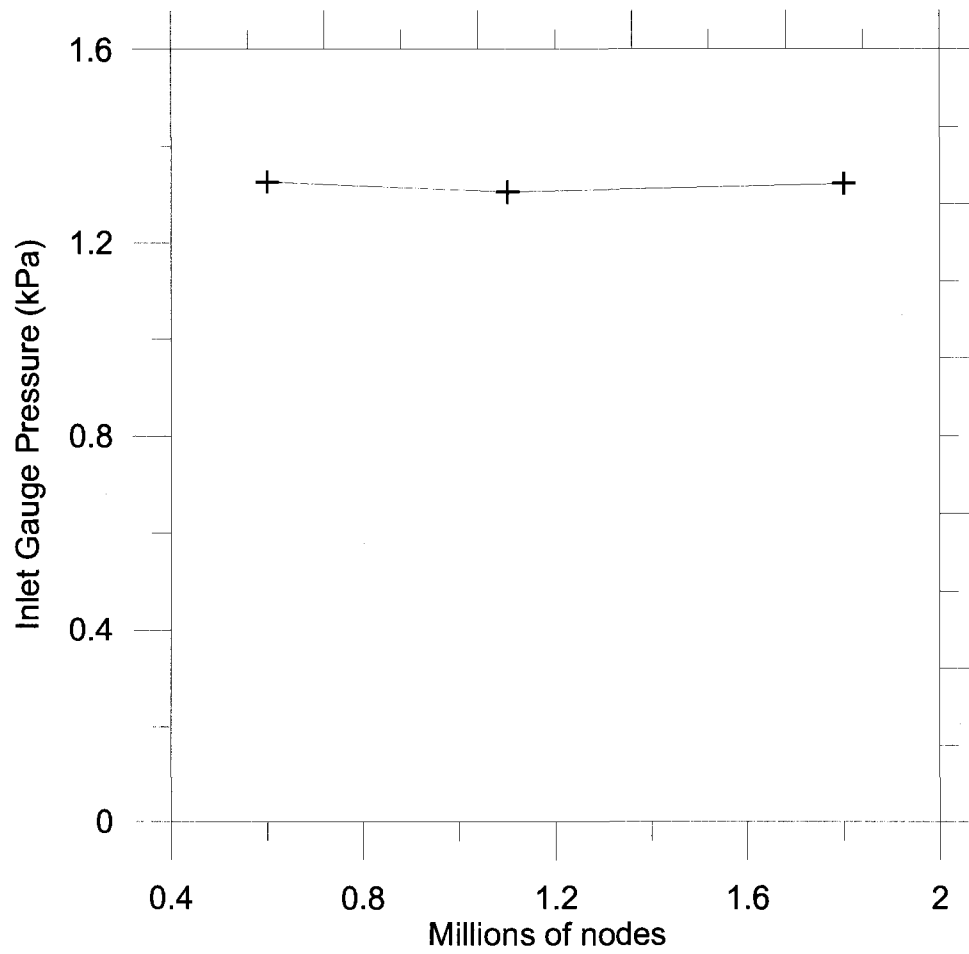


**Figure 6.2 Grid Convergence Study of the Test Section Inlet Pressure (area average)**

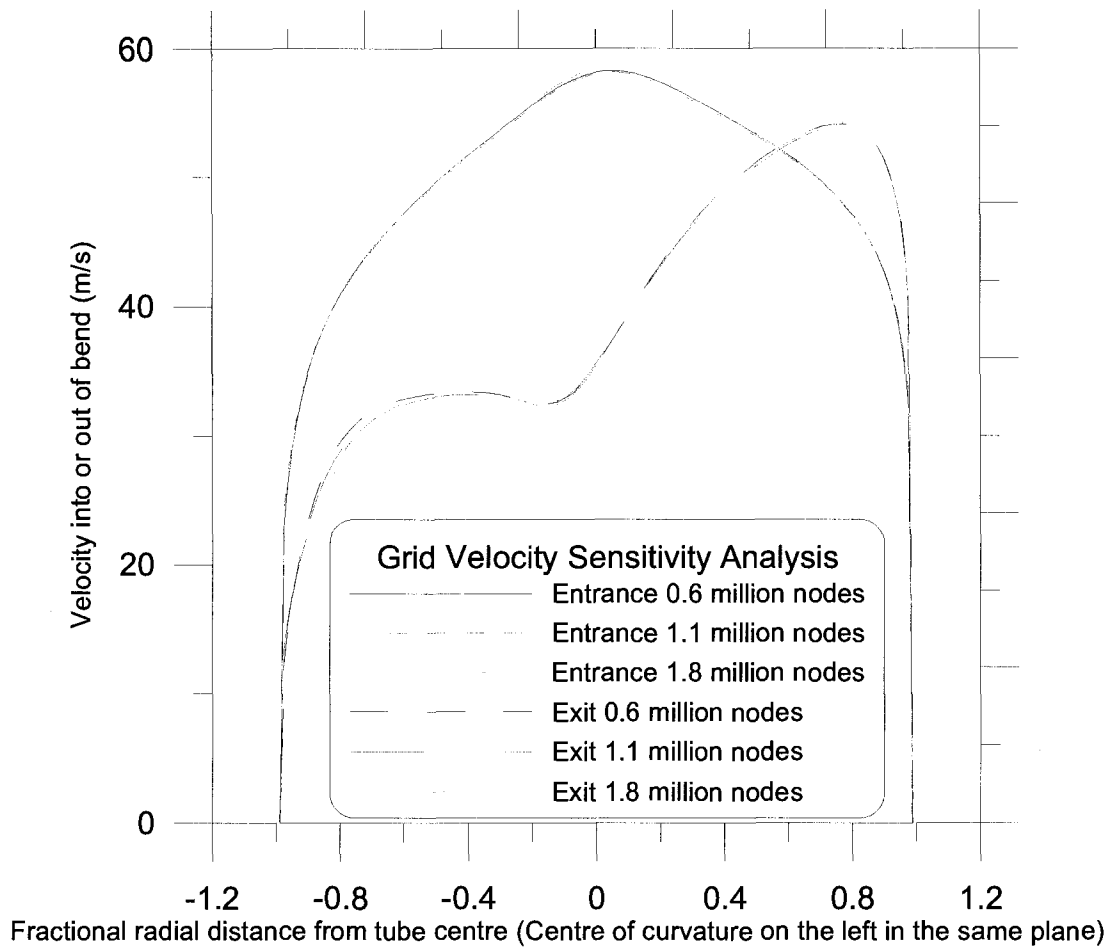


**Figure 6.3 Grid Convergence Study of the Velocity into and out of the Bend**

Since the secondary flow pattern might have a significant effect on the deposition fraction result, a graph was also made of the velocity component pointing away from the center of curvature of the bend at the bend exit, shown in Figure 6.4.

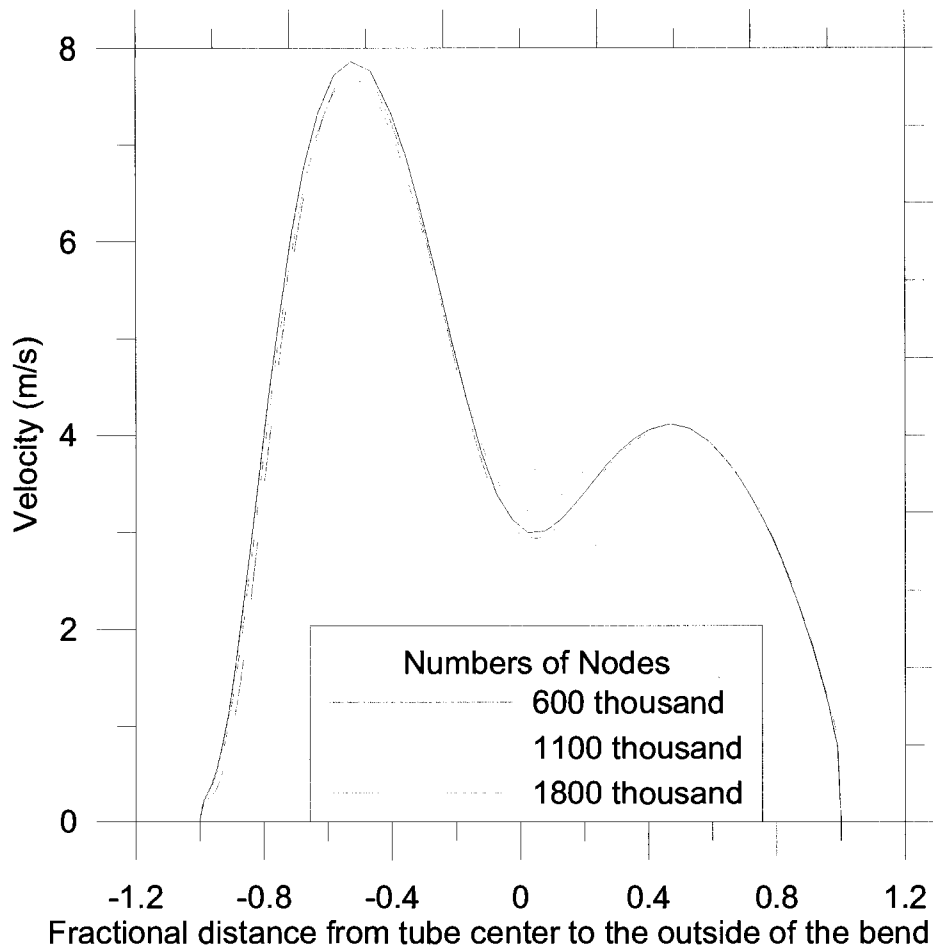


**Figure 6.4 Grid Convergence Study of the Secondary Flow Velocity Component in the Direction Away from the Bend Center of Curvature at the Exit to the Bend Portion**

The result seen in Figure 6.4 is that the secondary flow pattern is not significantly changed by increasing the node number from 600 000 to 1 800 000.

#### **6.4 Particle Trajectory Calculation**

Each particle trajectory is calculated by twice integrating the Lagrangian equation of motion for a spherical particle. Based on Equation 28 (the non-dimensional equation), the particle equation implemented in CFX11.0 (ANSYS Inc.) is

$$\begin{aligned}
St \frac{d\vec{V}_p^{(n)}}{dt^{(n)}} &= -\frac{C_D \text{Re}_p}{24} (\vec{V}_p^{(n)} - \vec{V}^{(n)}) \\
St &= \frac{\rho_p d_p^2 Q}{18\pi\mu a^3} = \frac{\rho_p d_p^2 V}{18\mu a} = \frac{m_p V}{3\pi\mu d_p a} \\
St \frac{d\vec{V}_p^{(n)}}{dt^{(n)}} &= \frac{m_p V}{3\pi\mu d_p a} \frac{a d\vec{V}_p}{V^2 dt} = \frac{m_p}{3\pi\mu d_p V} \frac{d\vec{V}_p}{dt} = \frac{C_D \text{Re}_p}{24V} (\vec{V} - \vec{V}_p) \\
m_p \frac{d\vec{V}_p}{dt} &= \frac{C_D \text{Re}_p \pi\mu d_p}{8} (\vec{V} - \vec{V}_p) = \frac{C_D \left| \frac{(\vec{V} - \vec{V}_p) d_p}{v} \right| \pi\mu d_p}{8} (\vec{V} - \vec{V}_p) \\
m_p \frac{d\vec{V}_p}{dt} &= \frac{C_D |\vec{V} - \vec{V}_p| \pi\rho d_p^2}{8} (\vec{V} - \vec{V}_p) = \frac{C_D |\vec{V} - \vec{V}_p| \rho A_p}{2} (\vec{V} - \vec{V}_p) \\
m_p \frac{d\vec{V}_p}{dt} &= \frac{1}{2} C_D \rho A_p |\vec{V} - \vec{V}_p| (\vec{V} - \vec{V}_p), \tag{76}
\end{aligned}$$

where  $\rho$  is the fluid density,  $A_p$  is the particle cross-sectional area, and the instantaneous fluid velocity at the particle location is given by

$$\vec{V} = \vec{V}_m + \vec{V}', \tag{77}$$

which is the sum of the mean velocity given by the RANS results, and a turbulent fluctuation, which is modeled. The coefficient of drag is given by the Schiller-Naumann correlation (Schiller & Naumann 1935):

$$C_D = \frac{24}{\text{Re}_p} (1 + 0.15 \text{Re}_p^{0.687}) \tag{78}$$

For the instantaneous fluid velocity,  $\vec{V}$ , in the particle equation of motion, there are two options available in the CFX11.0 software. Option 1 is to use the mean flow calculated by the RANS solution. This omits the fluctuations in the fluid velocity resulting from turbulence, and so neglects the turbulent dispersion mechanism by making the fluctuation component equal to zero so that

$$\vec{V} = \vec{V}_m. \quad (79)$$

Option 2 uses turbulent dispersion, where  $\vec{V}'$  is generated through modeling using, for example, the eddy interaction model (Gosman, & Ioannides, 1981). Both approaches are tested in the current work. Deposition resulting from the mean flow tracking (option 1) is referred to as inertial impaction. The effect of turbulent dispersion in addition to inertial impaction is captured with the turbulent dispersion option (option 2). With the eddy interaction model, for each velocity component a turbulent fluctuation component is added to the mean (from the RANS results), by sampling from a Gaussian probability density function of zero mean and a standard deviation equal to the eddy velocity scale

$$u_e = \sqrt{\frac{2k}{3}}, \quad (80)$$

This is the rms speed for isotropic turbulence. This fluctuation component is associated with a turbulent eddy, of a length scale

$$L_e = 0.164 \frac{k^{\frac{3}{2}}}{\varepsilon}, \quad (81)$$

and is imposed for a certain interaction time after which a new fluctuation component is generated (see section 2.6 for a discussion of eddy length and velocity scales). The interaction time is the minimum of the eddy time scale ( $L_e / u_e$ ), or the time for the particle to traverse the eddy (given by the solution of the particle equation of motion).

The particle density was fixed at a specific gravity of 0.912 (density ratio of 760, which is different from the 770 used in the experiments). For a particular Stokes number (or at a fixed Re, for a given particle diameter) at least 10 000 particles were allowed to enter the bend. Since some particles deposited in the entrance pipe, more than 10 000 needed to be

released into the start of the entrance pipe (with uniform spatial distribution) to ensure sufficient particles entered the bend. These were tracked by the software using the particle equation of motion, with and without turbulent dispersion, from which the deposition fraction was calculated. Particles impacting the walls were assumed to stick.

A sensitivity analysis of the number of particles used was performed to validate the use of 10 000 particles. This is seen in Figure 6.5, for which the Stokes numbers 0.07 and 0.97 are used. The deposition fraction is plotted against the Stokes number for a release of 5000 particles at the entrance and a release of 10 000. To verify grid convergence for the particle calculation, this was repeated for the 1.8 million node case. The Reynolds number used is 30 000, with turbulent dispersion tracking, since this should be the most difficult case.

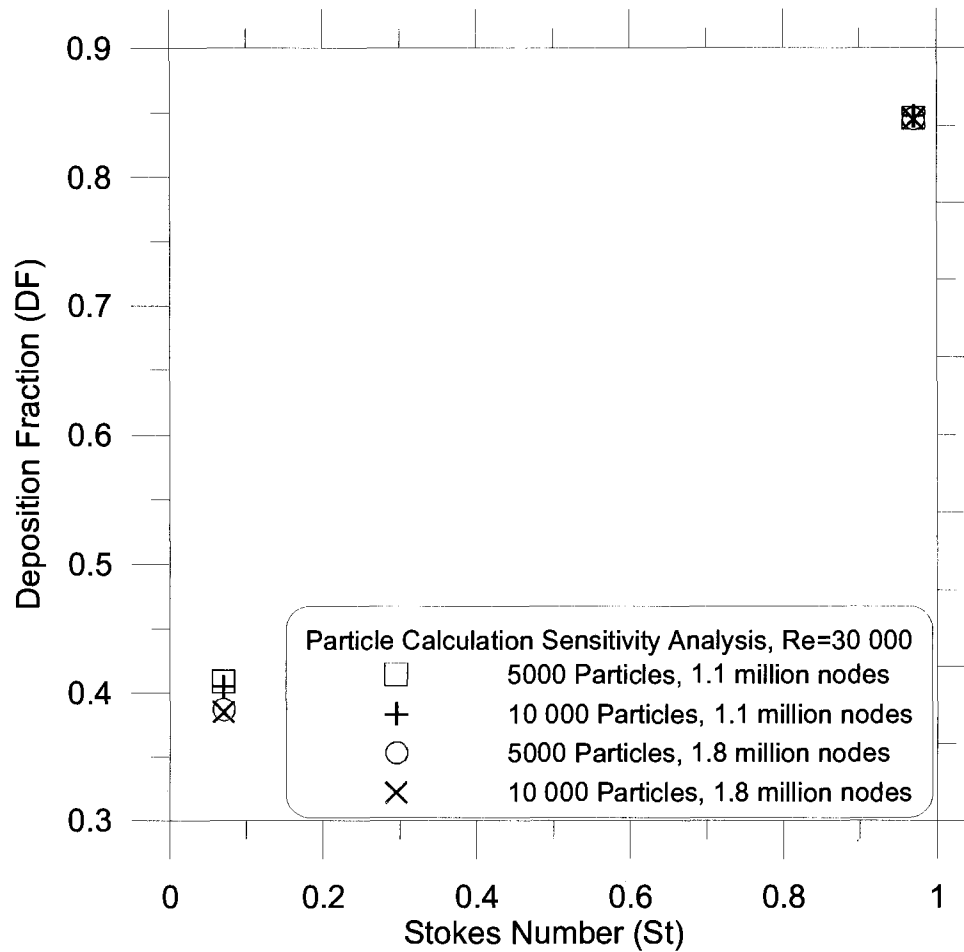


**Figure 6.5 Particle Sensitivity Analysis**  $\left( St = \frac{\rho_p d_p^2 Q}{18\pi\mu a^3} \right)$

For the 1.1 million node case (the number of nodes used in this study) there is less than 1% difference in the deposition fraction for either Stokes number when comparing simulations with either 5000 or 10 000 released particles. This indicates that the use of 10 000 particles was adequate. When this was repeated with 1.8 million nodes, it was also seen that the number of particles was adequate. Comparing the 1.1 million node case used in the current simulations with a higher resolution 1.8 million node test case, it seems that the 1.1 million nodes used for the particle calculation was adequate. The maximum difference in calculated deposition fraction between the two grid sizes is 0.02, which occurs at a Stokes number of

0.07 corresponding to the smallest value used in this thesis. The difference would be much smaller for the higher Stokes numbers and is negligible for the  $St=0.97$  case shown in Figure 6.5. Compared to the trends seen in the data discussed below, the maximum difference of 0.02 is quite small and the grid size of 1.1 million nodes with 10 000 released particles was deemed sufficiently accurate.

## **6.5 Results and Discussion**

### **6.5.1 Flow-field simulation results**

The single-phase flow is simulated in the computational domain (1 100 000 grid size) using RANS equations and the SST turbulence model. Figures 6.6 to 6.8 show the magnitude of mean velocities for different Reynolds numbers ( $Re = 10\,000$ ,  $20\,000$ , and  $30\,000$ , respectively) at the mid plane of the geometry and at several cross sections throughout the bend for different angles of  $0$ ,  $22.5$ ,  $45$ ,  $77.5$ , and  $90^\circ$ . Two-dimensional velocity vector plots at the exit of the bend for the three different Reynolds numbers are shown in Figure 6.9, indicating the formation of two helical counter-rotating vortices, as expected for the present range of Dean numbers ( $De = 3776$ ,  $7352$ , and  $11028$ ). These helical vortices are formed inside the bend because of a pressure gradient that is induced centrifugally, moving the slow fluid near the walls inward, while forcing the faster fluid in the core flow outward. From the figures, it can also be seen that the thickness of the boundary layers near the walls is decreased when the Reynolds number is increased. Turbulence kinetic energy distributions for the three different Reynolds numbers are shown from Figures 6.10 to 6.12, respectively.

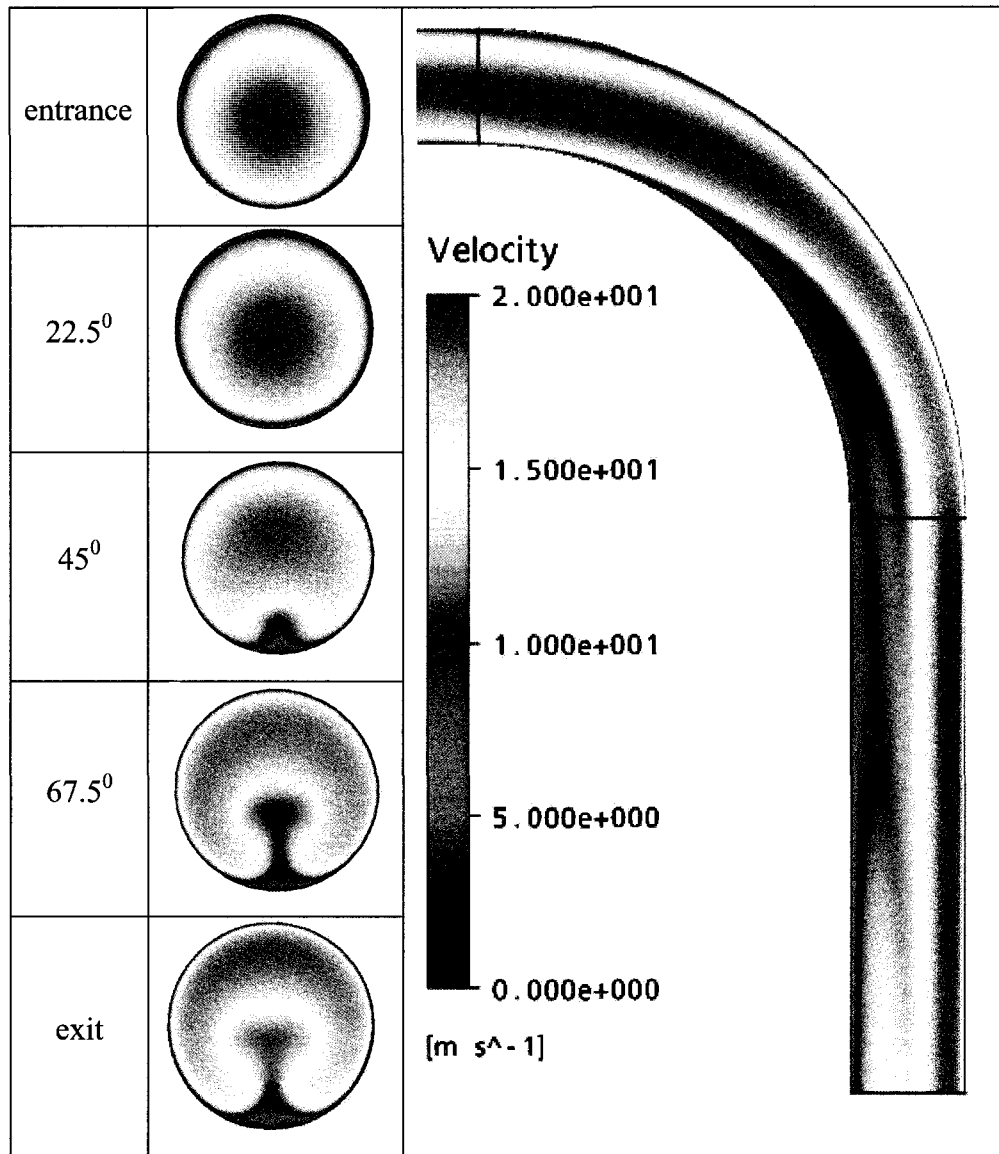


**Figure 6.6 Velocity Magnitude from RANS Results, Re = 10 000. (The radial axis runs vertically on the page for each of the cross-sectional views)**

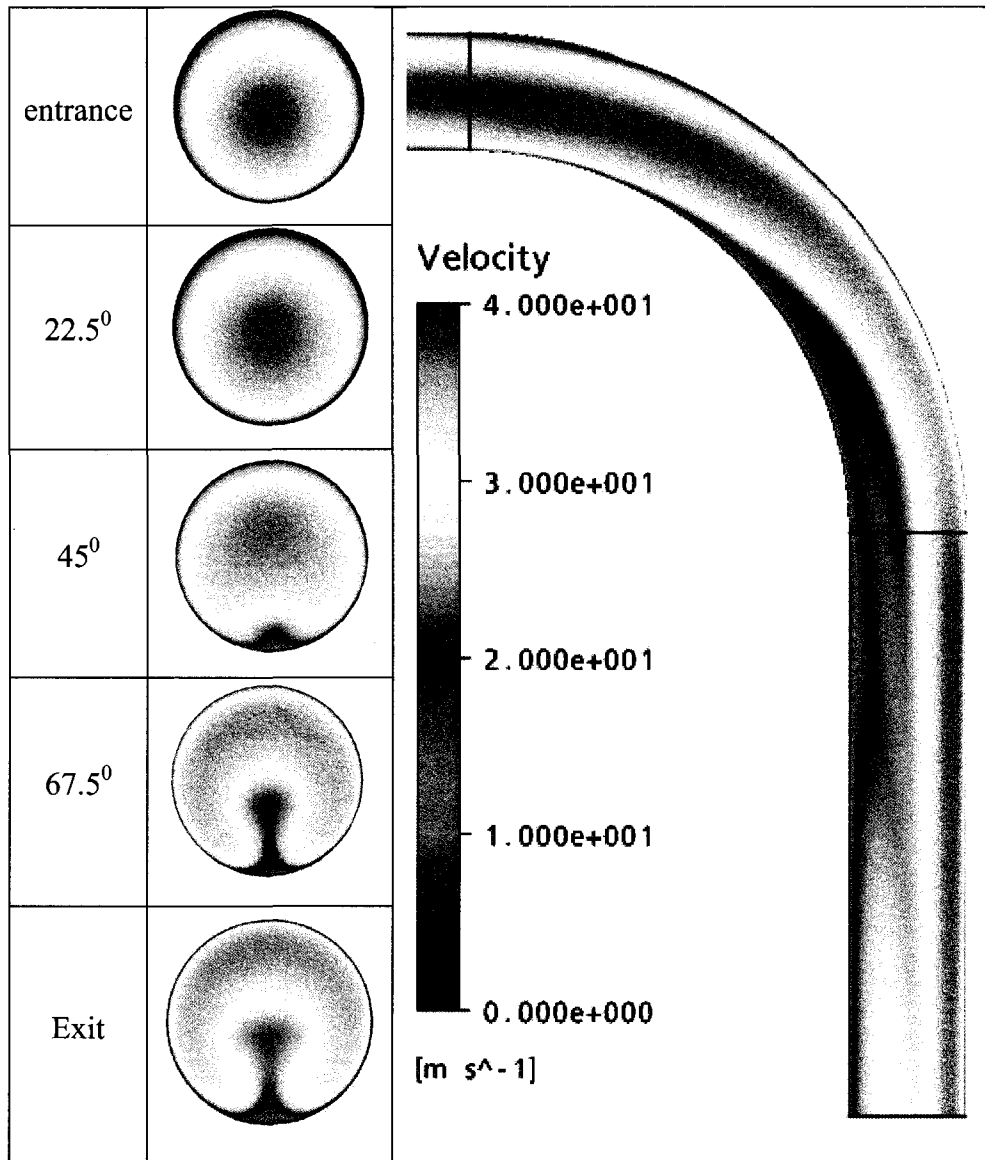


**Figure 6.7 Velocity Magnitude from RANS Results,  $Re = 20\ 000$  (The radial axis runs vertically on the page for each of the cross-sectional views).**

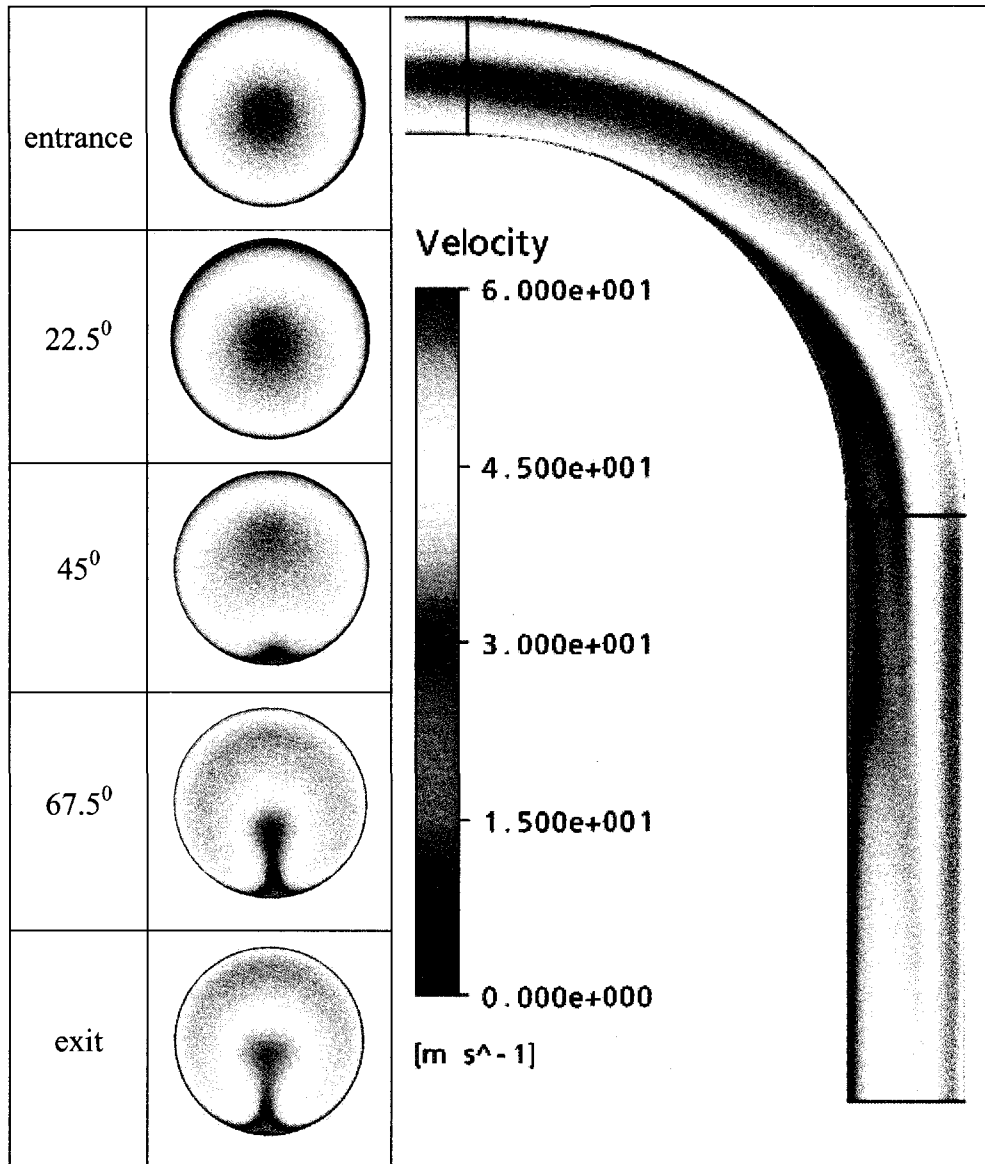


**Figure 6.8 Velocity Magnitude from RANS Results, Re = 30 000 (The radial axis runs vertically on the page for each of the cross-sectional views)**

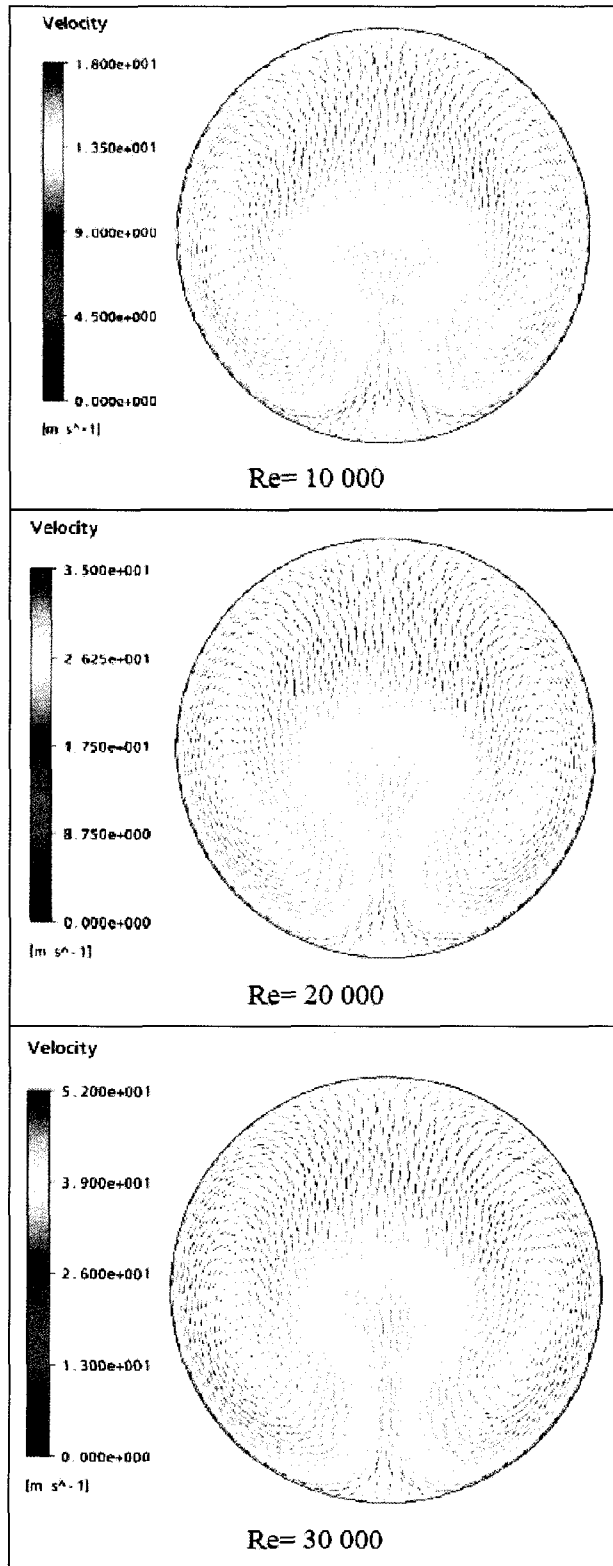


**Figure 6.9 Velocity in the Plane of the Bend Exit**

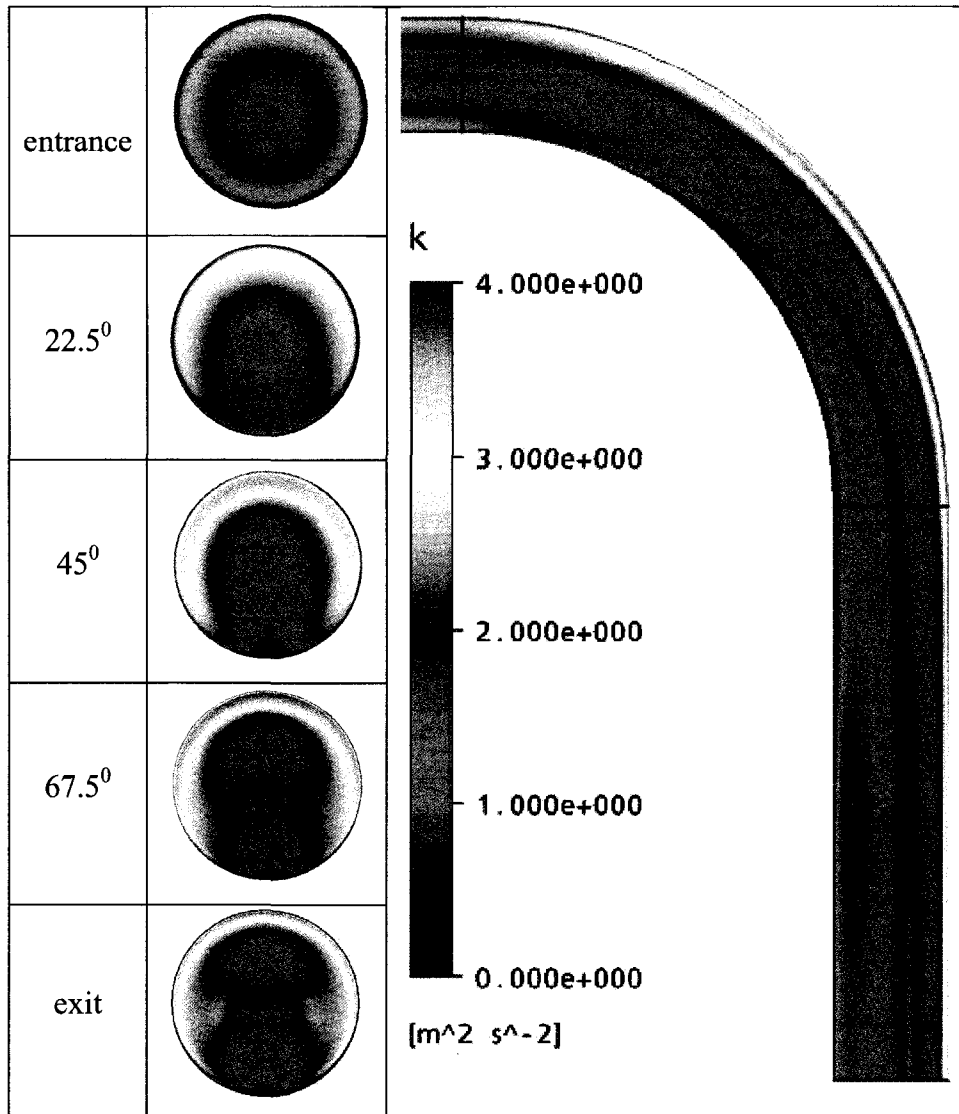


**Figure 6.10 Turbulent Kinetic Energy from RANS Results, Re = 10 000 (The radial axis runs vertically on the page for each of the cross-sectional views)**

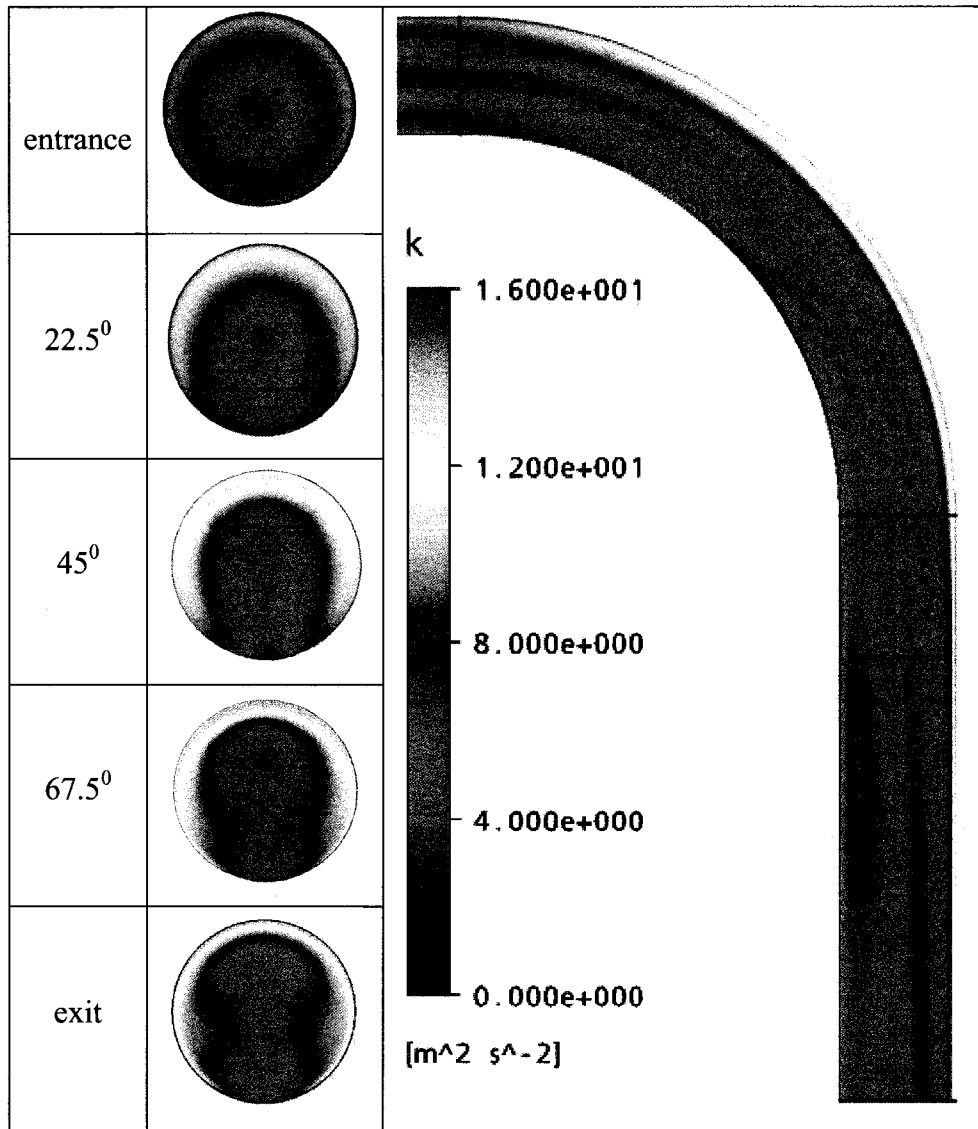


**Figure 6.11 Turbulent Kinetic Energy from RANS Results, Re = 20 000. (The radial axis runs vertically on the page for each of the cross-sectional views)**

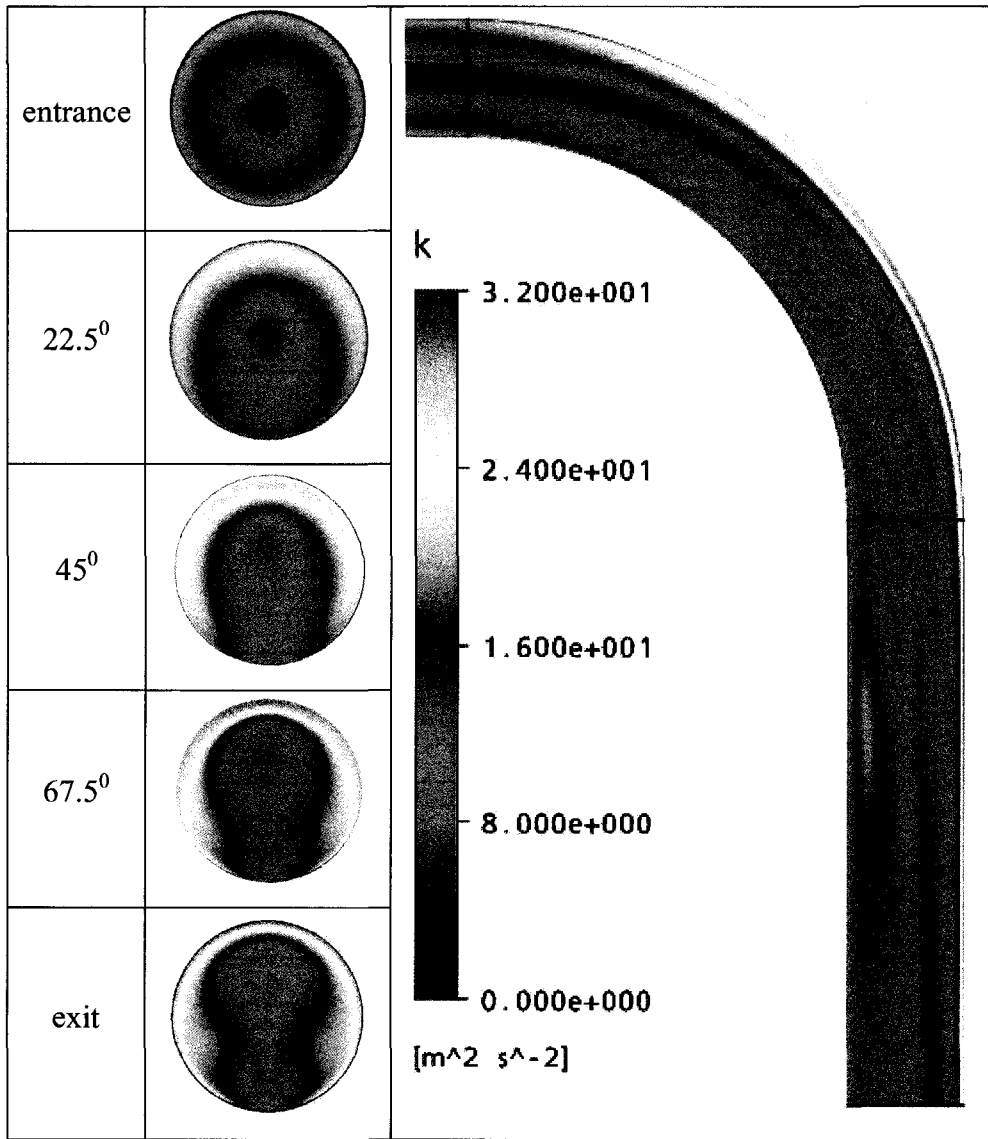


**Figure 6.12 Velocity Magnitude from RANS Results, Re = 30 000 (The radial axis runs vertically on the page for each of the cross-sectional views)**

## 6.5.2 Particle tracking simulation results

The particulate-phase is simulated using RANS equations and RANS/EIMs for mean flow tracking (turbulent dispersion turned off) and turbulent tracking (turbulent dispersion turned on), respectively. The numerical results for particle deposition fraction are tabulated in Table 6.1, for both mean flow tracking and turbulent dispersion tracking.

**Table 6.1: Deposition fractions obtained from numerical simulations (Curvature ratio = 7.4. Density ratio = 760)**

$St = \frac{\rho_p d_p^2 Q}{18\pi\mu a^3}$	Mean Flow Tracking			Turbulent Dispersion Tracking		
	Re=10 000	20 000	30 000	Re=10 000	20 000	30 000
0.07	0.07	0.09	0.09	0.20	0.34	0.39
0.20	0.30	0.30	0.29	0.44	0.49	0.51
0.39	0.58	0.55	0.54	0.59	0.64	0.67
0.65	0.82	0.78	0.76	0.73	0.77	0.82
0.97	0.93	0.92	0.90	0.87	0.89	0.92

The results without turbulent dispersion (mean flow tracking) are graphed against the experimental results in Figure 6.13, and those with turbulent dispersion turned on are graphed in Figure 6.14.

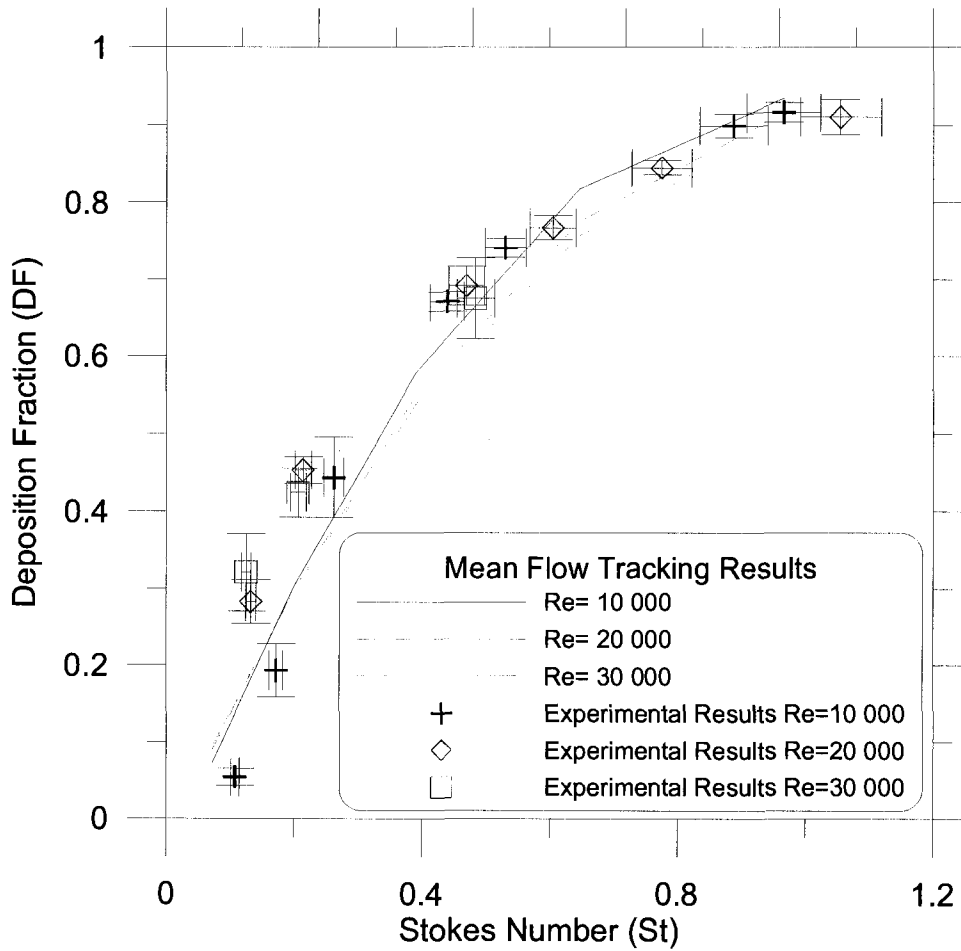


**Figure 6.13 Numerical Results (mean flow tracking) against Experimental Results**

$$\left( St = \frac{\rho_p d_p^2 Q}{18\pi\mu a^3} \right)$$

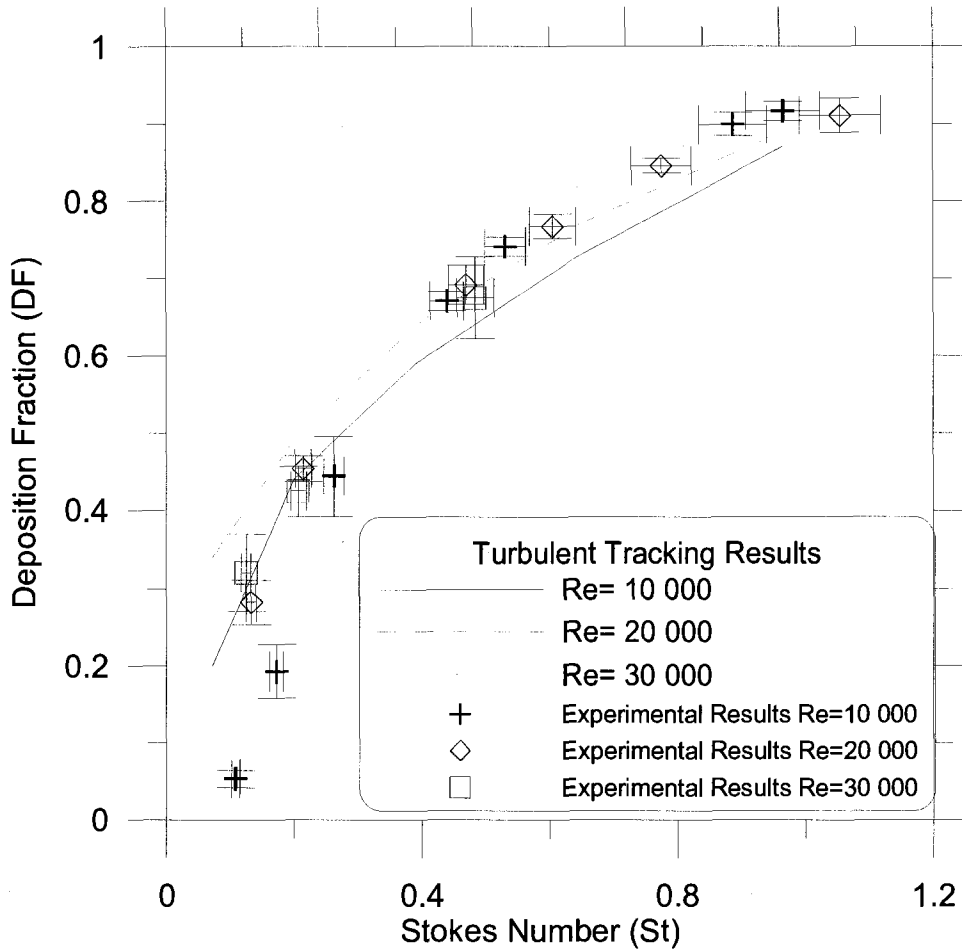


**Figure 6.14 Numerical Results (turbulent dispersion tracking) against Experimental**

**Results**  $\left( St = \frac{\rho_p d_p^2 Q}{18\pi\mu a^3} \right)$

In Figure 6.13 it is evident that the numerical results without the turbulent dispersion (mean flow tracking) closely resemble the experimental results, except that there is no apparent Reynolds number effect at the Stokes number of 0.15 (which is apparent in the experimental data). However, the general agreement with the experimental data indicates that the particle deposition in the present geometry is dominated by an inertial impaction mechanism. The absence of a Reynolds number effect in the simulations for Stokes numbers smaller than approximately 0.15, suggests that the Reynolds number effect found in the experiments in the same range could be due to a turbulent dispersion deposition mechanism.

In Figure 6.14 it can be seen that the numerical results with the inclusion of turbulent dispersion do not agree with the experimental results nearly as well as the mean flow tracking results in Figure 6.13. For Stokes numbers less than about 0.2, the numerical deposition results significantly overpredict the experimental results. Although a Reynolds number effect is apparent in the numerical results, it is present for all Stokes numbers in contrast to the experimental results, which showed Reynolds number dependence only for Stokes numbers smaller than 0.15. Higher Reynolds numbers produced higher deposition fractions but curiously, for Stokes numbers greater than 0.6, the inclusion of turbulent dispersion actually reduced the deposition fraction for the  $Re = 10\,000$  case and increased it for the  $Re = 30\,000$  case (compared to mean flow tracking).

The discrepancy of calculated particle deposition using the turbulent tracking simulation for low Stokes number comes from the fact that in the standard Eddy Interaction Model, the assumption of isotropic turbulence overestimates the velocity fluctuations normal to the walls, leading to an overprediction of particle deposition. Experimental observations indicate that the stream-wise turbulence kinetic energy component (see Equation 83) is approximately double the cross-stream component and about 4 times the size of the normal component (normal to the wall) in the boundary layer region close to the wall (Kundhu & Cohen, 2002). Away from the wall toward the edge of the boundary layer, the turbulence intensity tends to become isotropic (Kundhu & Cohen, 2002).

The turbulent tracking deposition in the bend is also affected by the turbulent dispersion of particles in the inlet pipe (prior to the bend). EIMs are also known to cause “spurious” concentration of particles in regions of low turbulence kinetic energy (near the walls in the present case) for particles having behaviour approaching that of fluid tracers (this

is discussed in section 2.6.2.). Therefore, some caution is needed for the interpretation of present turbulent tracking deposition. A more complete picture of particle deposition in the bend would require a Large Eddy Simulation with a dynamic particle tracking, but its implementation is beyond the scope of the present work. The particle deposition pattern showed a concentration of particles along the outside of the bend, with the inside of the bend relatively free of deposition. This is the same pattern seen by Breuer et al. (2006) for a Reynolds number of 10 000, for which the concentration towards the outside of the bend becomes more pronounced as the Stokes number increases, and there is a strip on the inside of the bend free of deposition.

Even though the turbulent tracking results carry some modeling uncertainty, the flow-field from the RANS calculation can still be examined. A graph showing the turbulence intensity ( $I$ ), half-way around the bend and at the bend exit, is shown as Figure 6.15. In terms of the non-dimensional variables introduced for the non-dimensional particle Equation (21), the nondimensional eddy velocity scale is

$$u_e^{(n)} = \frac{\sqrt{\frac{2k}{3}}}{V}. \quad (82)$$

The turbulence intensity ( $I$ ) based on the mean flow speed is (Schlichting, 1968)

$$I = \frac{\sqrt{u_e^2 + v_e^2 + w_e^2}}{V} = \frac{\sqrt{2k}}{V} = \sqrt{3}u_e^{(n)}. \quad (83)$$

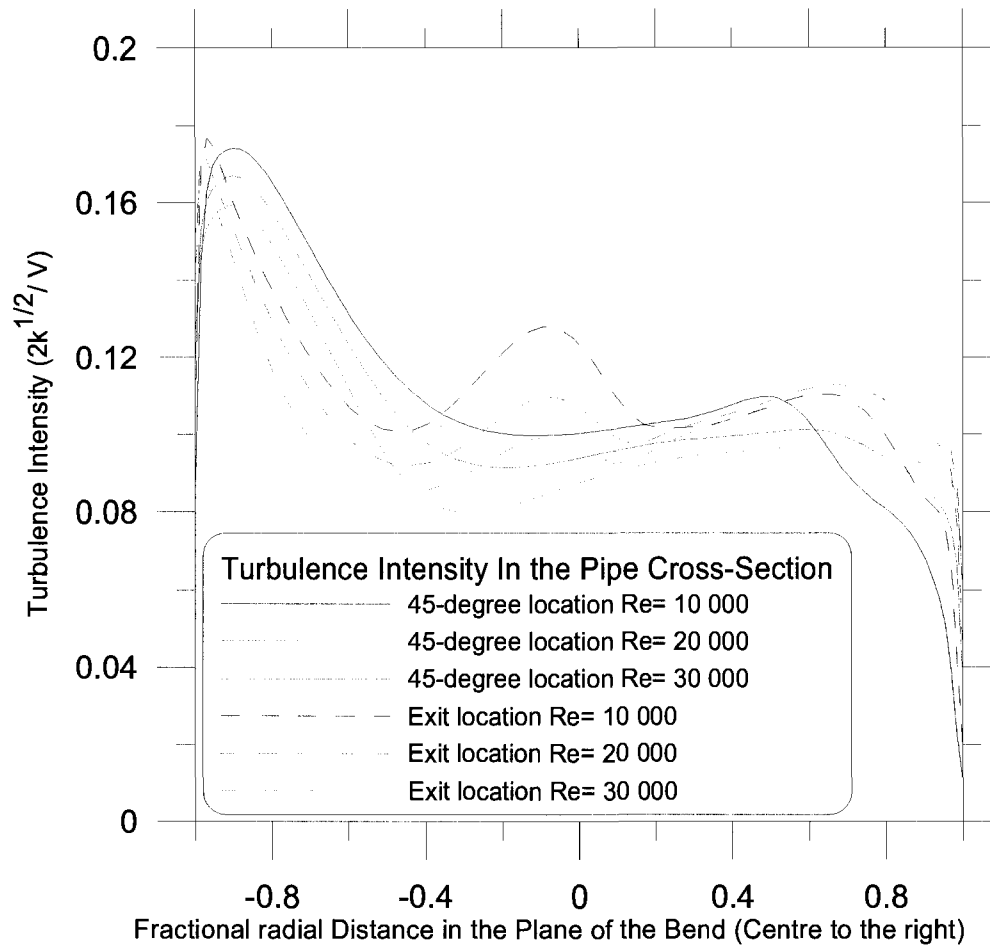


**Figure 6.15 Turbulence Intensity (I) Half-Way Around the Bend and at the Exit**

In Figure 6.15, it can be seen that the turbulence intensity is maximum close to the outside wall, but drops off to zero at the walls. The magnitudes are similar among the 3 cases. As the flow pattern develops with distance around the bend, this distribution becomes more skewed toward the outside of the bend. The impact of turbulence on the EIM occurs through the turbulence intensity (Equation 82) and the frequency of interaction with successive eddies (eddy interaction time). The impact of these on the particle equation of motion determines the modeling effect of the turbulence. It is hypothesized that the Re effect seen in the experimental results is due to an increase of the turbulent dispersion effect on the deposition fraction. The rest of this chapter is devoted to an attempt to explain why such an increase

only affects the particles with smaller Stokes numbers. This is attributed to the filtering out of the high frequencies by particles with Stokes numbers greater than 0.2.

### 6.5.3 Analytic Modeling of Particle Response to Turbulence

The particle equation can be represented by the Stokes drag particle equation (25) for making a simplified analysis of the response of particles to turbulent fluctuations (Tavoularis, 2005).

The equation (using a dimensional time, but non-dimensional velocities) is

$$\frac{aSt}{V} \frac{d\vec{V}_p^{(n)}}{dt} + \vec{V}_p^{(n)} = \vec{V}^{(n)} \quad (84)$$

Break the fluid into mean and fluctuating components  $\vec{V} = \vec{V}_m + \vec{V}'$

$$\frac{aSt}{V} \frac{d\vec{V}_p^{(n)}}{dt} + \vec{V}_p^{(n)} = \vec{V}_m^{(n)} + \vec{V}'^{(n)}. \quad (85)$$

This is a first order ordinary differential equation, with two inputs, the mean flow and the fluctuating flow. The solution is a sum of the solution to the mean flow and the solution to the fluctuating flow. We are interested in the solution to the fluctuating flow, so we want to solve

$$\frac{aSt}{V} \frac{d\vec{V}_p^{(n)}}{dt} + \vec{V}_p^{(n)} = \vec{V}'^{(n)} \quad (86)$$

The fluctuating component is composed of the range of frequencies making up the frequency spectrum of the turbulence. For a first order system with a sinusoidal input, the amplitude ratio is

$$\eta = \frac{1}{\sqrt{1 + (\omega\tau)^2}}, \quad (87)$$

where  $\omega$  is the input circular frequency and  $\tau$  is the time constant. In this case, the time constant is

$$\tau = \frac{aSt}{V}, \quad (88)$$

so the amplitude of the particle fluctuations divided by the fluid fluctuations is

$$\eta = \frac{1}{\sqrt{1 + \left(\frac{\omega aSt}{V}\right)^2}} \quad (89)$$

This amplitude ratio is a quantitative indication of the ability of a particle to track turbulent fluctuations in the flow occurring at a specified frequency. A large amplitude ratio indicates that the particle and flow fluctuations are similar, which means that the particle is able to follow turbulent fluctuations at the specified frequency. Conversely, a small amplitude ratio means that flow fluctuations are damped by the particle inertia so that in effect, the turbulent flow fluctuations are filtered out, and the particle does not respond to the relevant frequency of fluctuation.

To detect whether any of the frequencies making up the frequency spectrum of the turbulence are filtered out (as evidenced by a small amplitude ratio), the amplitude ratio can be analyzed for the highest frequency, given by the Kolmogorov time scale

$$\omega_K = \frac{2\pi}{\sqrt{\frac{V}{\varepsilon}}}, \quad (90)$$

where the denominator is the Kolmogorov time scale, representing the time scale of the smallest eddies.

Another relevant frequency to be examined is based on the eddy time scale (the overall average frequency used for the EIM), which is

$$\omega_e = \frac{2\pi}{0.20 \frac{k}{\varepsilon}} \quad (91)$$

The denominator is the eddy time scale. The eddy frequency equals 2.83 times the turbulent eddy frequency in the  $k - \omega$  turbulence model, which was used in the RANS calculation.

Thirdly, a frequency associated with the largest eddies can be used, which is roughly given by

$$\omega_L = \frac{2\pi}{\frac{a}{\sqrt{\frac{2k}{3}}}} \quad (92)$$

In this case, the time scale used is simply the pipe radius ( $a=0.005115$  m) divided by the eddy velocity scale.

The kinematic viscosity for air is  $\nu = 1.5 \times 10^{-5} \text{ m}^2/\text{s}$ . To obtain a value for the turbulent eddy dissipation,  $\varepsilon$ , the volume averages from the RANS results are used (averaged over the whole domain: entrance pipe, bend, and exit pipe). For the turbulent kinetic energy,  $k$ , a turbulence intensity of 0.1 is used (based on Figure 6.15). Using these values, Table 6.2 shows the frequency scales and the amplitude ratios at these different frequency scales as a function of Reynolds number.

It is important to note that the frequency range of the turbulence ( $\omega_k - \omega_L$ ) increases as the Reynolds number increases. For a doubling of the Reynolds number, the frequency range increases by roughly a factor of 2.6. Also, the frequencies are almost all added to the high frequency range of the spectrum. Although the kinetic energy is divided up among more frequencies, generally the kinetic energy at any one frequency has been increased. This is because the turbulence intensities are roughly the same for the 3 cases (Figure 6.15), so the

kinetic energy (see Equation 83) increases proportionally to the Reynolds number squared. This conclusion assumes that the energy spectrum has roughly the same shape for the different Reynolds numbers. This should be roughly true, according to the dimensionality argument of Kolmogorov (for example see Kundhu and Cohen, 2002).

**Table 6.2 Turbulent Frequency Scales and Corresponding Particle Amplitude Ratios**

Re	V (m/s)	$\varepsilon$ (m <sup>2</sup> /s <sup>3</sup> )	$\omega_K$ (10 <sup>4</sup> 1/s)	$\omega_e$ (10 <sup>4</sup> 1/s)	$\omega_L$ (10 <sup>4</sup> 1/s)	$\eta_K$	$\eta_e$	$\eta_L$
10 000	15.42	2527	8.2	6.7	0.11	$\frac{1}{\sqrt{1+742St^2}}$	$\frac{1}{\sqrt{1+492St^2}}$	$\frac{1}{\sqrt{1+0.13St^2}}$
20 000	30.84	18037	22	12	0.22	$\frac{1}{\sqrt{1+1324St^2}}$	$\frac{1}{\sqrt{1+387St^2}}$	$\frac{1}{\sqrt{1+0.13St^2}}$
30 000	46.26	51592	37	15	0.33	$\frac{1}{\sqrt{1+1683St^2}}$	$\frac{1}{\sqrt{1+287St^2}}$	$\frac{1}{\sqrt{1+0.13St^2}}$

Kolmogorov argued that if the fluctuations are isotropic, there is an intermediate range of wavenumbers (the inertial sub-range) for which the functional dependence of the kinetic energy distribution per wave number ( $S(K)$ ) is

$$S(K) = f(\varepsilon, K), \quad (93)$$

where  $K$  is the wavenumber, and by the Buckingham Pi Theorem,

$$S \propto \varepsilon^{2/3} K^{-5/3} \quad (94)$$

The same argument has been applied to the frequency spectrum,

$$\begin{aligned} S(\omega) &= f(\varepsilon, \omega) \\ S(\omega) &\propto \varepsilon \omega^{-2} \end{aligned} \quad (95)$$

Higher frequencies (or wavenumbers) are associated with less energy. At the high end of the spectrum, the energy has the Kolmogorov frequency, and is dissipated out by viscosity. This

indicates that the frequency spectrum has the same general shape even when the Reynolds number changes.

The amplitude ratios of the particle and flow fluctuations are now graphed in Figure 6.16, to show the particle amplitude response to the turbulence.

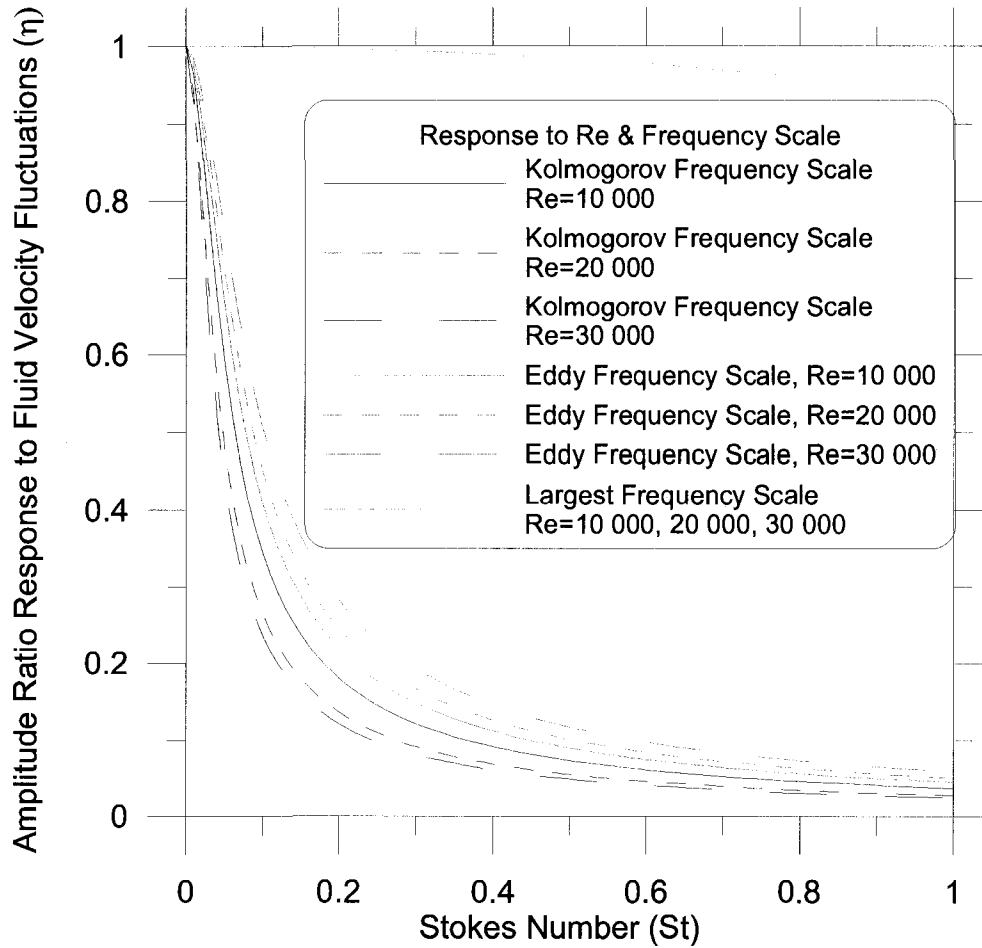


**Figure 6.16 Particle Amplitude Ratio Response to Velocity Fluctuations at Different Turbulent Frequency Scales**

From Figure 6.16, it is evident that the particle amplitude response to the lowest frequencies in the turbulence is essentially 100% for all three Reynolds numbers and for Stokes numbers below 1. However, there is significant damping for fluctuations occurring at both the eddy frequency scale and the Kolmogorov frequency scale, representing the highest frequencies

present in the flow. In fact, these two frequency scales are similar in magnitude, and for Stokes numbers larger than 0.2, the amplitude response of the particle is almost negligible for these frequencies for all three Reynolds numbers. For Stokes numbers less than 0.2, the response to the eddy frequency scale and the Kolmogorov frequency scale is generally significant, and increases strongly as the particle Stokes number decreases.

Based on the calculated particle responses shown in Figure 6.16, it can be generally said that high frequency eddies that are added to the frequency spectrum of the turbulence with increased Reynolds number will not be felt by particles with Stokes numbers greater than 0.2. Conversely, for particles with Stokes numbers below 0.2, the increase in the range of the frequency spectrum due to an increase in the Reynolds number will affect the particle response. This potentially explains why the Reynolds number effect on deposition is only apparent in the range of Stokes numbers below 0.2.

## Chapter 7: Conclusions

Particle deposition in a  $90^\circ$  bend with an aspect ratio of  $R/a = 7.4$  was studied experimentally and numerically for three different Reynolds numbers ( $Re = 10\,000, 20\,000, 30\,000$ ) based on the inlet diameter. The Stokes number was varied from 0.1 to 0.9. A new experimental setup for aerosol deposition using a spectroscopy technique was built and verified against experimental data available in the literature (Pui et al., 1987,  $R/a = 5.7, Re = 10\,000$ ). The overall experimental results indicate that there is a small Reynolds number effect on the deposition fraction for turbulent bend flows. For low Stokes numbers (near 0.15), there is an increase in the deposition fraction result of about 0.10 when the Reynolds number is increased from 10 000 to 20 000. Numerical calculations using the RANS equations with the Shear Stress Transport turbulence model were performed to see whether the experimental result could be better understood. There was good agreement between the numerical results and the experimental results for mean flow tracking, indicating the dominant influence of particle deposition by inertial impaction. The Reynolds number effect seen in the experimental data was not captured with this model, suggesting that the effect was likely due to turbulent dispersion. While an eddy interaction model was included to simulate the turbulent dispersion, due to the limitations of this model, it was not possible to reproduce the experimental results. However, an analytical analysis of the flow-field based on the RANS results provided a potential explanation for the effect not being apparent at the higher Stokes numbers based on a damped particle response to turbulence. These results and observations are important considerations for modeling of transport and deposition of aerosols having a range of scales. The Reynolds number influence (in the range studied) could be extrapolated (with caution) to higher Reynolds numbers.

## References

- Agilent Technologies (2003) Agilent 8453 UV-visible Spectroscopy System. Operators Manual. P/N G1115-90021.
- American Society of Mechanical Engineers (1985) Part 1 Measurement Uncertainty, Instruments and Apparatus. ANSI/ASME PTC 19.1-1985.
- Basset, A.B. (1888) A treatise on hydrodynamics, 2: 285. Dover.
- Bauman, R.P., Poe, R. (1962) Absorbtion spectroscopy. New York. Wiley.
- Breuer, M., Baytekin, H.T., Matida, E.A. (2006) Prediction of aerosol deposition in 90<sup>0</sup> bends using LES and an efficient Lagrangian tracking method. Journal of Aerosol Science 37, 1407-1428.
- Brooks Instrument (2000) Installation and operation manual. Brooks smart series (TMF) mass flow meters, models 5860S, 5861S, 5863S, 5864S & mass flow controllers, models 5850S, 5851S, 5853S. P/N 541-C-051-AAG rev. F
- Brun, R.J., Lewis, W., Perkins, P.J., Serafini, J.S. (1953) Impingement of cloud droplets on a cylinder and procedure for measuring liquid-water content and droplet sizes in supercooled clouds by rotating multicylinder method. NACA TR 1215.
- Chen, B.T., Cheng, Y.S., Yeh, H.C. (1985) Performance of a TSI aerodynamic particle sizer. Aerosol Science and Technology. 4, 89-97.
- Cheng Y.S. and Wang C.S. (1975) Inertial deposition of particles in a bend. J. Aerosol Sci. 6, 139-145.
- Cheng Y.S. and Wang C.S. (1981) Motion of particles in bends of circular pipes. Atmospheric Environment 15, 301-306.
- Crane, R.I., Evans, R.L. (1977) Inertial deposition of particles in a bent pipe. J. Aerosol Sci.. Vol. 8 pp. 161 to 170.
- DeHaan, W.H. and Finlay, W.H. (2001) In vitro monodisperse aerosol deposition in a mouth and throat with six different inhalation devices. Journal of Aerosol Medicine, 14, 3, 361-367.
- Dennis, S.C.R., Ng, M. (1982) Dual solutions for steady laminar flow through a curved tube. The Quarterly Journal of Mechanics & Applied Mathematics. 35: 305-324.
- Elghobashi, S. (1994) On predicting particle-laden turbulent flows. Applied Scientific Research. 52: 309-329.

- Finlay, W.H. (2001) The mechanics of inhaled pharmaceutical aerosols. Academic Press. New York.
- Ganic, E.N., Mastanaiah, K.M. (1981) Investigation of droplet deposition from a turbulent gas stream. *Int. J. Multiphase Flow*. 7:401-422.
- Gosman, A.D., Ioannides, E. (1981) Aspects of computer simulations of liquid-fuelled combustors. American Institute of Aeronautics and Astronautics. 19<sup>th</sup> Aerospace Sciences meeting, St. Louis, MO, Jan. 12-15, 1981.
- Hacker, P.T., Brun, R.J. and Boyd, B. (1953) Impingement of droplets in 90° elbows with potential flow. NACA Technical Note, No. 2999.
- Hoffmann, K.A., Chiang, S.T. (2000) Computational Fluid Dynamics. Volume III. Fourth Edition. Engineering Education System. Wichita.
- Ilie, M., Matida, E.A., Finlay, W.H. (2008) Asymmetrical aerosol deposition in an idealized mouth with a DPI mouthpiece inlet. *Aerosol Science and Technology*, 42, 10-17.
- Johnston and Muir (1973). Inertial deposition of particles in the lung. *Aerosol Science*, 4, 269-270.
- Johnston J.R., Isles K.D. and Muir D.C.F. (1977) Inertial deposition of particles in human branching airways . *Inhaled Particles* (edited by Walton W.H.) 4, 61-72.
- Kaimal, M.R., Devanathan, R. (1980) Motion of a viscous fluid with suspended particles in a curved tube. *International Journal of Engineering Science*. 18:847-854.
- Kundu, Pijush K., Cohen Ira M., *Fluid Mechanics*, 2<sup>nd</sup> edition. Academic Press. San Diego, 2002.
- Landahl, H.D. and Herrmann, R.G. (1949) Sampling of liquid aerosols by wires, cylinders and slides and efficiency of impaction of the droplets. *J. Colloid Sci.* 4, 103-136
- Matida, E.A., Finlay, W.H., Lange, C.F., and Grgic, B. (2004) Improved numerical simulation of aerosol deposition in an idealized mouth-throat. *Aerosol Science*, 35, 1-19.
- McCoy, D.D., Hanratty, T.J. (1977) Rate of deposition of droplets in annular two-phase flow. *Int. J. Multiphase Flow* 3:319-331.
- McFarland, A.R., Gong, H., Muyschondt, A., Wentz, W.B., Anand, N.K. (1997) Aerosol deposition in bends with turbulent flow. *Environ. Sci. Technol.* 31, 3371-3377.
- Menter, F.R. (1994) Two-equation Eddy-viscosity turbulence models for engineering applications. *AIAA Journal*. Vol. 32 #8, pp 1598-1605.
- Peters T.M. and Leith D. Particle deposition in industrial duct bends (2004). *Ann. Occup. Hyg.* 48, 483-490.

- Pui, D.Y.H., Romay-Novas, F., Liu, B.Y.H. (1987) Experimental Study of Particle Deposition in Bends of Circular Cross Section. *Aer.Sc.Tech.*7:301-315.
- Reeks, M.W. (1983) The transport of discrete particles in inhomogeneous turbulence. *J. Aerosol Science.* 14 (6):729-739.
- Reist, P.C. (1984) Introduction to aerosol science. MacMillan Publishing Company, New York.
- Rouhiainen, P.O., Stachiewicz, J. W. (1970) On the deposition of small particles from turbulent streams. *Journal of Heat Transfer*, 92:169
- Saffman, P.G. (1965) The lift on a small sphere in a slow shear flow. *J. Fluid Mech.* 22: 385-400.
- Sato, S., Chen, D., and Pui, D.Y.H. (2003). Particle transport at low pressure: deposition in bends of a circular cross-section. *Aerosol Science and Technology*, 37, 770-779.
- Schiller, L., Naumann, Z. (1935). A drag coefficient correlation. *Z. Ver. Deutsch Ing.* 77:318.
- Schlichting, H. (1968). *Boundary-Layer Theory*. New York. McGraw-Hill.
- Stone, H.A. (2000) Phillip Saffman and viscous flow theory. *J. Fluid Mech.* 409:165-183.
- Tavoularis, S. (2005) *Measurement in fluid mechanics*. Cambridge University Press.
- Tsai, C. and Pui, D.Y.H. (1990) Numerical study of particle deposition in bends of a circular cross-section--Laminar flow regime. *Aerosol Science and Technology*. 12, 813-831.
- TSI (2002), Model 3450 Vibrating orifice aerosol generator instruction manual. P/N 1933450, Revision L.
- TSI (2003), Models 3054/3054A Aerosol neutralizers instruction manual. P/N 1933054, Revision K.
- TSI (2004), PSD 3603 Particle size distribution analyzer instruction manual. P/N 1930068, Revision F.
- Yeh, H. (1974) Use of a heat transfer analogy for a mathematical model of respiratory tract deposition. *Bulletin of Mathematical Biology*. 36, 105-116.
- White, F.M. (1998) *Fluid Mechanics*. McGraw-Hill.
- Yeung, W. (1979) *Wear*. 55, 91-106.

## Appendix A: The Fluid Equations

For flow around a bend it is simpler to use angular coordinates. Polar coordinates  $(r, \alpha)$  are used for the tube cross-section. The distance around the bend is described by the angular distance,  $\theta$ . The curve radius to the centreline of the bend is  $R$ .

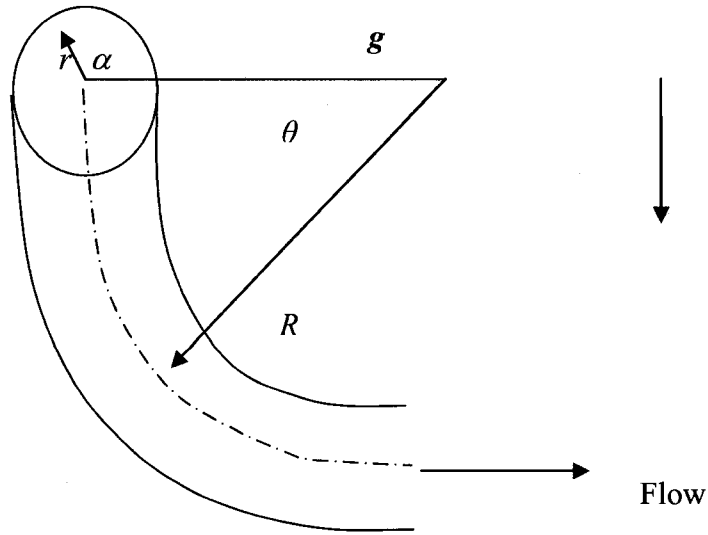


**Figure A1: Toroidal Coordinates for the Bend**

Let the velocity components for  $(r, \alpha, \theta)$  be  $(u, v, w)$ . The continuity equation is:

$$\frac{\partial u}{\partial r} + \frac{\partial v}{r \partial \alpha} + \frac{1}{R + r \cos \alpha} \frac{\partial w}{\partial \theta} + \frac{u}{r} - \frac{v \sin \alpha}{R + r \cos \alpha} + \frac{u \cos \alpha}{R + r \cos \alpha} = 0 \quad (\text{A1})$$

The Navier-Stokes equation, broken into component directions, is:

The  $r$  direction:

$$\begin{aligned}
& \frac{\partial u}{\partial t} - \frac{v^2}{r} + v \frac{\partial u}{r \partial \alpha} + u \frac{\partial u}{\partial r} + \frac{w}{R+r \cos \alpha} \frac{\partial u}{\partial \theta} - \frac{w^2 \cos \alpha}{R+r \cos \alpha} = \\
& \frac{-1}{\rho} \frac{\partial P}{\partial r} - g \sin \theta \cos \alpha + \\
& \frac{\mu}{\rho} \left\{ \frac{-2}{r^2} \frac{\partial v}{\partial \alpha} - \frac{u}{r^2} + \frac{1}{r^2} \frac{\partial^2 u}{\partial \alpha^2} + \frac{1}{r} \frac{\partial u}{\partial r} + \frac{\partial^2 u}{\partial r^2} + \frac{v \sin \alpha}{(R+r \cos \alpha)r} - \frac{\frac{\partial u}{r \partial \alpha} \sin \alpha}{(R+r \cos \alpha)} + \right. \\
& \left. \frac{\frac{\partial u}{\partial r} \cos \alpha}{(R+r \cos \alpha)} + \frac{v \sin \alpha \cos \alpha}{(R+r \cos \alpha)^2} - \frac{u \cos^2 \alpha}{(R+r \cos \alpha)^2} + \frac{\frac{\partial^2 u}{\partial \theta^2}}{(R+r \cos \alpha)^2} - \frac{2 \frac{\partial w}{\partial \theta} \cos \alpha}{(R+r \cos \alpha)^2} \right\}
\end{aligned} \tag{A2}$$

The  $\alpha$  direction:

$$\begin{aligned}
& \frac{\partial v}{\partial t} + v \frac{\partial v}{r \partial \alpha} + \frac{vu}{r} + u \frac{\partial v}{\partial r} + \frac{w}{R+r \cos \alpha} \frac{\partial v}{\partial \theta} + \frac{w^2 \sin \alpha}{R+r \cos \alpha} = \\
& \frac{-1}{\rho} \frac{\partial P}{r \partial \alpha} + g \sin \theta \sin \alpha + \\
& \frac{\mu}{\rho} \left\{ \frac{-v}{r^2} + \frac{1}{r^2} \frac{\partial^2 v}{\partial \alpha^2} + \frac{2}{r^2} \frac{\partial u}{\partial \alpha} + \frac{1}{r} \frac{\partial v}{\partial r} + \frac{\partial^2 v}{\partial r^2} - \frac{\frac{\partial v}{r \partial \alpha} \sin \alpha}{(R+r \cos \alpha)} - \frac{u \sin \alpha}{(R+r \cos \alpha)r} + \right. \\
& \left. \frac{\frac{\partial v}{\partial r} \cos \alpha}{(R+r \cos \alpha)} - \frac{v \sin^2 \alpha}{(R+r \cos \alpha)^2} + \frac{\frac{\partial^2 v}{\partial \theta^2}}{(R+r \cos \alpha)^2} + \frac{u \cos \alpha \sin \alpha}{(R+r \cos \alpha)^2} + \frac{2 \frac{\partial w}{\partial \theta} \sin \alpha}{(R+r \cos \alpha)^2} \right\}
\end{aligned} \tag{A3}$$

The  $\theta$  direction:

$$\begin{aligned}
& \frac{\partial w}{\partial t} + v \frac{\partial w}{r \partial \alpha} + u \frac{\partial w}{\partial r} - wv \frac{\sin \alpha}{R+r \cos \alpha} + uw \frac{\cos \alpha}{R+r \cos \alpha} + \frac{w}{R+r \cos \alpha} \frac{\partial w}{\partial \theta} = \\
& \frac{-1}{\rho(R+r \cos \alpha)} \frac{\partial P}{\partial \theta} + g \cos \theta + \\
& \frac{\mu}{\rho} \left\{ \frac{1}{r^2} \frac{\partial^2 w}{\partial \alpha^2} + \frac{1}{r} \frac{\partial w}{\partial r} + \frac{\partial^2 w}{\partial r^2} - \frac{\frac{\partial w}{r \partial \alpha} \sin \alpha}{(R+r \cos \alpha)} + \frac{\frac{\partial w}{\partial r} \cos \alpha}{(R+r \cos \alpha)} - \right. \\
& \left. \frac{2 \sin \alpha \frac{\partial v}{\partial \theta}}{(R+r \cos \alpha)^2} + \frac{2 \cos \alpha \frac{\partial u}{\partial \theta}}{(R+r \cos \alpha)^2} - \frac{w}{(R+r \cos \alpha)^2} + \frac{\frac{\partial^2 w}{\partial \theta^2}}{(R+r \cos \alpha)^2} \right\}
\end{aligned} \tag{A4}$$

To identify the important parameters, the equations are put into non-dimensional form. It is assumed that the secondary flow is significant, so that the secondary centripetal accelerations are of the same magnitude as the primary centripetal acceleration. This secondary flow is stream-wise oriented vortices, so the secondary centripetal acceleration scales off the tube radius (see for example Berger et al. 1983).

$$\begin{aligned}\frac{u^2}{a} &\approx \frac{v^2}{a} \approx \frac{w^2}{R} \\ u \approx v &\approx \sqrt{\frac{a}{R}} w = \frac{w}{\sqrt{\delta}}\end{aligned}\tag{A5}$$

The curvature ratio is  $\delta$ . For the non-dimensional velocities to be of similar magnitude:

$$\begin{aligned}w^{(n)} &= w/V \\ u, v &\approx \frac{w^{(n)}V}{\sqrt{\delta}} \\ u^{(n)}, v^{(n)} &\approx w^{(n)} \approx \frac{u, v\sqrt{\delta}}{V} \\ u^{(n)} &= \frac{u\sqrt{\delta}}{V} \\ v^{(n)} &= \frac{v\sqrt{\delta}}{V}\end{aligned}\tag{A6}$$

The non-dimensional variables used are:

$$\begin{aligned}r^{(n)} &= r/a \\ v^{(n)} &= v\sqrt{\delta}/V \\ u^{(n)} &= u\sqrt{\delta}/V \\ w^{(n)} &= w/V \\ P^{(n)} &= P/\rho V^2 \\ t^{(n)} &= tV/a\end{aligned}\tag{A7}$$

The non-dimensional continuity equation is:

$$\frac{\partial u^{(n)}}{\partial r^{(n)}} + \frac{\partial v^{(n)}}{r^{(n)} \partial \alpha} + \frac{1}{\delta + r^{(n)} \cos \alpha} \frac{\partial w^{(n)}}{\partial \theta} + \frac{u^{(n)}}{r^{(n)}} - \frac{v^{(n)} \sin \alpha}{\delta + r^{(n)} \cos \alpha} + \frac{u^{(n)} \cos \alpha}{\delta + r^{(n)} \cos \alpha} = 0 \quad (\text{A8})$$

The non-dimensional Navier-Stokes equation (in component directions) is:

The r direction:

$$\begin{aligned} & \frac{\partial u^{(n)}}{\partial t^{(n)}} - \frac{v^{(n)2}}{\sqrt{\delta} r^{(n)}} + \frac{v^{(n)}}{\sqrt{\delta}} \frac{\partial u^{(n)}}{r^{(n)} \partial \alpha} + \frac{u^{(n)}}{\sqrt{\delta}} \frac{\partial u^{(n)}}{\partial r^{(n)}} + \frac{w^{(n)}}{\delta + r^{(n)} \cos \alpha} \frac{\partial u^{(n)}}{\partial \theta} \\ & - \frac{\sqrt{\delta} w^{(n)2} \cos \alpha}{\delta + r^{(n)} \cos \alpha} = -\sqrt{\delta} \frac{\partial P^{(n)}}{\partial r^{(n)}} - \frac{a \sqrt{\delta} g}{V^2} \sin \theta \cos \alpha + \\ & \text{Re} \left[ \begin{aligned} & \frac{-2}{r^{(n)2}} \frac{\partial v^{(n)}}{\partial \alpha} - \frac{u^{(n)}}{r^{(n)2}} + \frac{1}{r^{(n)2}} \frac{\partial^2 u^{(n)}}{\partial \alpha^2} + \frac{1}{r^{(n)}} \frac{\partial u^{(n)}}{\partial r^{(n)}} + \frac{\partial^2 u^{(n)}}{\partial r^{(n)2}} \\ & + \frac{v^{(n)} \sin \alpha}{(\delta + r^{(n)} \cos \alpha) r^{(n)}} - \frac{\frac{\partial u^{(n)}}{r^{(n)} \partial \alpha} \sin \alpha}{\delta + r^{(n)} \cos \alpha} + \frac{\frac{\partial u^{(n)}}{\partial r^{(n)}} \cos \alpha}{\delta + r^{(n)} \cos \alpha} + \frac{v^{(n)} \sin \alpha \cos \alpha}{(\delta + r^{(n)} \cos \alpha)^2} \\ & - \frac{u^{(n)} \cos^2 \alpha}{(\delta + r^{(n)} \cos \alpha)^2} + \frac{\frac{\partial^2 u^{(n)}}{\partial \theta^2}}{(\delta + r^{(n)} \cos \alpha)^2} - \frac{2\sqrt{\delta} \frac{\partial w^{(n)}}{\partial \theta} \cos \alpha}{(\delta + r^{(n)} \cos \alpha)^2} \end{aligned} \right] \end{aligned} \quad (\text{A9})$$

The  $\alpha$  direction:

$$\begin{aligned}
& \frac{\partial v^{(n)}}{\partial t^{(n)}} + \frac{v^{(n)}}{\sqrt{\delta}} \frac{\partial v^{(n)}}{r^{(n)} \partial \alpha} + \frac{v^{(n)} u^{(n)}}{\sqrt{\delta} r^{(n)}} + \frac{u^{(n)}}{\sqrt{\delta}} \frac{\partial v^{(n)}}{\partial r^{(n)}} + \frac{w^{(n)}}{\delta + r^{(n)} \cos \alpha} \frac{\partial v^{(n)}}{\partial \theta} + \frac{\sqrt{\delta} w^{(n)2} \sin \alpha}{\delta + r^{(n)} \cos \alpha} = \\
& -\sqrt{\delta} \frac{\partial P^{(n)}}{r^{(n)} \partial \alpha} + \frac{a\sqrt{\delta} g}{V^2} \sin \theta \sin \alpha + \\
& \left. \begin{aligned}
& \frac{-v^{(n)}}{r^{(n)2} + \frac{1}{r^{(n)2}} \frac{\partial^2 v^{(n)}}{\partial \alpha^2} + \frac{2}{r^{(n)2}} \frac{\partial u^{(n)}}{\partial \alpha} + \frac{1}{r^{(n)}} \frac{\partial v^{(n)}}{\partial r^{(n)}} + \frac{\partial^2 v^{(n)}}{\partial r^{(n)2}} - \frac{\frac{\partial v^{(n)}}{r^{(n)} \partial \alpha} \sin \alpha}{\delta + r^{(n)} \cos \alpha}}{2} \\
& \frac{2}{\text{Re}} \left[ \frac{u^{(n)} \sin \alpha}{(\delta + r^{(n)} \cos \alpha) r^{(n)}} + \frac{\frac{\partial v^{(n)}}{\partial r^{(n)}} \cos \alpha}{\delta + r^{(n)} \cos \alpha} - \frac{v^{(n)} \sin^2 \alpha}{(\delta + r^{(n)} \cos \alpha)^2} + \frac{\frac{\partial^2 v^{(n)}}{\partial \theta^2}}{(\delta + r^{(n)} \cos \alpha)^2} \right. \\
& \left. \frac{u^{(n)} \cos \alpha \sin \alpha}{(\delta + r^{(n)} \cos \alpha)^2} + \frac{2\sqrt{\delta} \frac{\partial w^{(n)}}{\partial \theta} \sin \alpha}{(\delta + r^{(n)} \cos \alpha)^2} \right]
\end{aligned} \right)
\end{aligned} \tag{A10}$$

The  $\theta$  direction:

$$\begin{aligned}
& \frac{\partial w^{(n)}}{\partial t^{(n)}} + \frac{v^{(n)}}{\sqrt{\delta}} \frac{\partial w^{(n)}}{r^{(n)} \partial \alpha} + \frac{u^{(n)}}{\sqrt{\delta}} \frac{\partial w^{(n)}}{\partial r^{(n)}} - \frac{w^{(n)} v^{(n)}}{\sqrt{\delta}} \frac{\sin \alpha}{\delta + r^{(n)} \cos \alpha} + \frac{u^{(n)} w^{(n)}}{\sqrt{\delta}} \frac{\cos \alpha}{\delta + r^{(n)} \cos \alpha} \\
& + \frac{w^{(n)}}{\delta + r^{(n)} \cos \alpha} \frac{\partial w^{(n)}}{\partial \theta} = -\frac{1}{\delta + r^{(n)} \cos \alpha} \frac{\partial P^{(n)}}{\partial \theta} + \frac{ag}{V^2} \cos \theta + \\
& \left. \begin{aligned}
& \frac{2}{\text{Re}} \left[ \frac{1}{r^{(n)2}} \frac{\partial^2 w^{(n)}}{\partial \alpha^2} + \frac{1}{r^{(n)}} \frac{\partial w^{(n)}}{\partial r^{(n)}} + \frac{\partial^2 w^{(n)}}{\partial r^{(n)2}} - \frac{\frac{\partial w^{(n)}}{r^{(n)} \partial \alpha} \sin \alpha}{\delta + r^{(n)} \cos \alpha} + \frac{\frac{\partial w^{(n)}}{\partial r^{(n)}} \cos \alpha}{\delta + r^{(n)} \cos \alpha} - \right. \\
& \left. \frac{2 \sin \alpha \frac{\partial v^{(n)}}{\sqrt{\delta} \partial \theta}}{(\delta + r^{(n)} \cos \alpha)^2} + \frac{2 \cos \alpha \frac{\partial u^{(n)}}{\sqrt{\delta} \partial \theta}}{(\delta + r^{(n)} \cos \alpha)^2} - \frac{w^{(n)}}{(\delta + r^{(n)} \cos \alpha)^2} + \frac{\frac{\partial^2 w^{(n)}}{\partial \theta^2}}{(\delta + r^{(n)} \cos \alpha)^2} \right]
\end{aligned} \right)
\end{aligned} \tag{A11}$$

The Reynolds number, Re, is based on the pipe diameter. There are other ways to non-dimensionalize these equations (for example Berger et al. 1983). For fully-

developed laminar flow (helical pipe, where the torsion is insignificant), it is possible to drop the unsteady term, and then multiply by  $\sqrt{\delta}$  to remove this term from the denominators of the left hand sides. This causes the viscous terms to be multiplied by  $\frac{2\sqrt{\delta}}{Re} = \frac{2}{De}$ , where  $De$  is the Dean number. This indicates that for fully-developed laminar flow, the Dean number plays the role of the Reynolds number (for example Berger et al. 1983). The non-dimensional parameter multiplying the unit gravity vector is the Richardson number  $Ri = \frac{ag}{V^2}$  which is small, so gravity could be neglected, resulting in the Reynolds number and the curvature ratio determining the velocity field.

## Appendix B: Discussion of the Particle Equation

The Lagrangian equation of motion for a spherical particle is (Maxey & Riley, 1983):

$$\begin{aligned}
 \underbrace{m_p \frac{d\vec{V}_p}{dt}}_{\text{I particle inertia}} = & \underbrace{m_f \frac{D\vec{V}}{dt}}_{\text{II force exerted on an equivalent fluid particle due to the unperturbed flow}} - \underbrace{\frac{1}{2} m_f \frac{d}{dt} \left( \vec{V}_p - \vec{V} - \frac{1}{40} d_p^2 \nabla^2 \vec{V} \right)}_{\text{III added mass term with Faxen correction}} - \underbrace{3\pi d_p \mu \left( \vec{V}_p - \vec{V} - \frac{1}{24} d_p^2 \nabla^2 \vec{V} \right)}_{\text{IV Stokes drag term with Faxen correction}} \\
 & - \underbrace{1.5 \sqrt{\pi \mu \rho} d_p^2 \int_0^t \frac{d}{d\xi} \left( \vec{V}_p - \vec{V} - \frac{1}{24} d_p^2 \nabla^2 \vec{V} \right) \frac{d\xi}{\sqrt{t-\xi}}}_{\text{V the Basset term with Faxen correction}} d\xi + \underbrace{\bar{g} (m_p - m_f)}_{\text{VI gravitational term (with buoyancy)}} + \underbrace{\bar{F}_{Saffman}}_{\text{VII Saffman Lift Force}}
 \end{aligned} \tag{B1}$$

To derive the Lagrangian equation of motion for a sphere in a fluid, Maxey and Riley (1983) split the forces into two parts: forces due to the unperturbed flow, and additional forces due to the perturbation of the velocity field by the particle. The unperturbed part can be represented approximately by terms II and VI. Term II is the force on a fluid particle occupying the same volume as the aerosol particle if the aerosol particle wasn't there. It is assumed that the sphere is small enough that the volume occupied by it can be approximated as a differential element. This term shows up in the left hand side of the Navier-Stokes equations, so it is already solved once the unperturbed velocity field is calculated. Term VI is the gravitational force on the aerosol particle (including buoyancy, which is actually a perturbed component).

The forces on the particle due to the perturbation of the flow-field by the presence of the particle are terms III, IV, V and VII. Term III is the added mass term, representing the acceleration of the perturbed component of the flow-field in response to an acceleration of the particle. Term V is the Basset history term, which represents the fact that the acceleration of the flow-field in response to the particle acceleration is not

instantaneous. The fluid right next to the particle is accelerated with the particle, but the momentum of this fluid then diffuses away to the rest of the flow-field due to viscosity. This is the same effect seen in the impulsively started plate problem (Stoke's first problem. See Kundhu and Cohen, 2002). Term IV is the Stokes drag term, representing the drag force due to the perturbed component of the flow-field for constant velocity. Term VII is the Saffman lift force, a force perpendicular to the unperturbed streamlines due to the perturbed component of the velocity field.

To estimate the additional forces due to the disturbance of the flow-field by the particle, the undisturbed flow-field is perturbed, but first the acceleration and velocity frames are made to coincide with the centre of the aerosol particle. The new velocity field is  $\vec{V}^{(0)} = \vec{V} - \vec{V}_p$ , and the fluid equations become:

$$\nabla \cdot \vec{V}^{(0)} = 0$$

$$\frac{\partial \vec{V}^{(0)}}{\partial t} + (\vec{V}^{(0)} \cdot \nabla) \vec{V}^{(0)} = -\frac{1}{\rho} \nabla P + \frac{d\vec{V}_p}{dt} + \frac{1}{\rho} \vec{g} + \frac{\mu}{\rho} \nabla^2 \vec{V}^{(0)} \quad (\text{B2})$$

The new velocity and pressure due to the perturbation are represented as:

$$\vec{V}^{(2)} = \vec{V}^{(0)} + \vec{V}^{(1)}$$

$$P^{(2)} = P^{(0)} + P^{(1)} \quad (\text{B3})$$

The perturbed components are denoted by the superscript (1). Since it is already assumed that the undisturbed flow-field satisfies the fluid equations (small perturbation), and the new flow-field must satisfy them too, the perturbed components must separately satisfy the continuity equation, and they must satisfy the following x-component equation:

$$\frac{\partial u^{(1)}}{\partial t} + u^{(0)} \frac{\partial u^{(1)}}{\partial x} + u^{(1)} \frac{\partial u^{(0)}}{\partial x} + u^{(1)} \frac{\partial u^{(1)}}{\partial x} = -\frac{1}{\rho} \frac{\partial P^{(1)}}{\partial x} + \frac{\mu}{\rho} \nabla^2 u^{(1)} \quad (\text{B4})$$

The other component directions are similar. Now, Maxey and Riley assume that the convective terms are practically zero (small particle Reynolds number), de-coupling the perturbed components from the un-perturbed ones. Their results for the forces due to the perturbation are terms III, IV and V of the particle equation. These terms have been approximated by previous investigators. Term III, the added mass term, is due to the acceleration of the flow-field around the particle as the particle accelerates (Basset, 1888). Term IV is the Stokes drag term, previously given by George Stokes (see Basset, 1888), for steady flow and small particle Reynolds number. Term V is the Basset term, given by Basset (1888). The Faxen terms account for the deviation of the unperturbed velocity field from uniform flow.

The Saffman force is missing from the Maxey Riley derivation. It was derived by Saffman (1965), and is an effect due to a non-zero particle Reynolds number, even though the derivation assumes a small Reynolds number, derived using the method of perturbations. The Maxey and Riley derivation assumes that the particle Reynolds number is negligible, so it neglects this term. The derivation assumes a constant velocity gradient perpendicular to the flow streamlines ( $\Gamma$ ). The formula is:

$$F_{Saffman} = -81.2\pi^2 \sqrt{\mu\rho} (V_p - V) d_p^2 |\Gamma|^{1/2} \text{sgn}\{\Gamma\}, \quad (\text{B5})$$

where the force is perpendicular to the streamlines. The Lagrangian equation of particle motion (B1) assumes the following:

- Negligible particle Reynolds number
- Particle small relative to spatial gradients